



**UNIVERSITY OF SOUTHERN DENMARK**

**MADS CLAUSEN INSTITUTE**

**NanoSYD**

Final Master Thesis

**NANOSTRUCTURE-INDUCED FIELD-ENHANCED NONLINEAR  
OPTICS OF PLASMONIC SUBSTRATES**

Oksana Kostiučenko

Sønderborg \* 2011

## ABSTRACT

The work is based on fabrication of plasmonic substrates and observation of second-order nonlinear optical properties in form of Second-Harmonic Generation due to local surface plasmons oscillations and therefore Local Field Enhancements of gold plasmonic substrates.

Electron Beam Lithography (EBL) is advanced high resolution lithography technique that was implemented in order to fabricate three kinds of plasmonic substrates geometries with well-defined dimensions up to 450 nm and periodicity up to 750 nm.

Femtosecond laser ablation of two different thicknesses of PMMA as a quantification method of local field enhancements was performed by means of two-photon excited second-harmonic generated signal, which is exactly  $\lambda/2$  and thus, twice frequency in comparison with incident electromagnetic excitation. Spectra Physics Tsunami a broadband pulsed laser (<100 fs of pulse duration, 80 MHz of repetition rate and max pulse energy of 8 nJ) combined with a custom build laser scanning microscope (laser spot diameter 600 nm) with centered wavelength at 790 nm was used. Due to the short pulse duration thermal effects are minimized. PMMA was used due to its transparency and low ablation threshold. Irradiation was performed at normal incidence with controlled linear polarization.

Electron Beam Evaporation technique with precise deposition thickness rate was implemented for deposition of very thin gold films of 70 and 55 nm. Spin-coating technique for EBL and laser ablation of plasmonic substrates was fulfilled varying rotation speed and therefore thickness of final film of PMMA, which was estimated then using profilometry surface probing technique. Laser threshold fluence for PMMA was theoretically estimated and plotted versus number of pulses. The number of surface investigation techniques, such as Optical Microscopy, Atomic Force Microscopy, Scanning Electron Microscopy were performed in order to get results of each fabrication step and ablation analysis. Electromagnetic radiation propagation over the one single gold nanotriangle, nanosquare and nanorectangle of 55 nm thickness on a Si-Gold substrate at 790 nm of incident light was simulated using commercial Electro Magnetic Explorer software, which was licensed to me as a trial version for one month.

## **PREFACE**

All the experiments described in thesis were held using NanoSYD cleanroom facilities and Nanooptics Laboratory equipment of Mads Clausen Institute at University of Southern Denmark during 2010/2011 years. I want to express my thankfulness to University of Southern Denmark for giving me a great possibility to be a master student of Mads Clausen Institute and advance my scientific and personal development.

For the successful preparation of a final master thesis, the support of comprehending people is necessary. Therefore, I would like to express honest gratitude for my supervisors: Professor Horst-Günter Rubahn; Professor Jakob Kjelstrup-Hansen; and Postdoc Jacek Fiutowski, for giving me important directions, helpful atmosphere, constructive comments and become an immediate party to my final project.

I would also like to express my sincere thankfulness to Postdoc Christian Maibohm and Postdoc Jacek Fiutowski for their assistance during the dangerous and safety rules attention-required femtosecond laser experiments and all the technical part, accompanied by clear explanation of physical concepts of the work.

## TABLE OF CONTENTS

ABSTRACT.....	i
PREFACE.....	ii
Aim of the work and the following objectives.....	1
1. THEORY AND LITERATURE REVIEW .....	3
1.1 Maxwell's Equations .....	3
1.2 The Plasma Sea.....	4
1.2.1 The Dielectric Function of the Free Electron Gas .....	5
1.3 Plasmonics .....	8
1.3.1 SPP, LSP and Volume Plasmon concepts.....	9
1.4 Non-Linear Optics and Second-Harmonic Generation.....	12
1.4.1 Second-Harmonic Generation.....	13
2. METHODOLOGY AND FABRICATION PART.....	15
2.1 Electron Beam Evaporation.....	15
2.2 Spin-Coating technique .....	17
2.3 Electron Beam Lithography.....	19
2.4 Lift-Off .....	22
2.5 Profilometry.....	23
2.6 Atomic Force Microscopy .....	24
2.7 LSM and SHG Measurements .....	25
2.8 Laser ablation of PMMA .....	27
3. EXPERIMENTAL RESULTS.....	32
3.1 Fabrication steps .....	32
3.2 Optical Microscopy results .....	35
3.3 Scanning Electron Microscopy images of fabricated plasmonic substrates.....	37

3.4 Atomic Force Microscopy results of fabricated plasmonic substrates .....	42
3.5 Ellipsometry data of fabricated plasmonic substrates .....	46
3.6 Second-Harmonic spectra and imaging of plasmonic substrates .....	49
3.7 Scanning Electron Microscopy images of ablated substrates.....	51
3.8 Software-based Near-Field Intensities simulation of plasmonic substrates .....	61
4. DISCUSSIONS AND FUTURE PLANS .....	66
CONCLUSIONS.....	67
REFERENCES .....	68
Appendix 1.....	72
Appendix 2.....	74
Appendix 3.....	74
Appendix 4.....	75
Appendix 5.....	77
Appendix 6 .....	78

## **Aim of this work**

Using Electron Beam Lithography to form gold plasmonic substrates with three different geometries at nanoscale and investigate nonlinear optical properties of them demonstrating electromagnetic field enhancements mapping by femtosecond laser pulse ablation of polymethyl methacrylate covered on top.

Therefore, **the following objectives** are:

- Fabrication of 450 x 450 nm triangles with periodicity of 750 x 750 nm, 450 x 900 nm rectangles with periodicity of 750 x 1030 nm and 450 x 450 nm squares with periodicity of 750 x 750 nm by high resolution EBL technique. Scanning Electron Microscopy, Atomic Force Microscopy based dimensions measurements and surface topography evaluation of fabricated substrates;
- Femtosecond laser pulse ablation of PMMA covered on top of fabricated nanostructures;
- Two photon based Laser Scanning Microscopy nonlinear optical properties evaluation of fabricated gold plasmonic substrates.

Work performed and tasks accomplished:

1. Electron Beam Evaporation of thin 70 and 55 nm gold films;
2. PMMA spin-coating, varying rotation speeds and therefore thicknesses of covered films. Thickness measurements of coated thin film, implementing surface probing Profilometry technique;
3. Electron Beam Lithography high resolution mask for nano-triangles, nano-rectangles and nano-squares fabrication;
4. Lift-off technique fulfilling in order to dispose secondary fabrication parts and achieve precise nanostructured geometries;
5. Scanning Electron Microscopy final geometries evaluation of fabricated plasmonic substrates;
6. Laser Scanning Microscopy based second-harmonic spectra measurement of plasmonic substrates, illuminated by 790 nm centred Gaussian shape femtosecond pulsed laser beam;

7. Field Enhancements of gold plasmonic substrates mapping by femtosecond laser ablation of PMMA covered on top;
8. Ellipsometry based reflection spectra measurements of gold plasmonic substrate;
9. EM Explorer-solved Near-Field Intensities of fabricated each single nano-triangle, nano-rectangle and nano-square geometry.

## 1. THEORY AND LITERATURE REVIEW

This chapter represents the main theoretical aspects related to plasmonic phenomena interpretation. The “Plasmonics: Fundamentals and Applications” book written by Steffan A. Maier, University of Bath [1], and theory from the lectures help to imagine and understand the principles of how metals behave during irradiation of them by electromagnetic waves.

### 1.1 Maxwell's Equations

Electromagnetic wave theory starts from the works of the famous scientists James Clerk Maxwell and his set of partial differential ‘microscopic’ and ‘macroscopic’ equations with support of Gauss’s law (equation 1.1) for magnetism (equation 1.2), Faraday’s law of induction (equation 1.3), Amperes circuital law (equation 1.4), describe mathematically the variation of electromagnetic wave in time and in the media. These formulas are the basis for classical electrodynamics, optics and electric circuit sciences and ingeniously underlie the electrical and communication technology.

The ‘macroscopic’ Maxwell’s equations are the basic equations, determining the electromagnetic response of metals, enabling not to be detailed into the fundamental interactions between charged particles inside media and electromagnetic fields, since the rapidly varying microscopic fields are averaged over distances much larger than the underlying structure [1].

Maxwell’s equations of macroscopic electromagnetism in the following form are represented below [1]:

$$\nabla \cdot D = \rho_{ext}; \quad (1.1)$$

$$\nabla \cdot B = 0; \quad (1.2)$$

$$\nabla \times E = -\frac{\partial B}{\partial t}; \quad (1.3)$$

$$\nabla \times H = J_{ext} + \frac{\partial D}{\partial t}; \quad (1.4)$$

where, D – the dielectric displacement field;

E – the electric field;

H – the magnetic field;

B – the magnetic induction or magnetic flux density field;

$\rho_{\text{ext}}$  – external charge density;

$J_{\text{ext}}$  – external current density;

The total charge and current are described as follows (equations 1.5 and 1.6) [1]:

$$J_{\text{total}} = J_{\text{ext}} + J; \quad (1.5)$$

$$\rho_{\text{total}} = \rho_{\text{ext}} + \rho; \quad (1.6)$$

where,  $J_{\text{ext}}$  and  $\rho_{\text{ext}}$  – are external current and charge driving the system, while

$J$  and  $\rho$  – are internal current and charge responding to the external stimuli [1].

These four macroscopic fields of dielectric displacement (equation 1.1), the magnetic induction or magnetic flux density (equation 1.2), electric field (equation 1.3) and magnetic field (equation 1.4) can be linked by the polarization  $P$  and magnetization  $M$  (equations 1.7 and 1.8) [1]:

$$D = \varepsilon_0 E + P; \quad (1.7)$$

$$H = \frac{1}{\mu_0} B - M; \quad (1.8)$$

where,  $\varepsilon_0$  - the electric permittivity and

$\mu_0$  – magnetic permeability of vacuum.

## 1.2 The Plasma Sea

The transport properties of electrons in materials, especially metals have been explained by Paul Drude in 1900. Drude model suppose that behavior of electrons in a solid looks like a sea of constantly moving electrons, which collide between themselves and furthermore are always shaking into and out of a heavy positively charged ions. With each collision electrons loss certain part of their kinetic energy, and damping of electric field occurs.

Conduction electrons of the metal due to their chaotic thermal motion could even jump out from the metal body. Therefore, there is an electron cloud existing near metal surface, which is constantly giving the electrons back to the metal body, thus enabling the dynamic equilibrium between the metal body electrons and electrons of the cloud near the surface. An evident

concentration of electrons in the electron cloud is observing over a distance of about several interatomic levels. There is an excess of positively charged ions on the metal surface. These charges and an electron cloud form a thin double electrical layer with an electrical field, which prevents the electrons from flying far away from the metal surface.

Over a wide frequency range, the optical properties of metals can be explained by a *plasma model*, where a gas of free electrons of number density  $n$  moves against a fixed background of positive ion cores [1]. For instance, for the frequencies of Microwaves or Far Infrared (FIR) part of the electromagnetic spectrum, metals are highly reflective, therefore do not allow the electromagnetic waves to propagate through them and only a negligible fraction of the electromagnetic waves penetrates into the metal. Metals are perfect or good conductors at this low-frequency regime. At higher frequencies of Near Infrared (NIR) and Visible (VIS) parts of the electromagnetic spectrum, metals become less resistant to electromagnetic wave penetration. Thus, the penetration increases significantly, increasing dissipation, and prohibiting a simple size scaling of photonic devices that work well at low frequencies at this regime [1]. For Ultraviolet (UV) frequencies, metals acquire a lot of dielectric behavior, enabling the penetration and propagation of electromagnetic waves with varying degrees of attenuation, depending on the details of the electronic band structure. Noble metals, for example gold, exhibit strong absorption in the UV frequency regime due to transitions between electronic bands.

### 1.2.1 The Dielectric Function of the Free Electron Gas

If we do not forecast electron-electron interactions and the details of lattice potentials, the optical properties of metals can be explained by a plasma model (electrons + positive ions), where the band structure is assumed like the effective optical mass  $m$  of each electron. The electrons oscillate (Fig. 1.1) in response to the applied electromagnetic field, and their motion is damped via collisions occurring with a characteristic collision frequency (equation 1.9) [1].

$$\gamma = 1/\tau; \tag{1.9}$$

where,  $\tau$  is the relaxation time of the free electron gas. At room temperature it is on the order of  $10^{-14}$ , corresponding to  $\gamma = 100$  THz [1].

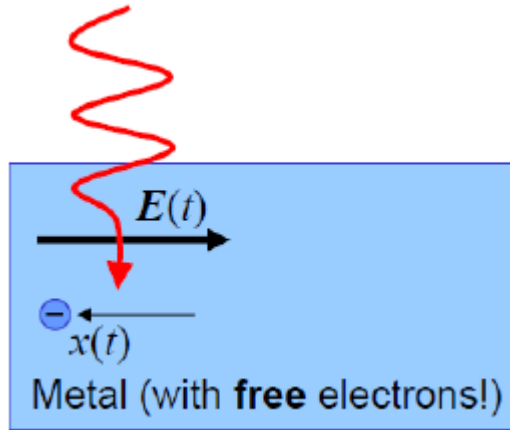


Figure 1.1 Schematic drawing of the concept of the harmonic time dependence  $E(t)$  and the oscillation of the electron  $x(t)$  inside metal body irradiated by electromagnetic wave [lection material of plasmonics part1]

Motion of the electron in the plasma sea, forced by an external electric field  $E$  is represented in equation 1.10 [1]:

$$m\ddot{x} + m\gamma\dot{x} = -eE; \quad (1.10)$$

If harmonic time dependence of the driving field (equation 1.11) [1]:

$$E(t) = E_0 e^{-i\omega t}; \quad (1.11)$$

A particular solution of this equation describing the oscillation of the electron is (equation 1.12) [1]:

$$x(t) = x_0 e^{-i\omega t}; \quad (1.12)$$

The complex amplitude  $x_0$  incorporates any phase shifts between driving field and response via equation 1.13 [1]:

$$x(t) = \frac{e}{m(\omega^2 + i\gamma\omega)} E(t); \quad (1.13)$$

The displaced electrons assist in the macroscopic polarization (dipole moment/volume) (1.14). Equation 1.15 represents polarization equation in detail [1]:

$$P = -nex; \quad (1.14)$$

$$P = -\frac{ne^2}{m(\omega^2+i\gamma\omega)}E \quad (1.15)$$

Inserting equation 1.15 into 1.7 the relation to dielectric displacement (response) is given by equation 1.16 [1]:

$$D = \varepsilon_0 E + P; \quad D = \varepsilon_0 \left(1 - \frac{\omega_p^2}{\omega^2+i\gamma\omega}\right) E; \quad (1.16)$$

where,  $\omega_p^2 = \frac{ne^2}{\varepsilon_0 m}$  is the plasma frequency of the free electron gas.

Thus, the dielectric function of the free electron gas can be described by the equation 1.17 [1]:

$$D = \varepsilon_0 \varepsilon E; \quad \varepsilon(\omega) = 1 - \frac{\omega_p^2}{\omega^2+i\gamma\omega}; \quad (1.17)$$

Here, the real and imaginary components of this complex dielectric function (figure 1.2) (equation 1.18) [1].

$$\varepsilon(\omega) = \varepsilon_1(\omega) + i\varepsilon_2(\omega); \quad (1.18)$$

are:

$$\varepsilon_1(\omega) = 1 - \frac{\omega_p^2 \tau^2}{1+\omega^2 \tau^2}; \quad (1.19)$$

$$\varepsilon_2(\omega) = \frac{\omega_p^2 \tau}{\omega(1+\omega^2 \tau^2)}; \quad (1.20)$$

We have used  $\gamma = 1/\tau$ . It is insightful to study (1.17) for a variety of different frequency regimes with respect to the collision frequency  $\gamma$  [1]. We will limit ourselves here to frequencies  $\omega < \omega_p$ , where metals retain their metallic character. For large frequencies close to  $\omega_p$ , the product  $\omega\tau \gg 1$ , leading to negligible damping [1]. Here,  $\varepsilon(\omega)$  is predominantly real, and

$$\varepsilon(\omega) = 1 - \frac{\omega_p^2}{\omega^2}, \quad (1.21)$$

can be taken as the dielectric function of the undamped free electron plasma [1].

As examples, figure 1.2 shows the real and the imaginary parts  $\varepsilon_1(\omega)$  and  $\varepsilon_2(\omega)$  of the dielectric function for gold [Johnson and Christy, 1972] [1].

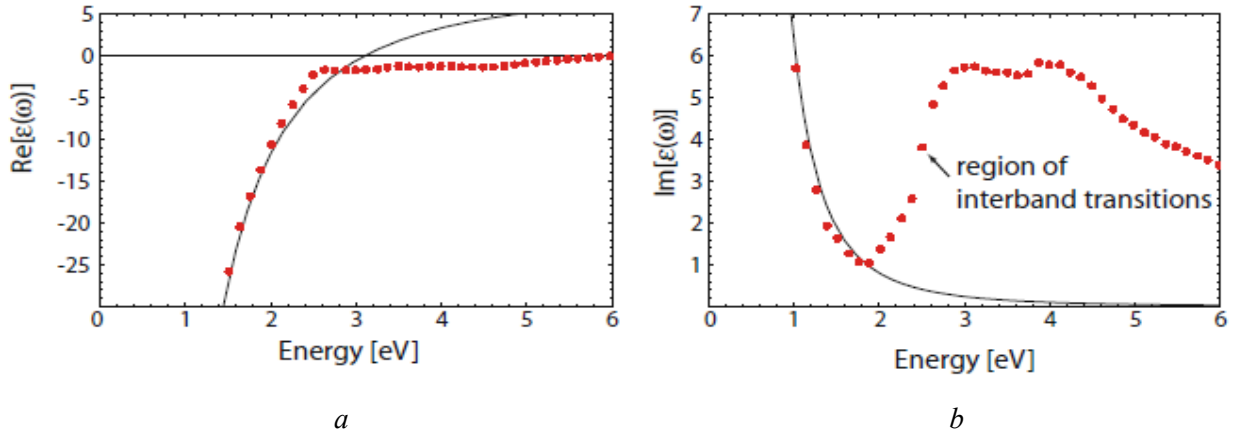


Figure 1.2 Dielectric function  $\varepsilon(\omega)$  of the free electron gas (solid line) fitted to the literature values of the dielectric data for gold [Johnson and Christy, 1972] (dots). Interband transitions limit the validity of this model and higher frequencies [1]: a) real and b) imaginary parts of the complex dielectric function for gold.

### 1.3 Plasmonics

Plasmonics is a new rapidly developing challenging branch of the attractive field of photonics (nanooptics), makes it possible to manipulate light beyond a diffraction limit and enhance or localize electromagnetic fields at extremely small structures on the order of several hundreds of nm and even investigate the unique optical properties of these structures and materials. In the other words, plasmonics is the study of light-matter interaction, which finds implementation in different fields of science, such as: biological and chemical sensing, surface plasmon microscopy, lithographic fabrication, optical sensors, waveguides, plasmon couplers (converting photons to plasmons) and many others. As the fact, integration circuits based on fundamentals of plasmonics work much faster, have significantly greater information capacity with by far smaller dimensions, than traditional integration circuits.

Consequently, plasmonics is based on investigation, excitation and evaluation of localized surface plasmons, surface plasmons polariton and volume plasmons phenomenon.

First of all, for better imagination of plasmon occurrence, it can be divided into two parts:

- Surface plasmons (surface plasmon polaritons, localized surface plasmons) and

- Volume plasmons;

### 1.3.1 SPP, LSP and Volume Plasmon concepts

Plasmons are quasiparticles appearing in a solid body due to vibrations of conduction electrons relatively positively charged framework of ions (section 1.2). If a material (gold) is distinguished by its negative real or small positive imaginary dielectric constant it contributes in surface plasmon resonance appearance. Vibrations of electrons are excited either by electromagnetic irradiation (photons) or electrons (by firing electrons into the bulk of a metal). Electron-photon coupled hybridized coherent oscillations are called surface plasmon polaritons. Due to propagation across the metal-dielectric (metal-air) interface these oscillations loss energy because of either absorption in the metal or radiation into free-space. In the case of surface plasmon polaritons (SPP), plasmons propagate in the x- and y- directions along the metal-dielectric interface, for distances in the order of tens to hundreds of microns, and decay evanescently in z-direction with  $1/e$  decay lengths on the order of 200 nm [2].

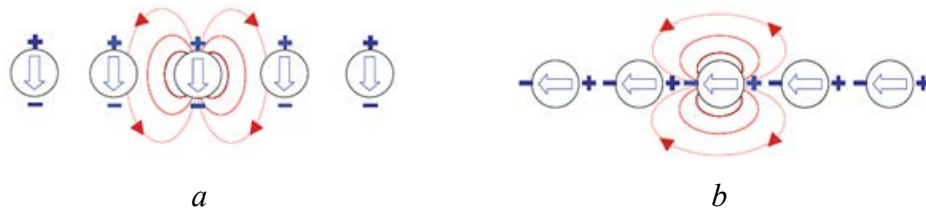


Figure 1.3 Schematics of near-field charges coupling between metallic nanoparticles for the two-different polarizations [1]: a) s-polarized light; b) p-polarized light.

It has been mentioned at the beginning of section 1.3.1 that surface plasmons are quasiparticles or surface electromagnetic waves held in the metal-dielectric boundary; it appears because of scattering of light across the certain structurized surface. Thereby, in the issue of plasmon migrations extremely intensive localized maximum on the tops or sharp edges (Tables 3.5 and 3.7) of the structures can be observed. Consequently, it becomes possible to concentrate energy in nanometer scale, even spectral characteristics will be predefined by geometry (Appendix 1). Localized surface plasmons (LSP or LSP Resonance) (Fig. 1.3) exists when light interacts with particles much smaller than the incident wavelength.

This leads to plasmon oscillate locally around the nanoparticle with a frequency known as the LSPR (Fig. 1.4 b) [2]. If dimensions of nanoparticle is much smaller than the wavelength of

illuminating light ( $a/\lambda < 0.1$ ), it results the case of static electric field around the nanoparticle (LSPR) (Fig. 1.4 b). Equation 1.22 express solution of EM field propagation for this case [2]:

$$E_{out}(x, y, z) = E_0 \hat{z} - \left[ \frac{\varepsilon_{in} - \varepsilon_{out}}{(\varepsilon_{in} + 2\varepsilon_{out})} \right] a^3 E_0 \left[ \frac{\hat{z}}{r^3} - \frac{3z}{r^5} (x\hat{x} + y\hat{y} + z\hat{z}) \right]; \quad (1.22)$$

where,  $\varepsilon_{in}$  is the dielectric constant of the metal nanoparticle,

$\varepsilon_{out}$  is the dielectric constant of the external environment.

The first term in square brackets determines the dielectric resonance condition for the particle, since the dielectric constant of the metal nanoparticle is strongly dependent on wavelength.

When the dielectric constant of the metal nanoparticle is approximately on the order of  $-2\varepsilon_{out}$ , the EM field is enhanced relative to the incident field. In the case of noble metals, such as silver or gold this condition could be observed at the visible part of the EM spectrum.

Equation 1.23 represents the extinction spectrum of the metal nanoparticle, or rather the influence of  $\varepsilon_{out}$  and size  $a$  on the EM field propagation outside the nanoparticle [2]:

$$E(\lambda) = \frac{24\pi^2 N a^3 \varepsilon_{out}^{3/2}}{\lambda \ln(10)} \left[ \frac{\varepsilon_i(\lambda)}{(\varepsilon_r(\lambda) + \chi \varepsilon_{out})^2 + \varepsilon_i(\lambda)^2} \right]; \quad (1.23)$$

where,  $\varepsilon_r$  is the real part of the metal complex dielectric function,

$\varepsilon_i$  is the imaginary part of the metal complex dielectric function.

$\chi$  is the factor, which for instance, in the case of spherical nanoparticle is equal 2, but could be even on the order of 20, depending on particle geometry. It could be either analytical evaluation of this factor, finite-difference time-domain or discrete dipole approximation.

In addition, equation 1.24 represents shifting of the wavelength of extinction spectra in the case, when additional adsorbed layer (molecules or nanoparticles) exist on the plasmonic surface being evaluated spectroscopically [2]:

$$\Delta\lambda_{max} = m\Delta n \left[ 1 - \exp\left(-2d/l_d\right) \right]; \quad (1.24)$$

where,  $m$  is response of the bulk refractive index of the nanoparticles and

$n$  is change response of the bulk refractive index affected by an adsorbate layer with

$d$  – thickness of an adsorbate layer.

Like electrons oscillations of the surface plasmons (SPs), volume plasmons occur in the volume of a metal due to collective excitations of the dense electron gas (valence electrons of a metal  $n_0 \sim 10^{22} \text{ cm}^{-3}$  or in semiconductor  $n_0 \sim 10^{19} \text{ cm}^{-3}$  [3]. The energy quanta of these volume plasma oscillations are called volume plasmons. The positive ions neutralise the mean negative charge (electrons). The density oscillations  $\Delta n$  of  $n$  can be expressed by plane longitudinal waves with the amplitude  $\Delta n_{max}$  in 1.25 equation [3]:

$$\Delta n(x, t) = n(x, t) - n = \Delta n_{max} \exp i (\omega t - qx); \quad (1.25)$$

where,  $\omega$  is the frequency and

$$q = 2\pi/\lambda \text{ is the wave vector.}$$

Volume plasmons could be also defined as collective mode oscillations, due to a high number of electrons participates at such a kind of oscillations. Here electrons of the plasma are treated as free-electrons, neglecting the periodicity of the potential of ion lattice. However, band structure cannot be neglected, since it determines the lifetime of volume plasmons. Therefore, if ones need to obtain more precise calculations, different approximations taking into account band structure and considering electron-electron correlations (Coulomb interaction and spin exchange) must be performed.

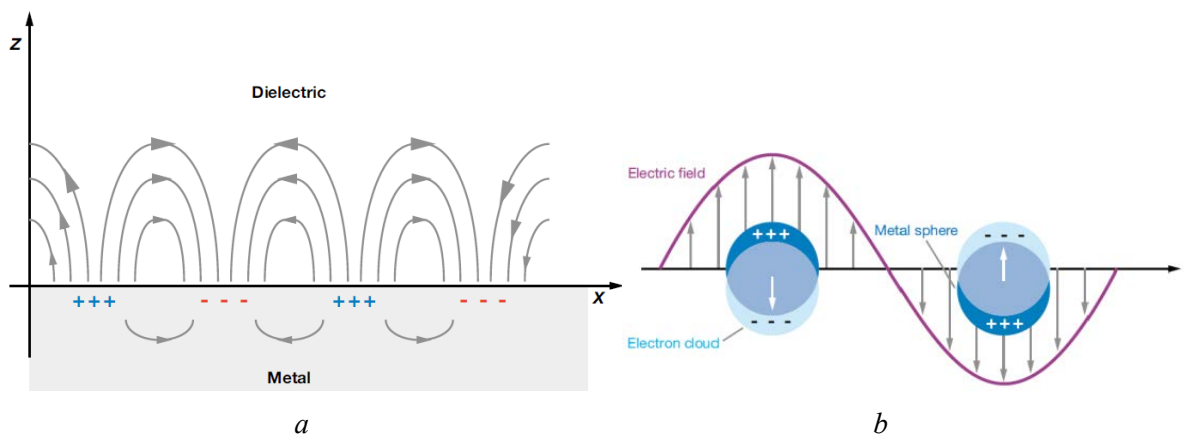


Figure 1.4 Schematic diagrams illustrating a) surface plasmon polariton (or propagating plasmon) and b) localized surface plasmons [2].

Nanoparticles of noble metals are widely used in science regarding to plasmon resonances, which are utterly sensitive to diameter of the nanoparticle.

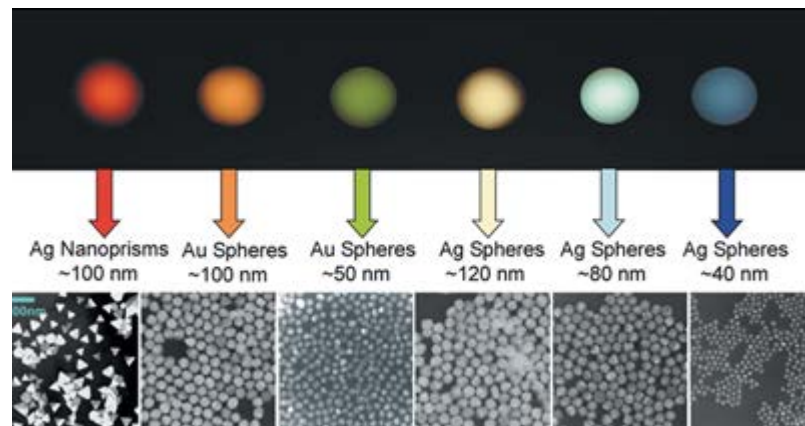


Figure 1.5 Example of Gold and Silver nanoparticles with different form and size [4].

Nano-sized metals (Fig. 1.5) have different properties from bulk metals. In this way, nanomaterials show unique properties (electronic, magnetic, structural) depending on nano-size structure.

Metal nanostructure optical properties depend on:

- 1) nature of nanostructured material (Ag, Au, Cu),
- 2) size of nanostructures (10, 100 nm,...)
- 3) shape of nanostructures (sphere, cube, triangle, rectangle, square....)
- 4) surrounding medium (refractive index) – type of the polymer and nanostructures arrangement in polymer matrix.

The specific-size dependence of these properties becomes evident when they:

- no longer follow classical physical laws but rather are described by quantum mechanical theory;
- are dominated by particular interface effects;
- refer to an almost infinite number of constituents (e.g. atoms, molecules) displaying an averaged statistical behaviour.

#### 1.4 Non-Linear Optics and Second-Harmonic Generation

Femtosecond pulsed laser appearance has significantly enlarged abilities of nonlinear optics and surface spectroscopy. Owing to high peak and small average intensity of pulsing emission it is possible to reliably measure weak nonlinear response of metallic nanostructures of different shapes.

### 1.4.1 Second-Harmonic Generation

Most common optical method of obtaining information of the surface of metallic nanostructure located between the separation of two mediums (metal-dielectric) or inside a thin film of polymer (PMMA) is Second-Harmonic Generation (SHG). Analysis of surface SHG signal dependence on incident irradiation allows gain individual information of metall nanostructures under consideration (example: phase shift of fundamental oscillation harmonics relative to the excitation signal).

Second-harmonic generation (SHG) is a specific method of imaging structures on a metal (gold) surface using a femtosecond pulsed near-infrared (NIR) laser beam. It is reliably if two photons of incident light simultaneously interact with the sample, generating a scattering photon of exactly twice the energy and therefore half the wavelength [5]. This process occurs if only a sufficient photon flux delivers at the focal plane, where condition of peculiar optical sectioning is held and provides information of 3D (three-dimensional) metal [5]. Conditions which must be kept for delivering the sufficient photon flux are both the focal plane of ablation and use of a short-pulse duration (sub 100 femtosecond) laser system which is able to produce the intense photon density at the focal plane for imaging [5].

Second-harmonic imaging is coherent, meaning that the signal propagates in a fixed direction and is sensitive to excitation light polarization relative to the sample [5].

SHG at a metal nanostructure tip results from a combination of field enhancement due to an electrostatic 'lightning rod' effect (light localization at the edges and tips of metal nanostructures), induced by the tip sharpness, and the excitation of localized surface plasmon resonances. If the polarization of an incident light is parallel to the metal nanostructure, the electric field of the incident light interacts with the free electrons in a metal, leading to charge accumulation at metal nanostructure surface, especially tips, because of localization of charge density and electric field [6].

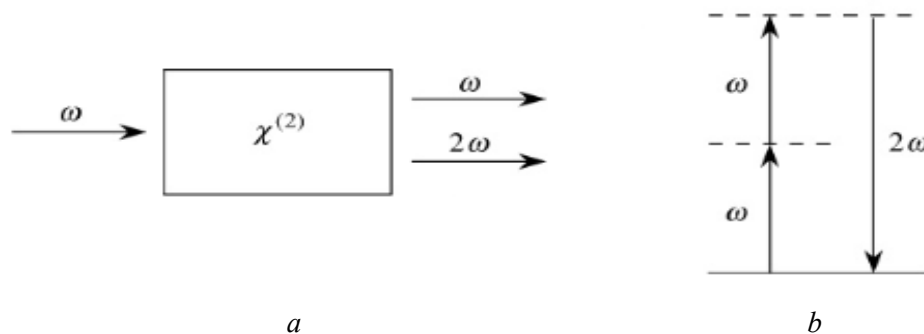


Figure 1.6 a) Geometry of SHG; b) Energy-level diagram describing SHG [7].

Second-Harmonic Generation (Fig. 1.6) is a “nonlinear” optical phenomena due to such an optical changes in the metal nanostructure depend quadratically on the strength of the incident optical field: the intensity of the light resulting from second-harmonic generation scales with the square of the applied laser light [7].

The polarization  $P(t)$ , the dipole moment per volume, of a system depends on the strength  $\hat{E}(t)$  of the optical field. In conventional optics, this relationship is linear (equation 1.26) [7]:

$$P(t) = \varepsilon_0 \chi^{(1)} \hat{E}(t); \quad (1.26)$$

where,  $\varepsilon_0$  is the permittivity of free space;

$\chi^{(1)}$  is the constant called the linear susceptibility.

However, in nonlinear optics, the generalization of this equation attains, in which the polarization goes with the power series of the field strength (equation 1.27) [7]:

$$\begin{aligned} P(t) &= \varepsilon_0 [\chi^{(1)} E(t) + \chi^{(2)} E^2(t) + \dots + \chi^{(n)} E^n(t)], \\ P(t) &= P^{(1)}(t) + P^{(2)}(t) + \dots + P^{(n)}(t); \end{aligned} \quad (1.27)$$

where,  $\chi^{(n)}$  is the n-th order nonlinear optical susceptibility;

$P^{(n)}(t)$  is the n-th order polarization.

Electric field strength of a laser is given by equation 1.28 [7]:

$$\hat{E}(t) = E e^{-i\omega t} + \text{complex conjugates}; \quad (1.28)$$

impinges on a system with a nonzero second-order susceptibility  $\chi^{(2)}$ , the polarization created is (equation 1.29) [7]:

$$P^{(2)}(t) = 2\varepsilon_0 \chi^{(2)} E E^* + (\varepsilon_0 \chi^{(2)} E^2 e^{-2i\omega t} + \text{complex conjugates}); \quad (1.29)$$

We see that the second-order polarization consists of a contribution at zero frequency (the first term) and a contribution at frequency  $2\omega$  (the second term) [7].

## 2. METHODOLOGY AND FABRICATION PART

Metal nanostructures excite a high interest owing to different possibilities of applications in plasmonics. Besides, the most suitable method of fabrication and control of 3D architecture should be held for revealing and achieving the best possible optical properties of it.

This chapter describes all chosen appropriate methods and techniques for plasmon substrates fabrication. Design and fabrication methodology of nanoarrays of specified size, shape and spacing are represented.

### 2.1 Electron Beam Evaporation

From theory, thin films are thin layers of material scaling from nanometers to several micrometers in thickness. Thin films are mostly used in electronic semiconductor devices, optical coatings, ceramic thin films of high hardness, thin films against corrosion, oxidation and wear.

Therefore, there are many different types of thin film layer deposition used today:

1. Chemical processes: Electrodeposition; Langmuir-Blodgett films; CVD (chemical vapor deposition), such as: atmospheric pressure CVD, low pressure CVD; plasma enhanced CVD and other;
2. Or Physical processes: Molecular Beam Epitaxy; Sputtering; Pulsed laser deposition; Cathodic arc deposition; Electrohydrodynamics; PVD (physical vapor deposition), such as: thermal evaporation (**electron beam evaporation**);

PVD concept is chosen and Electron Beam thermal Evaporation type of thin film deposition is performed.



*Figure 2.1 Polytechnik Cryofox Explorer 600 e equipment at NanoSYD used for E-Beam Evaporation of titanium and gold [8].*

The Cryofox Explorer 600 (Fig. 2.1) was used for metal deposition. It applies electron beam evaporation to get uniform layer of desired metal material onto a wafer.

Process (start substrate: silicon):

- Deposition of 2/70 nm titanium/gold
- E-beam lithography to define the six nanoparticle arrays
- Deposition of 2/55 nm titanium/gold and lift-off

Physical concept of the process:

The filament is heated until it emits electrons of high kinetic energy. Electrons leave the gun (an electron source) and form the electron beam which is focused and bent by a magnet (permanent magnets or electromagnets), which shapes and directs the path of the electrons onto the surface of evaporant (Ti, Au) by means of electric and magnetic fields (Fig. 2.2. a). Magnets are necessary, because the electrons are emitted in a random manner [9] and must all be directed to very small area of the target, where the evaporation occurs. Thus, the kinetic energy of electrons motion is transformed to thermal energy by the impact of a vast amount of electrons with the target material, causing it to evaporate (vaporization of Ti, Au) . The vapor then condenses on the substrate surface forming thin film (condensation of Ti and Au vapor). This is done in a high-vacuum environment ( $10^{-5}$  Torr or less), so that the vaporized atoms or molecules will be transported to the substrate with minimal collision interference from other gas atoms or molecules.

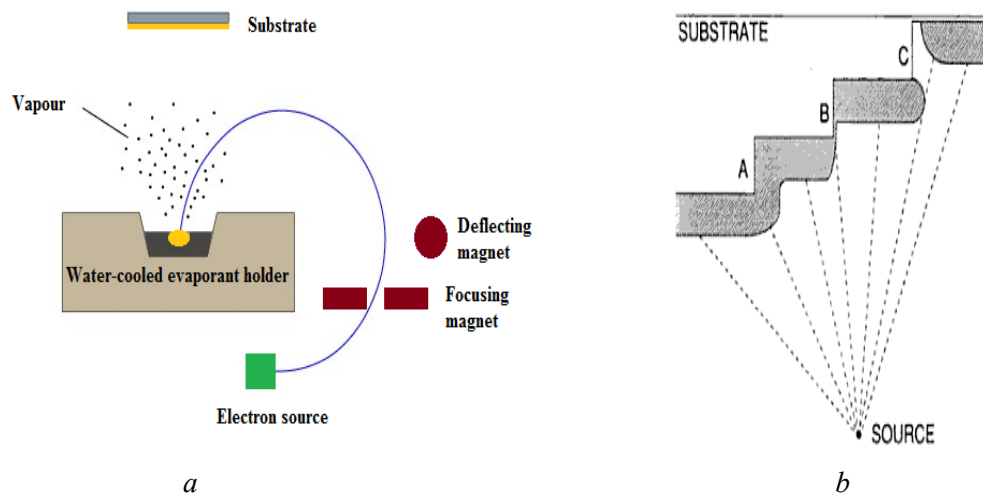


Figure 2.2 a) schematic representation of E-Beam Evaporation process of Thin Film deposition; b) schematic illustration of film coverage of stepped substrate: (A) uniform coverage; (B) poor sidewall coverage; (C) lack of coverage – discontinuous film [10].

The energy level achieved in this manner is quite high – often more than several million Watts per square inch. Compare this to the heat given off by a 100 Watt light bulb and you can

begin to appreciate the magnitude of heat generated. Due to the intensity of the heat generated by the electron beam, the evaporant holder must be water cooled to prevent it from melting. The power supply for this operation is a high voltage DC power supply, typically 10 to 30 kiloVolts, with a wattage ranging from 10 to 30 kiloWatts [9]. Multi-layer coatings can be deposited in one duty cycle. Some problems with nonuniform coverage might occur if stepped substrate is used (Fig. 2.2 b)

## 2.2 Spin-Coating technique

Spin-coating (Fig. 2.3) is a procedure to apply an uniform and homogeneous layers on a flat substrates to produce thin films. Spin-coating is widely used in microfabrication to create thin films even below to 10 nm, or as a step of the Lift-off process to produce an uniform layer of photoresist for further lithography procedure.

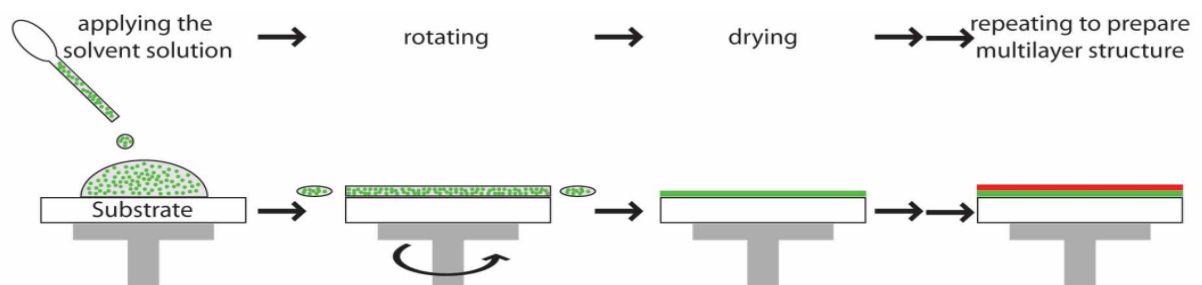


Figure 2.3 Schematic representation of spin-coating technique [11]

Physical concept of the process:

An excess amount of solution is placed on the substrate, which is then rotated at high speed in order to spread the fluid by centrifugal force. The film thickness can be adjusted by different factors, for instance the rotation speed, acceleration, the rotation time, and the concentration of used solution.

Final film thickness will depend on the nature of solution (viscosity, drying rate, percent solids, surface tension, etc.) and the parameters chosen for the spin process (Fig. 2.4). For example, if evaporation of solution is too fast, the flow of the solution will be slower, due to the higher viscosity of it. Concentration of used solution also strongly influences on the final thickness of thin film. As more concentrated the applied solution is as more thicker the final film becomes.

A typical spin-coating process consists of a:

- dispense step (static or dynamic), when solution is deposited on a substrate surface. Static dispense is performed simply placing a certain amount of solution in the centre of the

substrate, whereas dynamic dispense is placing an amount of solution while the substrate is turning at a low speed;

- a high speed spin step, when the solution is thinning by centrifugal force during rotation;
- drying step, when excess of solution is eliminated from the resulting film.

One of the most important factors in spin-coating is repeatability. Subtle variations in the parameters that define the spin process can result in drastic variations in the coated thin film. On the whole, higher rotational speeds and longer spin times create thinner films [12].

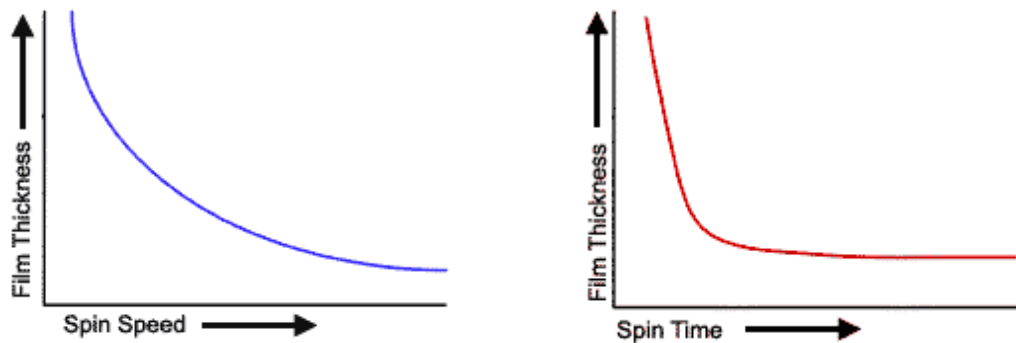


Figure 2.4 Spin-coating process trend charts representing general trends for the various process parameters: film thickness dependence on spin speed and spin time [12]

The disadvantage of this method is that it is limited by solution and that no lateral resolution is possible [11]. In addition, process parameters vary greatly for different solution materials and substrates, so, there are no fixed rules for spin-coat processing, only general guidelines. Figure 2.5 represents several specific spin-coating process problems of thin films production.

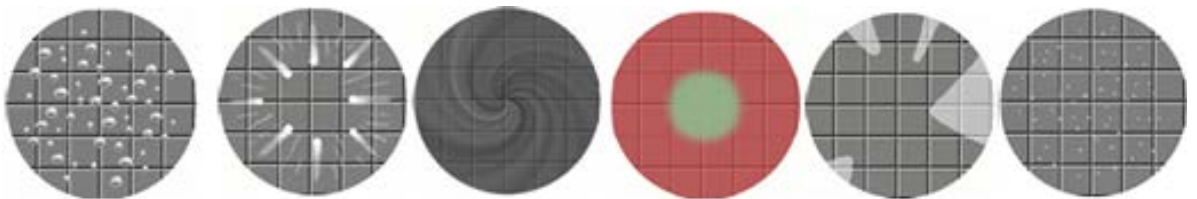


Figure 2.5 Specific spin-coating process problems of the final thin film: air bubbles; comets, streaks or flares; swirl pattern; center circle; uncoated areas; pinholes; [12]

For this experiment the spin-coater RRT Lanz EBS 11 of NanoSyd cleanroom is used (Fig. 2.6 b).

During thin film deposition step certain parameters were specified and used for successful and qualitative thin film deposition for a) PMMA thin film layer for EBL and b) PMMA thin film layer for ablation:

a) Dispense of 950 PMMA A4 is applied:

1 step) 5 s at 1000 rpm, ramping 1500 rpm/s and acceleration of 50 000 rpm/s<sup>2</sup> –uniform and smooth covering of the surface;

2 step) 45 s at 7000 rpm, ramping – 10000 rpm/s and acceleration of 50000 rpm/s<sup>2</sup> – covering of desirable thickness of thin film;

3 step) 90 s of prebaking at 200°C – from liquid to solid (hardening of spinned on thin film);

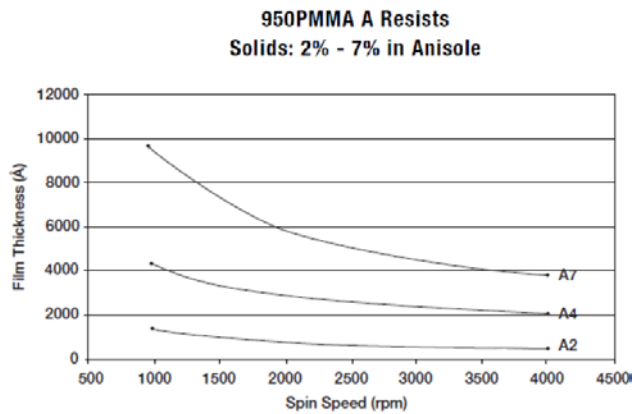
b) Dispense of 950 PMMA A4 and A2 is applied:

1 step) 5 s at 1000 rpm, ramping – 1500 rpm/s and acceleration of 50000 rpm/s<sup>2</sup> –uniform and smooth covering of the surface;

2 step) 45 s at 7000 rpm (for A4 950 PMMA) or 3000 rpm (for A2 950 PMMA), ramping – 10000 rpm/s and acceleration of 50000 rpm/s<sup>2</sup> – covering of desirable thickness of thin film;

3 step) 90 s of prebaking at 200°C – from liquid to solid (hardening of spinned on thin film);

Different rpms on accordance to desirable thickness of covered thin PMMA film have been determined using theoretical approach (Fig. 2.6 a) and analytical using Dektak 150 profilometer for thickness measurements of spinned on thin films:



a



b

Figure 2.6 a) Film thickness versus applied spin speed [39]; b) Spin-coater RRT Lanz EBS 11 of NanoSyd cleanroom [Micro- and Nanofabrication 2course slides: Lecture 1: Introduction to micro and nanosystems and lecture 6 EBL]

## 2.3 Electron Beam Lithography

Electron Beam Lithography (EBL) is a high resolution lithography technique, where a focused beam of electrons with diameter about about 0.4 nm to 5 nm [13] and energy ranging from

1 kV to 30 kV [14] typically used to form the patterns of desired design while direct scanning over a surface of photoresist. Therefore, EBL does not need masks unlike optical lithography and offers higher optical resolution, than optical lithography. However, EBL is a 'serial' production method of patterns in comparison with optical lithography, due to slow process of electron beam scanning.

The resolution of optical lithography is limited by diffraction, but this is not a problem for electron lithography. Electron beams have produced features as small as 10 nm [14]. The reason for this is the short wavelengths (0.2-0.5 angstroms) [13] exhibited by the electrons in the energy range that they are being used by EBL systems. While the EBL is used to avoid the reflection and diffraction problems existing in optical lithography, it however has a drawback relating to electron scattering in the resist, which results to degraded resolution and proximity effects of patterning.

Scattering appears when electrons strike the matter (resist, substrate) and penetrating inside it transferring energy due to collisions with the atoms of the matter. Therefore, forward or backward scattering events take place. Forward inelastic scattering under small angles is mostly appears, than backward large angles scattering. So, during the forward scattering the secondary electrons with a few eV of kinetic energy are generated, while backward scattering results in scattering of mostly primary electrons with a high kinetic energy. It „widens“ diameter of the electron beam when it penetrates the resist, therefore giving the extra energy doses for exposed resist if electrons is backscattered from the substrate.

Regardless of the beam energy, scattering occurs at an obvious level, and adjustments are therefore required in order for patterns to be sized correctly. The total exposure dose is the sum of incident and backscattered electrons [14]. Thus, dose that a pattern feature receives is affected by neighboring electrons scattering. Therefore, dose factors for each single feature must be evaluated correctly before performing the lithography process (Table 3.3).

There are some kinds of commercial software developed specially for estimation and adjustment of the proximity effect and scattering, for instance Casino [15]. Casino software helps theoretically predict the unexpected scattering of electrons during the process of lithography, choosing an appropriate acceleration voltage for the electron beam (Fig. 2.7).

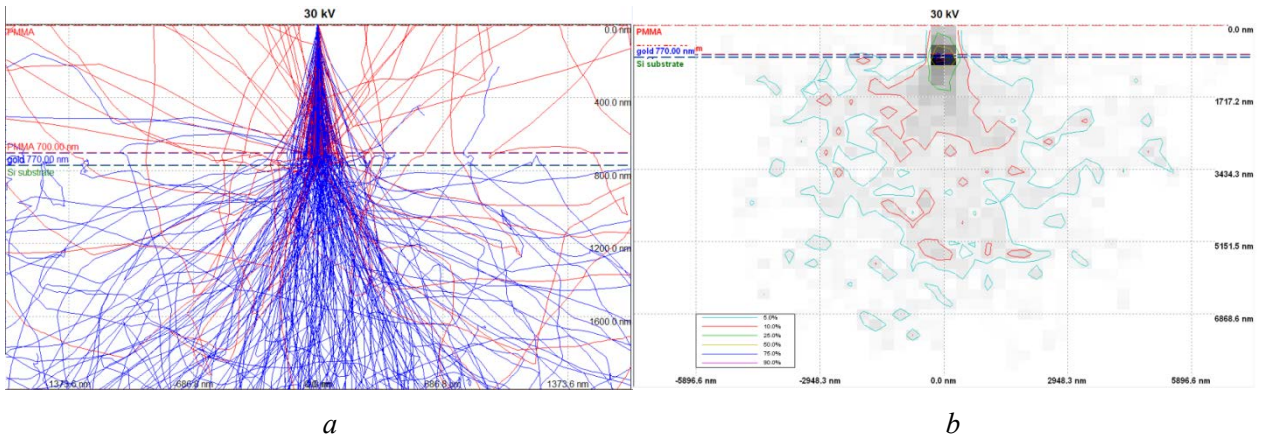


Figure 2.7 Simulation of a scattering phenomena inside the PMMA thin film using Casino software. Simulation performed for 30 kV, 700 nm PMMA, 70 nm Au and 2  $\mu\text{m}$  Si: a) scope of probable electron trajectories; b) accumulation of probable electron energies during back-scattering phenomena.

The cross-sectional drawing of the optical column of Electron Beam gun for EBL and SEM systems is represented in figure 2.8 a. It consists of the necessary all parts to direct precisely the electron beam for scanning over the surface of the substrate: filament, Wehnelt cylinder, anode, stigmators, beam blanking unit, condenser lens, beam control unit, objective aperture, objective lens and the movable stage, where the substrate with the sensitive to electron beam material is placed on.

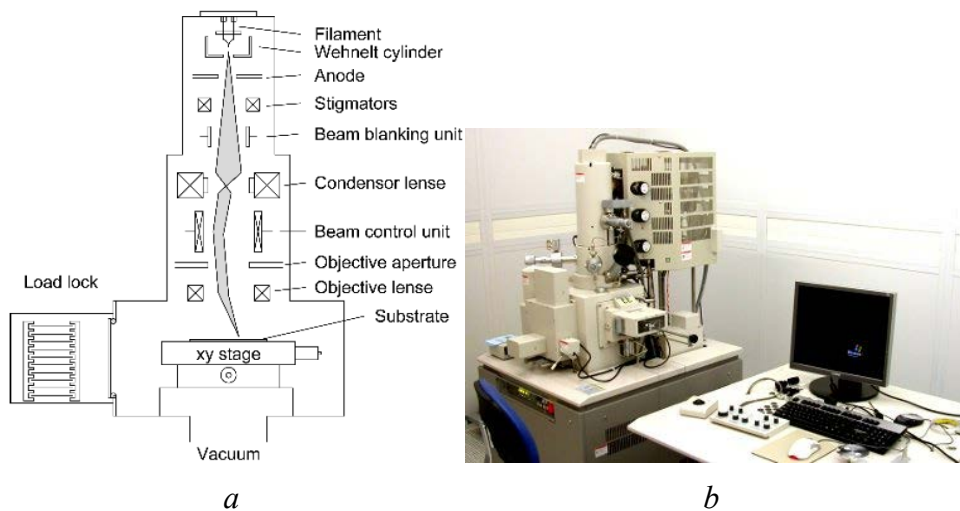


Figure 2.8 a) Cross-sectional view of the electron-optical column of an electron-beam writer [17] b) Raith ELPHY Quantum [16]; Hitachi S-4800 equipment for EBL-SEM experiments [18].

During the fabrication step and analysis of fabricated substrates Hitachi S-4800 equipment (Fig. 2.8 b) for EBL-SEM experiments was used.

The system can expose with energies up to 30 kV and can cover an area of 100 x 100  $\mu\text{m}$  without stitching. Depending on the resist and processing conditions, the system can write structures with dimensions down to a few tens of nanometers [18]. Voltage of 30 kV and current of 1  $\mu\text{A}$  were chosen.

Scanning Electron Microscopy was operated on a less electron beam voltage about 1 kV and current 10  $\mu\text{A}$  for analysing the fabricated gold nanoarrays on a gold substrate. Dimensions of each triangle, rectangle and square, pitch distance between nanoparticles were measured and uniformity of edges and sharpness of the corners were estimated. Results are represented in the Results and Discussions part of the thesis.

## 2.4 Lift-Off

The last step of plasmonic structures fabrication is lift-off. The samples with patterned resist and 55nm of gold thin film deposited on the top using Electron Beam Evaporation technique are immersed in the Remover PG and left for several hours (10 or more) to completely remove the resist from the substrates. Thus, the nanoparticles: triangles, rectangles and squares are left on the gold substrate and can be covered with thin layers of Polymethylmethacrylate (A4 950, A2 950 PMMA) using spin-coating technique described in the 2.2 part for further ablation using femtosecond laser pulses.

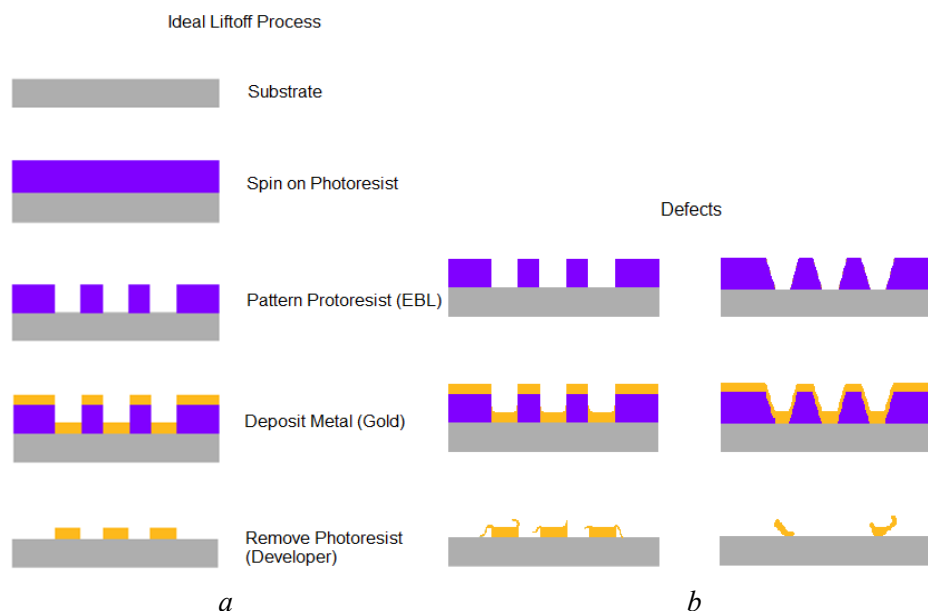


Figure 2.9 Cross-sectional drawing of the Lift-off Process: a) an ideal Lift-off process; b) Possible defects;

To avoid defects it is possible to use thicker layer of PMMA, thus perform spin-coating on a lower speed. If sidewalls of Photoresist are not perpendicular and  $> 90^\circ$  (Fig. 2.9 b) metal will be continuously deposited and no separation between desired and undesired metal takes place. If the metal comes alongside the resist sidewalls it is high probability that it will fall down to the substrate in an undesirable location after removing the resist (Fig. 2.9 b).

## 2.5 Profilometry

To estimate desirable thin film layers of PMMA spun onto the substrates, Profilometry technique of thin film measurements was performed. Veeco Dektak 150 Stylus Profiler (Fig. 2.10) at the NanoSYD cleanroom was used.

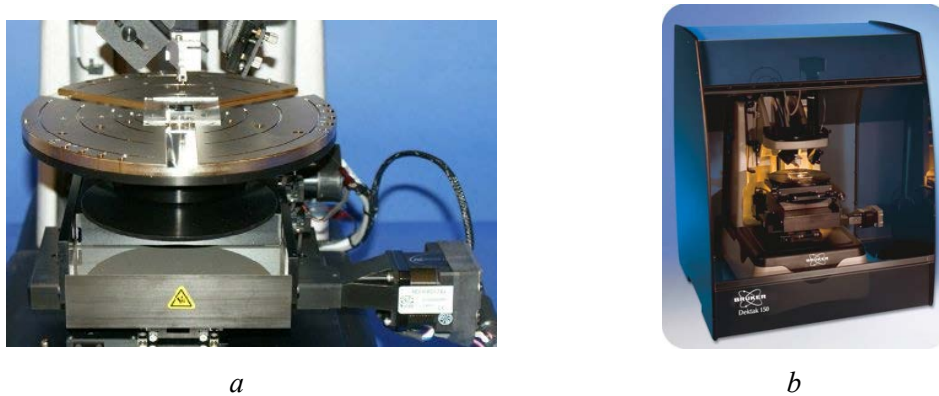


Figure 2.10 a) Profilometer sample stage [19]; b) Veeco Dektak 150 Stylus Profiler [20];

Profilometer is equipment, which measure either surface profile in nanometer range or roughness of it. Vertical resolution is observed in nanometer range. Lateral resolution is controlled by the scan speed and data signal sampling rate, and is usually poorer than the vertical one. A diamond tip of stylus with a radius ranges from 20 nm to 25  $\mu\text{m}$  moves both vertically, maintaining the contact with a sample according a specified force (range from 1 to 50 milligrams), and laterally across the surface of the sample according a specified distance. Thus, a profilometer is able to measure small variations of vertical features (from 10 nm to 1 mm) of surface roughness with vertical displacement of stylus as a function of position. During vertical displacement of stylus, an analog signal is being generated and converted into a digital one, which is then stored, analyzed and displayed in a PC screen, using commercial software for the profilometer operation [19].

Table 2.1

Thin film thickness variations applying different rotation speeds during spin-coating process. Measurements has been performed using Veeco Dektak 150 Stylus Profiler

Material	Rotation speed, rpm	Final Thickness, Å
A4 950 PMMA	4000	2250
A4 950 PMMA	5000	2100
<b>A4 950 PMMA</b>	<b>7000</b>	<b>2000</b>
<b>A2 950 PMMA</b>	<b>3000</b>	<b>800</b>
A2 950 PMMA	3500	720
A2 950 PMMA	4000	650

Where, extra bold assigned values have been chosen in order to provide optimum sensitive to Near-Field Enhancements of gold substrate thicknesses of PMMA layers for further ablation by femtosecond laser.

According to theoretical thin film thickness evaluation, using graph in figure 2.6 a., and measured thin film thickness values by profilometer (table 2.1), an appropriate rotation speed has been chosen in order to provide thick enough layer for further ablation, which will provide satisfied results and not damage gold nanostructures from the bottom (section 2.2).

## 2.6 Atomic Force Microscopy

Atomic Force Microscopy (Fig. 2.11) is versatile device which can be used for imaging different types of materials. It supports various mode operations: contact (repulsive) mode; non-contact/intermittent contact (tapping) mode; phase mode [21]. The diamond tip of diameter of about 10 nm located on the cantilever of about 100-200  $\mu\text{m}$  long probes the surface at chosen scanning mode. Contact between the tip and scanned surface cause forces of about  $10^{-8}$ - $10^{-6}$  N, therefore cantilever is deflected with respect of scanned surface roughness. At the same time, variations of deflections are registered by detector thus allowing for surface topography mapping at computer screen.

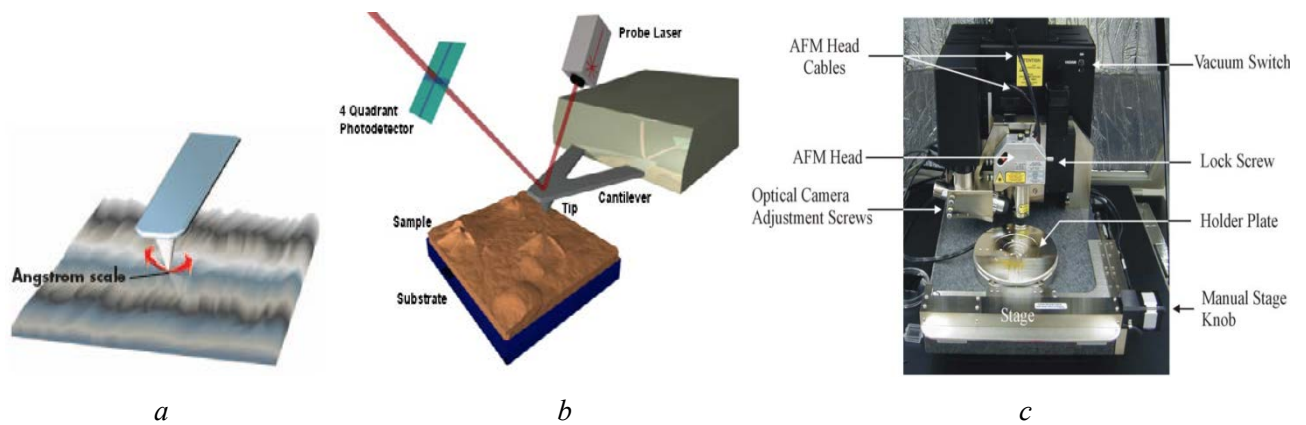


Figure 2.11 a) AFM cantilever image [22] b) Schematic representation of AFM process [23]; c) Veeco Dimension 3100 AFM used in experiments [24]

## 2.7 LSM and SHG Measurements

Second-Harmonic Generation (SHG) method in form of two-photon emission has been performed. When intense light irradiates a sample electrons leave it and optical response data of the sample is collected. Irradiation light in form of photons gives additional energy to electrons inside material of the sample. When any single photon is absorbed by the sample, electron of the sample changes its energy and jumps from the lower to higher energy states and back to the lower energy state, emitting a photon of the same energy as absorbed photon has. In another hand, this electron can take energy of two photons and emit off the sample in form of photon with twice an energy and been collected then by a photomultiplier or spectrometer. The probability of two-photon event is very low, therefore a high intensity femtosecond laser pulses has to be applied [25]. The key benefits of ultra-short laser pulses lie in their ability to produce very high peak power intensity and deliver energy into a material before thermal diffusion occurs [26].

Laser Scanning Microscopy experiment at Nanooptics Laboratory in Sønderborg is briefly explained in this part. All theoretical aspects are adopted in a reference with PhD thesis of Christian Maibohm (University of Southern Denmark) [27], where LSM equipment is explained in details.

Eclipse TE2000-U/laser scanning microscope (Fig. 2.13 b) was used to get an images of optical near-fields response from fabricated nanostructures. Spectra Physics Tsunami Ti: Sapphire femtosecond pulsing laser was used as an incident electromagnetic excitation source. The centre wavelength of wide pulsing Gaussian shape (Fig. 2.13 a), indicating that laser is pulsing at femtosecond regime, was set manually at 790 nm by changing the mirrors position of laser optical cavity. Figure 2.12 represents schematic drawing of optical setup for laser beam path [27].

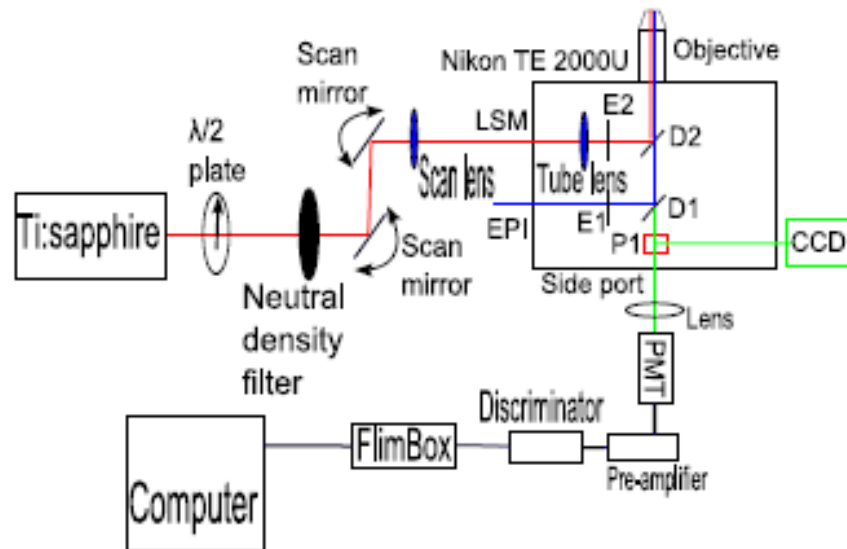
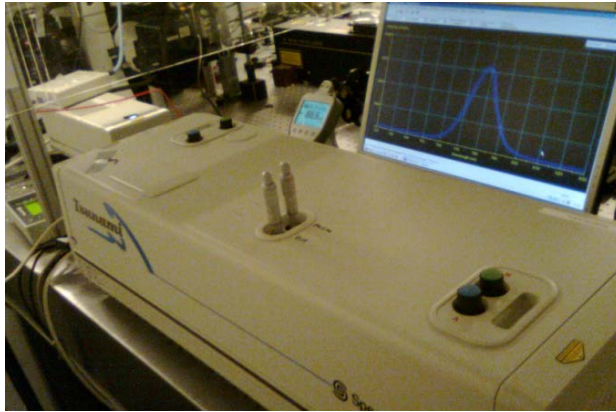


Figure 2.12 Schematic drawing of optical setup for laser beam path (red: two photon excitation path), consisting of: M-guiding mirrors; OI-optical isolator;  $\lambda/2$ -lambda-half plate; F1-neutral density filter; PM-two periscope mirrors; Keplerian telescope setup: SM-scanning mirrors; scan and tube lens; and inverted microscope setup: E1-excitation filter (340-380 nm), D1-dichroic mirror (400 nm); E2-emitter filter (350-650 nm); green color – detection path with P1-port selecting prism and CCD camera [27].

Laser light with a pulse length of sub 100 fs is directed by guiding mirrors (M) to a lambda-half wave plate ( $\lambda/2$ ) through an optical isolator, which prevents unwanted feedback to optical cavity of the laser, therefore ensuring safety for the pulsing regime. Lambda-half wave plate ( $\lambda/2$ ) is used to control the power of laser beam. Two periscope mirrors (PM) are used to raise the beam to the level of scanning mirrors (SM, a galvanometric scanners 6210H from Cambridge Technology) where the parallel beam is then created and directed through the lenses and objective to scan over the surface of the sample. An excitation filter E1 and a dichroic mirror (D1) are used to center the single photon at 365 nm of EPI-mercury lamp as an excitation source for microscope. An emitter filter (E2) is used for effectively block the excitation light and provide only a certain optical information to be detected from the sample [27]. To control the process and the position of scanning mirrors the computer software “Globals for imaging” by Enrico Gratton was used. The scanning area is determined by the applied voltage to the SM, it could vary for instance from 100 till 2000 mV. For 2000 mV the area of scanning is set equal to  $68.3 \times 68.3 \mu\text{m}$ . Therefore, it is easy to evaluate the dimensions of any other scanning areas belonged to applied voltage variations [27].

The optical response of electromagnetic radiation from the sample passing through the objective and emission filter is sent either to CCD camera or Photomultiplier. Hamamatsu R585 Photomultiplier working in a photon counting regime is used to send the photo current to a pre-amplifier ESN electronic VT110 CH4 and then to a constant fraction discriminator Phillips

Scientific model 6915 which converts the signal into TTL signal. Then the TTL pulses are collected by a field-programmable gate array which is connected to a computer to image the scanned area by “Globals for imaging” software [27].



a



b

Figure 2.13 a) Femtosecond laser beam of wide pulsing Gaussian shape; b) Eclipse TE2000-U/laser scanning microscope

## 2.8 Laser ablation of PMMA

Femtosecond laser pulses irradiated near-field optics of gold nanostructures can be quantified analytically implementing set of equations, describing different physical phenomena. However, this project describes another approach of near-field data gathering from gold nanostructures. The idea starts with covering fabricated gold nanostructures with a two different thicknesses of polymethyl methacrylate (PMMA) thin films.

To transfer a very high power  $P_{peak}$  to the PMMA material and enable of it ablation, femtosecond laser emitting light in a series of pulses [28] of duration  $\tau \approx 100$  fs and repetition rate  $R \approx 82$  MHz [29] was used. While continuous wave (cw) laser emits a steady beam of light with a constant power, the pulsed laser has its both  $P_{peak}$  and  $P_{avg}$ . It can be estimated as follows (equations 2.1 and 2.2):

$$P_{avg} = P_{peak} \times D \text{ (Joules/sec or Watts);} \quad (2.1)$$

where, D is dimensionless duty cycle (equation 2.3).

$$P_{avg} = E \times R \text{ (Joules/sec or Watts);} \quad (2.2)$$

where, E is energy per pulse (equation 2.4).

$$D = R \times \tau \text{ (dimensionless); Duty cycle} \quad (2.3)$$

$$D = 8 \cdot 10^{-6} = 80 \cdot 10^6 \cdot 100 \cdot 10^{-15} ; \tau \text{ is pulse width} < 100 \text{ fs (Table 2.2)}$$

$$E = \frac{P_{avg}}{R} = \frac{700mW}{80MHz} = 8 \text{ (nJoules);} \quad (2.4)$$

Peak and average power can be taken from the table 2.2 or calculated theoretically using equation 2.2:

$$P_{avg} = E \times R = 8 \cdot 10^{-9} \times 80 \cdot 10^6 = 640 \cdot 10^{-3} \text{ (Joule/sec or Watt)}$$

where,  $8 \cdot 10^{-9}$  is energy per pulse (Joule) (equation 2.4) and  $80 \cdot 10^6$  is repetition rate of femtosecond pulses (Table 2.2). Finally, peak power is:

$$P_{peak} = \frac{640 \cdot 10^{-3}}{8 \cdot 10^{-6}} = 80 \cdot 10^3 \text{ (Joule/sec or Watt)}$$

Table 2.2 [31]

Operation parameters of femtosecond pulsing Spectra Physics Tsunami Ti: Sapphire laser

	720 nm	790 nm	850 nm	950 nm	1050 nm <sup>2</sup>
<b>Average Power<sup>3</sup></b>					
Millennia Xs	700 mW	1.4 W	1.2 W	400 mW	250 mW
Millennia Vllls	500 mW	1.1 W	900 mW	250 mW	N/A
Millennia Vs	300 mW	700 mW	500 mW	100 mW	N/A
<b>Peak Power<sup>3</sup></b>					
Millennia Xs	> 65 kW	> 170 kW	> 145 kW	> 48 kW	> 24 kW
Millennia Vllls	> 47 kW	> 134 kW	> 109 kW	> 30 kW	N/A
Millennia Vs	> 28 kW	> 85 kW	> 61 kW	> 12 kW	N/A
<b>Pulse Width<sup>3,4</sup></b>	< 130 fs	< 100 fs	< 100 fs	< 100 fs	< 130 fs
<b>Tuning Range</b>					
Millennia Xs		700–1000 nm			970–1080 nm
Millennia Vllls		700–1000 nm			N/A
Millennia Vs		710–980 nm			N/A
<b>Repetition Rate (nominal)<sup>5</sup></b>			80 MHz		
<b>Noise<sup>6</sup></b>			< 0.2%		
<b>Stability<sup>7</sup></b>			< 5%		
<b>Spatial Mode</b>			TEM <sub>00</sub>		
<b>Beam Diameter at 1/e<sup>2</sup> points</b>			< 2 mm		
<b>Beam Divergence, full angle</b>			< 1 mrad		
<b>Polarization</b>			> 500:1 vertical		

Pulsing laser beam of Gaussian shape parameters are represented graphically (Fig. 2.14):

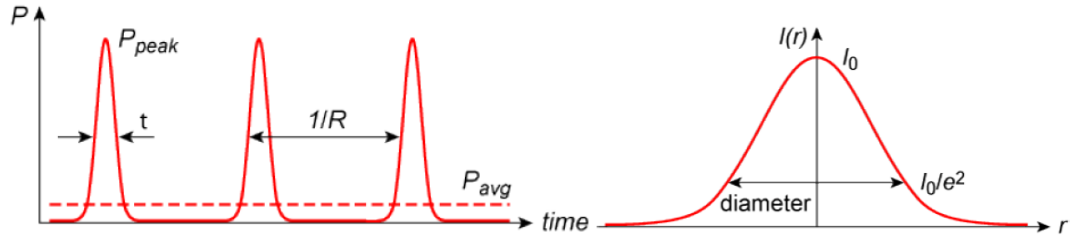


Figure 2.14 Laser beam parameters:  $P_{peak}$  is a peak power,  $I_0/e^2$ - intensity point [28]

It is mentioned in section 2.2, that samples have been covered with PMMA thin layers for ablation. Equation 2.5 [32] represents the possibility of threshold fluence calculation using ablated diameter of PMMA.

$$D^2 = 2\omega_0^2 \ln\left(\frac{F_0}{F_{th}}\right); \quad (2.5)$$

where,  $D^2$  is the square diameter D of laser-processed hole [32];

$\omega_0$  is a Gaussian focal beam radius equal to 600 nm [29];

$F_0$  is a peak fluence or maximum laser fluence, which is estimated from equation 2.6:

$$F_0 = \frac{2E_{pulse}}{\pi\omega_0^2} = \frac{2 \cdot 8 \cdot 10^{-9}}{\pi \cdot 360000 \cdot 10^{-14}} = 1.4 \text{ Joule/cm}^2; \quad (2.6)$$

where,  $E_{pulse}$  is an incident laser pulse energy [31] equal to 8 nJ (equation 2.4).

Using equation 2.7 fluence threshold for the measured ablated diameter of 0.4  $\mu\text{m}$  for A4 PMMA (Table 3.5 image Nr. 16) can be evaluated theoretically:

$$D^2 = 2\omega_0^2 (\ln F_0 - \ln F_{th}); \quad (2.7)$$

Where,  $\ln F_0 = \ln 0.84$ , taking into account that the laser fluence coming to ablation area after the  $\lambda/2$  plate decrease of about 40% when passes through inverted microscope setup.

$$\ln F_{th} = \ln x; \quad \ln x = \log_e(x) = y; \quad (2.8)$$

y can be defined as follows:

$$y = \frac{2\omega_0^2 \ln F_0 - D^2}{2\omega_0^2} = -0.39;$$

where, D is measured ablated area = 0.4  $\mu\text{m}$ ;

$\omega_0$  is a Gaussian focal beam radius equal to 600 nm [29];

$F_0$  is a peak fluence or maximum laser fluence  $J/cm^2$ ;

Therefore,

$$F_{th} = e^y \quad (2.9)$$

$$F_{th} \approx 0.68 J/cm^2;$$

This value of threshold fluence would be roughly estimated for A4 PMMA, using experimentally found ablation diameter and maximum fluence of used laser, in the case if ablation were performed from the top of PMMA [32] covered onto 450x450 nm nanosquares without taking into account the field enhancement factor and plasmon oscillations of gold nanostructures. Fluence threshold value 0.68  $J/cm^2$  is related to 1,9 nJ of pulse energy (equation 2.10) and proportionally related to  $\approx 166$  mW of ablation power, if 700 mW for 8 nJ of pulse energy from 2.2 table is taken as 100%.

When laser beam spot comes to ablation surface after passing through inverted microscope setup it loses about 40% of its energy. The maximum power of laser beam after  $\lambda/2$  plate was measured using powermeter and it is equal to 400 mW. Therefore, if the maximum power comes to the ablation surface after inverted microscope setup it is equal to 240 mW. Focal spot area  $A$  for laser beam of 600 nm radius is equal to [27]  $2.826 \cdot 10^{-9} cm^2$ .

From the 2.2 table average power of <100 fs pulsing laser with energy per pulse of 8 nJ is equal to 700 mW. Assuming minimum 60 mW power (Table 3.5 image Nr.16) for ablation estimated practically for A4 PMMA of 450x450 nm squares, energy for this case is proportionally calculated and equal to 0.68 nJ. Threshold fluence could be roughly estimated from equation 2.10:

$$Fluence \left( \frac{J}{cm^2} \right) = \frac{Energy \ of \ laser \ pulse \ (nJ)}{focal \ spot \ Area \ (cm^2)}, \quad (2.10)$$

and it is equal to:

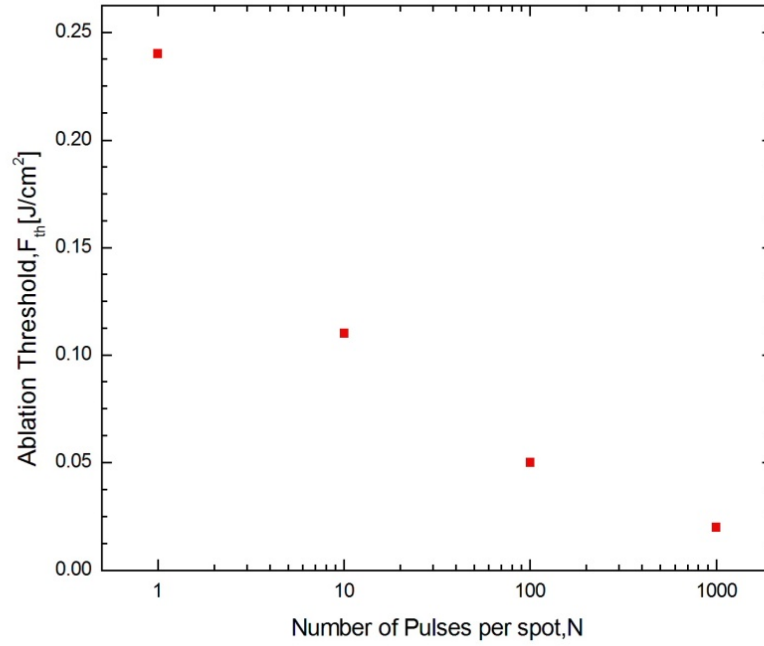
$$F_{th} \left( \frac{J}{cm^2} \right) = \frac{0.68}{2.826} = 0.24; \quad (2.11)$$

This value is about 65% less than it is estimated using equation 2.7.

Relation between the single pulse threshold  $F_{th}(1)$  and the threshold  $F_{th}(N)$  for applied  $N$  laser pulses on the same spot is represented in equation 2.12 [30]:

$$F_{th}(N) = F_{th}(1)N^{\xi-1} \quad (2.12)$$

where,  $\xi$  is an incubation parameter of PMMA or strength of accumulation and it is equal to 0.67 [30].



Graph 2.1 Ablation threshold fluence dependence on number of pulses per spot.  $F_{th} \approx 0.24 J/cm^2$  is experimentally measured fluence, while other values are estimated according equation 2.12.

$F_{th} \approx 0.24 J/cm^2$  is calculated typically for one day and certain case of ablation, depending on certain conditions according ablation experiment. It is not precisely estimated, due to many factors influence on this value, for instance, how old the PMMA layer is at the moment of ablation, thickness of PMMA layer, laser pulse duration and stability, surroundings temperature, humidity and etc. Pulse duration was not monitored. It is only known, that the value is  $<100$  fs (Table 2.2), if not the acoustic optical modulator of Ti:sapphire laser does not work and no pulses are produced.

### 3. EXPERIMENTAL RESULTS

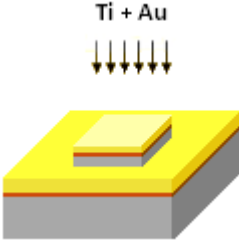
This chapter represents detailed explanation and structural drawing of each fabrication step of plasmonic substrates. SEM images of fabricated plasmonic substrate geometries and ablated PMMA layers are represented. AFM images of surface topography of plasmonic substrates are also included. Ellipsometry optical data, LSM fluorescence images and Second-Harmonic Generation graph are attached. EM Explorer software images of Near-Field Intensities on plasmonic substrates after 790 nm incident light irradiation are demonstrated.

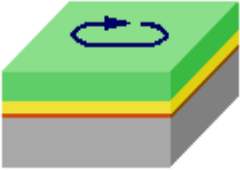
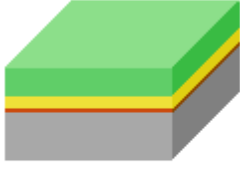
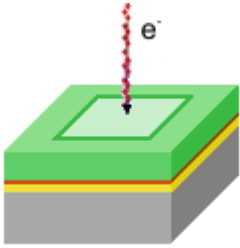
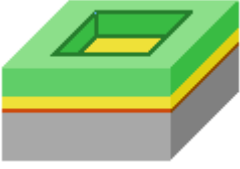
#### 3.1 Fabrication steps

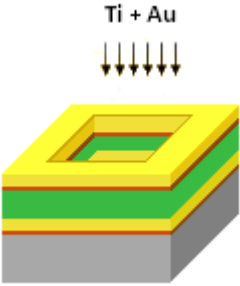
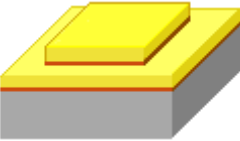
Table 3.1 summarizes all relevant fabrication steps with accompanying structural drawings for each fabrication step.

Table 3.1

Structural drawings of fabrication steps

Nr.	Structural View	Description
0		<p><i>Elevated platform fabrication</i></p> <p>Starting Si wafer are single-side polished, <math>t \sim 525</math> nm</p>
1	 <p>Gray-silicon;</p>	<p><i>Preparation of starting substrates</i></p> <p>Silicon substrates 5mm x 5mm; 9 platforms 200 x 200 <math>\mu</math>m and 1 <math>\mu</math>m of thickness;</p>
2	 <p>Yellow-gold; Red-Ti;</p>	<p><i>Ti/Au deposition by electron beam evaporation.</i></p> <p><i>Polyteknik Cryofox Explorer 600</i></p> <p>Ti – 2 nm; Deposition rate is 1 <math>\text{\AA}/\text{sec}</math>; tooling factor 89; Au - 70 nm; Deposition rate is 2 <math>\text{\AA}/\text{sec}</math>; tooling factor 67;</p>

3	 <p>Green-PMMA;</p>	<p><i>Spin-coating of EBL resist</i></p> <p>1 step) 5 s at 1000 rpm, ramping 1500 rpm/s and acceleration of 50 000 rpm/s<sup>2</sup> –uniform and smooth covering of the surface;</p> <p>2 step) 45 s at 7000 rpm, ramping – 10000 rpm/s and acceleration of 50000 rpm/s<sup>2</sup> – covering of desirable thickness of thin film;</p>
4	 <p>200 deg C prebake</p>	<p><i>Prebake</i></p> <p>90 s of prebaking at 200°C – from liquid to solid (hardening of spinned on thin film);</p>
5		<p><i>Electron beam lithography</i></p> <p>V acc - 30 kV; I<sub>e</sub> – 1 μA;</p> <p>without proximity correction, but designing about 10 nm smaller geometry to enhance desirable final dimensions of each single nanostructure;</p> <p>Dose factors for 6 different arrays of triangles: 3.65; 3.7; 3.75; 3.65; 3.7; 3.75;</p> <p>rectangles: 3.15; 3.2; 3.25; 3.3; 3.35; 3.4;</p> <p>squares: 3.0; 3.05; 3.10; 3.15; 3.20; 3.25</p>
6		<p><i>Development</i></p> <p>Developer MIBK:IPA 1:3 for 40 sec;</p> <p>Stopper IPA (2-propanol) for 30 sec;</p> <p>then immediately dried using a N<sub>2</sub> gas gun before the wafer dries by itself</p>

7		<p><i>Ti/Au deposition by electron beam evaporation.</i> <i>Polyteknik Cryofox Explorer 600</i></p> <p>Ti – 2 nm; Deposition rate is 1 Å/sec; tooling factor 89; Au - 55 nm; Deposition rate is 2 Å/sec; tooling factor 67;</p>
8		<p><i>Lift-off</i></p> <p>Remover PG for several hours (10 or more); place it afterwards for 5 minutes in ultrasound</p>

Detailed explanation of each fabrication step:

0. Positive photolithography on the wafer polished side with “stamp test” mask: HDMS 120°C; spin on 1.5 μm photoresist (Resist AZ5214A) 500 RPM for 5 s, acc. 5000 rps<sup>2</sup>, 4000 RPM for 30 s, acc. 10000 rps<sup>2</sup>; 90°C, 60 s of baking; 4 s Exposure (“stamp test” mask); 22°C, 60 s Development (AZ351B developer); Rinse / dry in water for 2 minutes; ICP-RIE plasma etching for 30 seconds; Spin on resist 1.5 μm for dicing; Removal of resist; ~ 5 min in acetone and ~ 2 min rinse in water;

1. Silicon substrates with dimensions of 5mm x 5mm structurized with 9 platforms of 200 x 200 μm and 1 μm of thickness are cleaned up by placing in Acetone for 10 minutes and then agitated in ultrasonic Isopropanol bath for 5 minutes. Then samples are washed up in distilled water and dried up immediately by compressed N<sub>2</sub> gas;

2. After plasma cleaning for approximately 10 seconds samples are placed in Polyteknik Cryofox Explorer 600 for Electron Beam Evaporation of Ti (2 nm, evaporation rate 1 Å/sec; tooling factor 89) and Au (70 nm, evaporation rate 2 Å/sec; tooling factor 67);

3. After metals are deposited spin-coating of EBL resist is performed with a 2 step deposition set up: 1 step) 5 s at 1000 rpm, ramping 1500 rpm/s and acceleration of 50 000 rpm/s<sup>2</sup> – uniform and smooth covering of the surface; 2 step) 45 s at 7000 rpm, ramping – 10000 rpm/s and acceleration of 50000 rpm/s<sup>2</sup> – covering of desirable thickness of thin film;

4. After spin-coating is performed samples are placed on the hot-plate and being prebaked for 90 seconds at temperature of 200°C. Then, after 2-3 minutes samples are cooled down below its glass transition temperature. It enables for PMMA to change its state from liquid to solid.

5. Now samples are ready for EBL step. It is performed choosing regime with acceleration voltage of 30 kV and electron beam current of 1  $\mu$ A; Triangles, squares and rectangles structures are designed using ELPHY Quantum commercial software and dose factors for 6 different arrays on each platform of triangles: 3.65; 3.7; 3.75; 3.65; 3.7; 3.75; rectangles: 3.15; 3.2; 3.25; 3.3; 3.35; 3.4; and squares: 3.0; 3.05; 3.10; 3.15; 3.20; 3.25, were evaluated on a practice. It enables most sharp geometries for certain lithography conditions.

6. When EBL step is done, samples must be placed in developer MIBK:IPA 1:3 for 40 sec; and Stopper IPA (2-propanol) for 30 sec; It washes away all particles of PMMA destroyed by electron beam during EBL, creating mask for further metal deposition. After developing step samples are immediately dried using N<sub>2</sub> gas gun before it dries by itself.

7. Then, step 2 is repeated, however instead of 70 nm of Au, 55 nm is evaporated.

8. Lift-off procedure is performed by placing samples into Remover PG for several hours (10 or more) and for 5 minutes in ultrasonic bath. Plasmonic substrates are fabricated and could be tested optically. 6 arrays 50 x 50  $\mu$ m, consisting of approximately 66 squares, triangles with pitch distances of 750 nm by x and y axes, and 66 x 38 (x and y direction) rectangles with pitch distances of 1030 nm and 750 nm by y and x axes respectively, are structured on each 200 x 200  $\mu$ m and 1  $\mu$ m of thickness platform.

### 3.2 Optical Microscopy results

Optical microscope (Fig. 3.1) is convenient method for getting images and evaluating fabricated substrates. It is equipped with 5 objectives of different magnifications from 5 to 100 times.

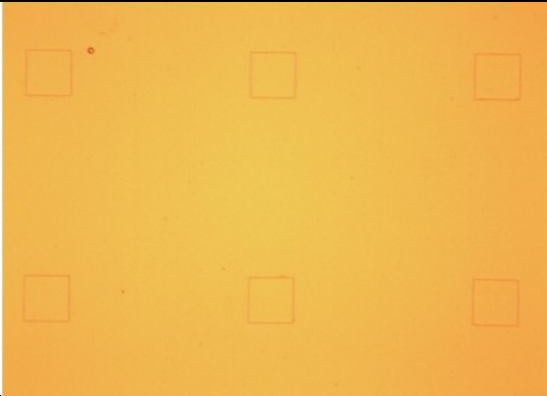
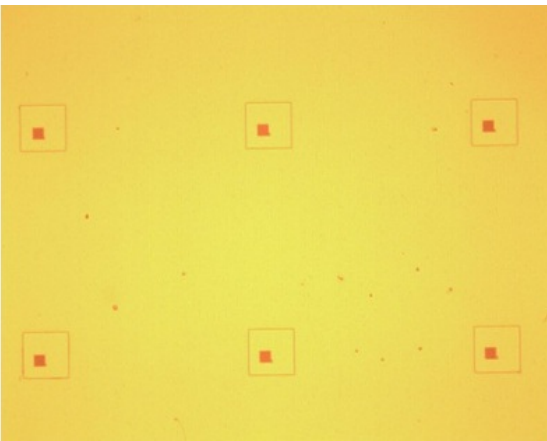
Table 3.2 represents optical microscopy images of the 2<sup>nd</sup>, 6<sup>th</sup>, 8<sup>th</sup> fabrication steps (3.1 table) and one single array with a number.

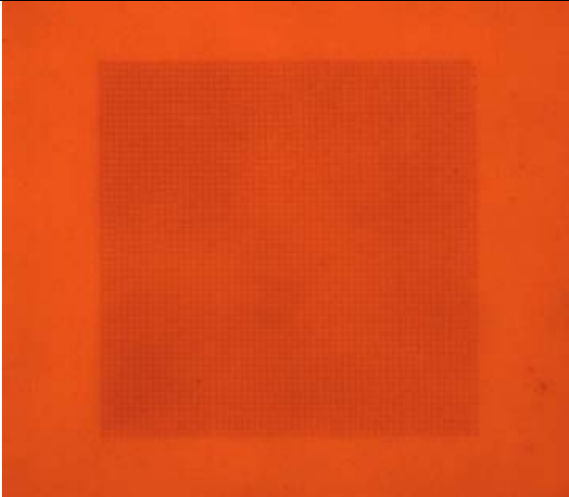
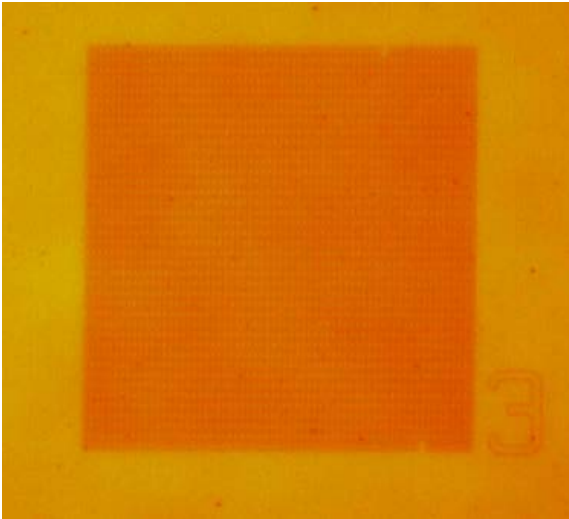


Figure 3.1 Optical microscope Nikon LV100D [33]

Table 3.2

## Optical Microscopy images of fabricated substrates

Sample	Image	Description
2 <sup>nd</sup> fabrication step		<p>6 platforms covered with 2 nm of Ti and 70 nm of Au. Each platform is 200 x 200 <math>\mu\text{m}</math> and 1 <math>\mu\text{m}</math> of thickness. x5 magnification</p>
6 <sup>th</sup> fabrication step		<p>6 platforms after EBL step. Substrate is covered with 2 nm of Ti, 70 nm of Au and approximately 200 nm of PMMA A4 EBL resist. Each platform is 200 x 200 <math>\mu\text{m}</math> and 1 <math>\mu\text{m}</math> of thickness. x5 magnification. Each array on a platform is 50 x 50 <math>\mu\text{m}</math>, consisting of approximately 66 mask for squares, triangles and 66 x 38 (x and y direction) rectangles. x5 magnification.</p>

8 <sup>th</sup> fabrication step		single array 50 x 50 $\mu\text{m}$ with approximately 66 triangles with dimensions of 450 x 450 nm and 55 nm of thickness, pitch distance is 750 nm by y and x axes.
Array Nr. 3		image of 3 <sup>rd</sup> array 50 x 50 $\mu\text{m}$ with approximately 66 x 38 (x and y direction) rectangles with pitch distances of 1030 nm and 750 nm by y and x axes respectively and 55 nm of thickness. Number of the array is located side by side in the right bottom corner.

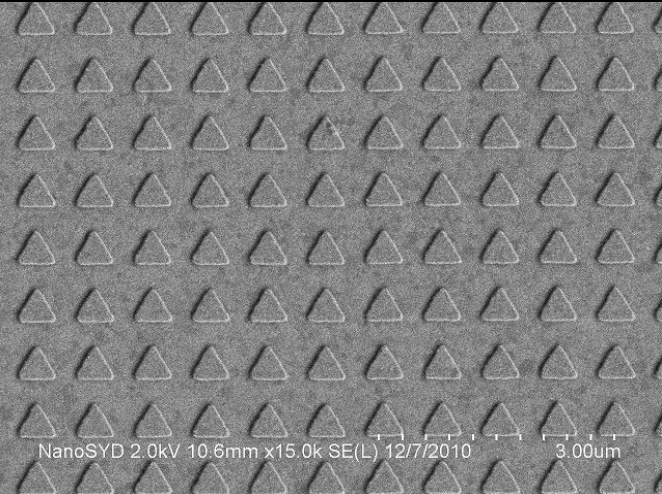
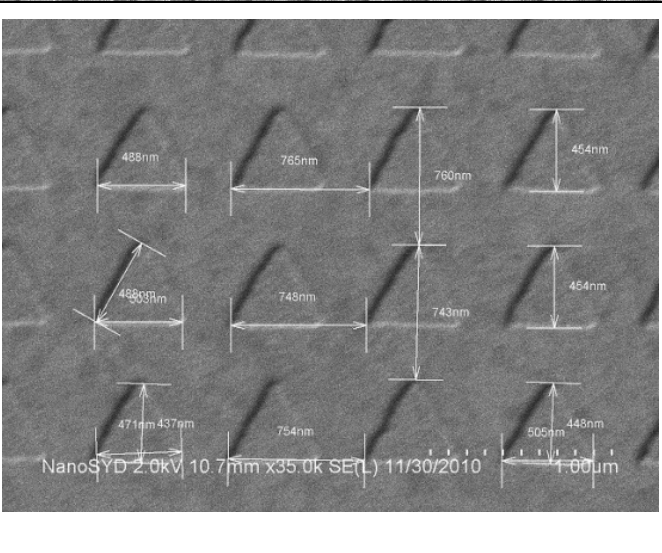
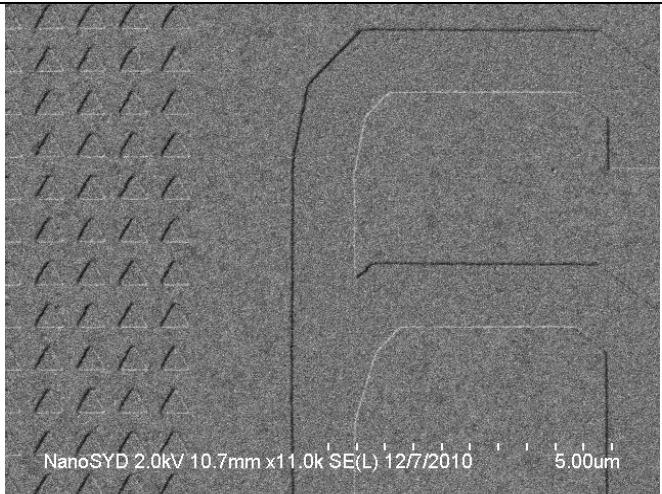
After each fabrication step, optical microscopy images of fabricated substrates have been taken. It allows fast and convenient inspection of evaporated gold layer homogeneity, scratches or contaminations presence revealing, and estimation if certain fabrication step has been successfully sustained.

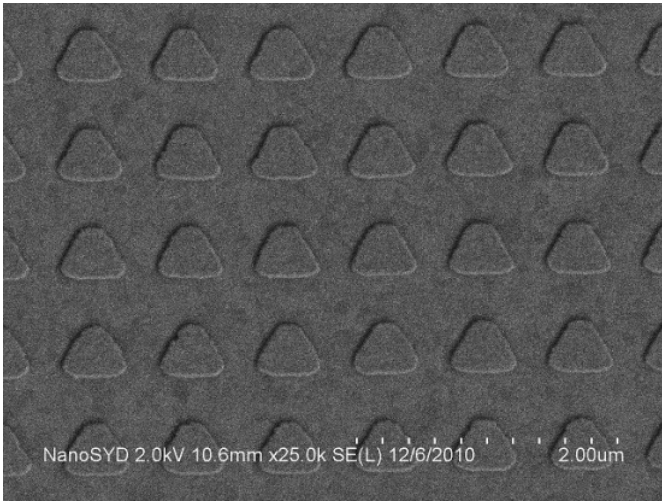
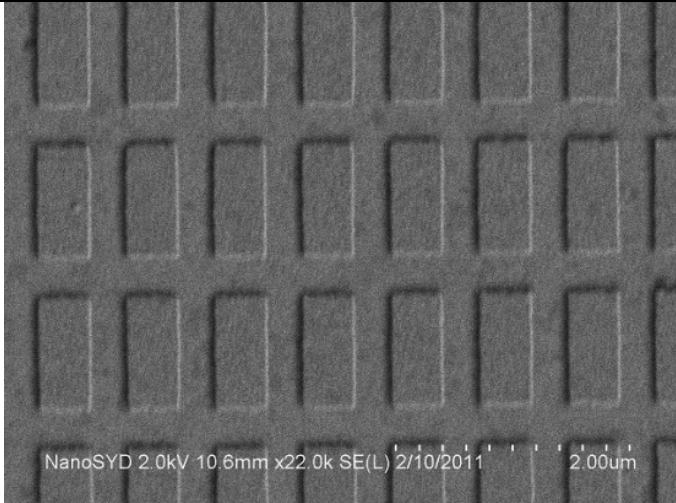
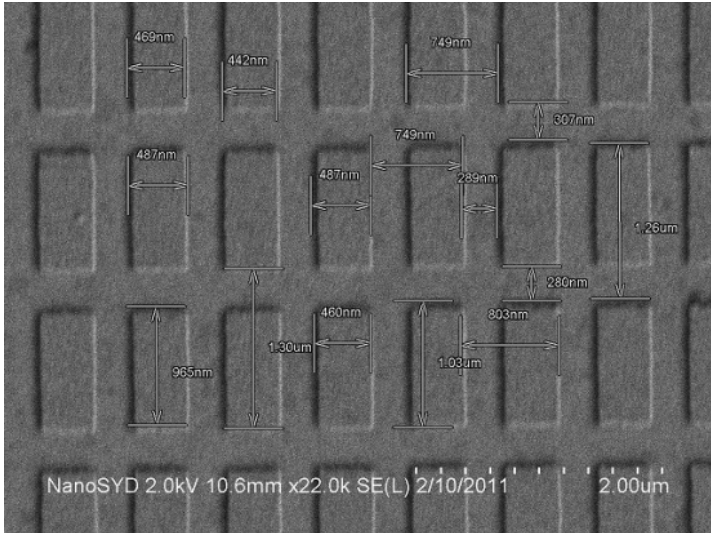
### 3.3 Scanning Electron Microscopy images of fabricated plasmonic substrates

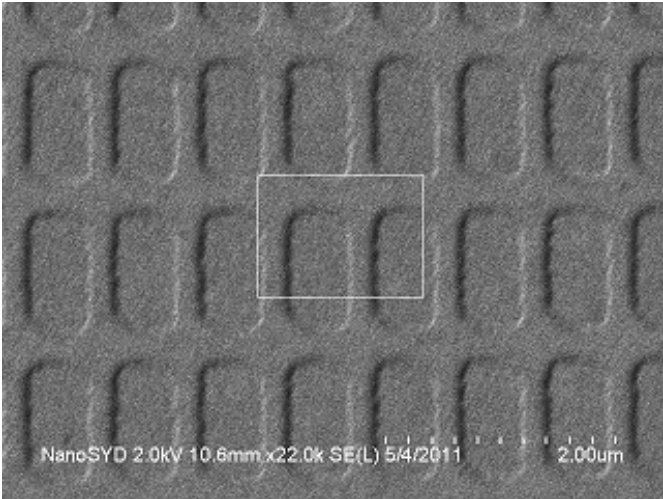
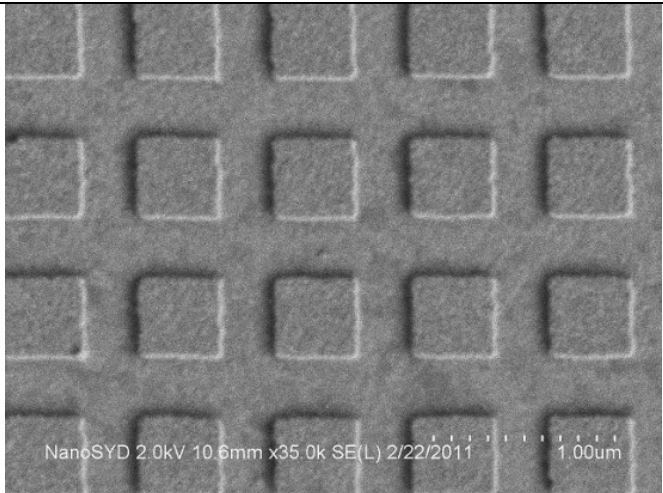
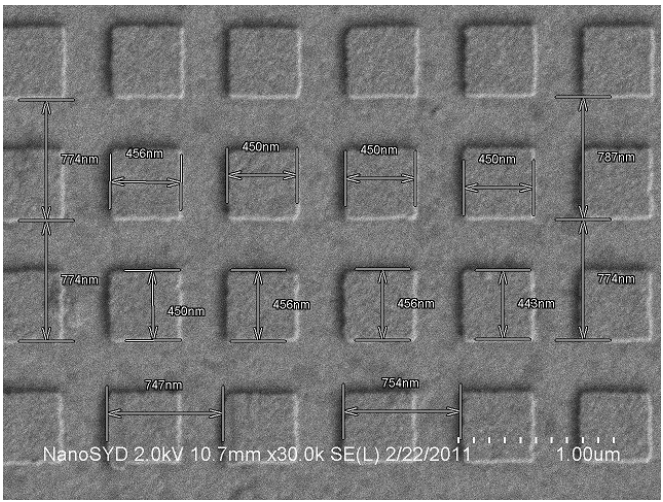
If electron beam parameters are set correctly, especially dose factors, it allows to get desirable geometry with sharp edges and suitable dimensions. Table 3.3 represents Scanning Electron Microscopy Images of fortunate and unfavorable dimensions of fabricated plasmonic substrates by Electron Beam Lithography technique.

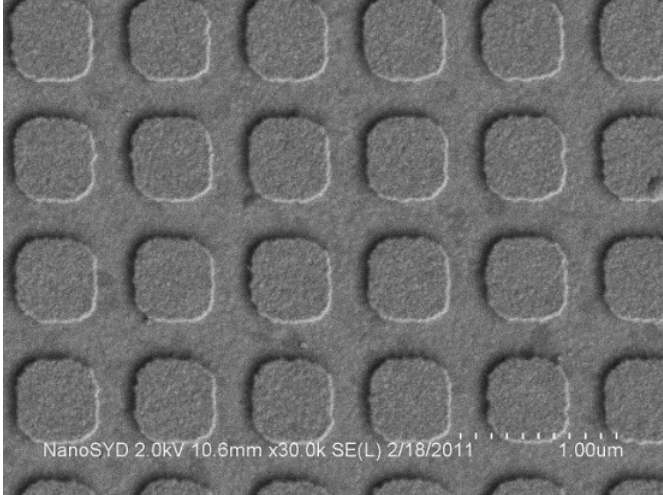
Table 3.3

## Scanning Electron Microscopy images of EBL fabricated substrates

Sample	Image	Description
Triangles ideal geometry: 450 x 450 nm Ideal period: x-y 750 nm;		SEM image of triangles array after well designed pattern and suitable lithography conditions. Magnification x 15.0k
		SEM image of triangles array magnificated 35.0k with dimension variations: 437 - 505 nm by x-y-axes of geometry and pitch distance: 743 – 765 nm by x-y-axes.
		SEM image of triangles array and a number indicating certain platform, magnificated 11.0k

		<p>Deformed shapes and round corners of rectangles: bad lithography conditions, especially wrong chosen dose factors.</p> <p>Magnification 25.0k</p>
<p>Rectangles ideal geometry: 450 x 900 nm Ideal period: x-750 nm; y-1030 nm;</p>		<p>SEM image of rectangles array after well designed pattern and suitable lithography conditions.</p> <p>Magnification x 22.0k</p>
		<p>SEM image of rectangles array magnificated 22.0k with dimension variations: 442 - 460 nm by x-axis of geometry, 965 nm-1.03 <math>\mu\text{m}</math> by y-axis and pitch distance: 749 - 803 nm by x-axis and 1.26 - 1.30 <math>\mu\text{m}</math> by y-axis.</p>

		<p>Deformed shapes and round corners of rectangles: bad lithography conditions, especially wrong chosen dose factors.</p> <p>Magnification 22.0k</p>
<p>Squares ideal geometry: 450 x 450 nm; Ideal period: x-y 750 nm;</p>		<p>SEM image of squares array after well designed pattern and suitable lithography conditions.</p> <p>Magnification x 35.0k</p>
		<p>SEM image of squares array magnificated 30.0k with dimension variations: 443 - 456 nm by x-y-axes of geometry and pitch distance: 747 – 774 nm by x-y-axes.</p>

		<p>Deformed shapes and round corners of squares: bad lithography conditions, especially wrong chosen dose factors.</p> <p>Magnification 30.0k</p>
--	--	---

There are many factors influencing on fabrication outcome. First of all, samples must be covered with well spinned smooth layer of PMMA EBL resist of correctly chosen thickness (Fig. 2.6. a).

Pattern design is important step if one wishes to obtain desirable dimensions of final array of nanostructures. In my case, I choose smaller geometries for pattern design in order to obtain larger structures after lithography is performed. It allows do not care so much about proximity effect, due to small enough patterns are being fabricated and electron scattering does not influence so much on the whole set of fabricated geometries. It has been observed that if design geometries smaller of about several tens (400 nm for triangles and squares, and x-axis of rectangles but 850 nm by y-axis) are set, the correct final ones are resulted (450 nm for triangles and squares by both axis and 450 nm by x-axis and 900 nm by y-axis for rectangles).

Electron beam optimization is also quite important thing during electron beam lithography step. Focusing well, astigmatism correction helps perform qualitative exposure by setting correctly electron beam on the sample.

Stage adjustment, such as origin correction and angle correction are necessary for sample navigation from one coordinate to another, and adjustment of desirable place for lithography.

Measurements of beam current by Faraday Cup were also performed before each lithography process. It enables stable cooperation of emitted electron beam current and the patterned resist if calculations for area, line and dot dwell times corresponding to the certain measured amount of current in nA are made. Suitable dose factors must be appointed for each certain array of nanostructures. In my case, different dose factors for 6 different arrays were assigned to catch the most appropriate value for the best dimensions. Such as, for example, in the case of triangles for the 1<sup>st</sup> array on the 1<sup>st</sup> platform it is 3.65; for the 2<sup>nd</sup> -3.7; 3<sup>rd</sup> - 3.75; 4<sup>th</sup> - 3.65;

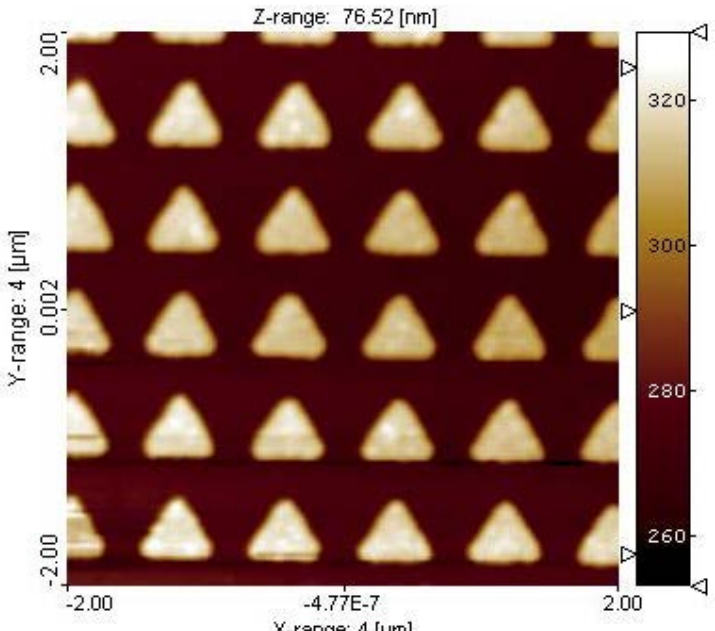
5<sup>th</sup> - 3.7; and 6<sup>th</sup> - 3.75. Afterwards, by obtaining images of fabricated structures, it has been noticed that for triangles the most suitable dose factor value is 3.65; for rectangles – 3.3; and squares – 3.05;

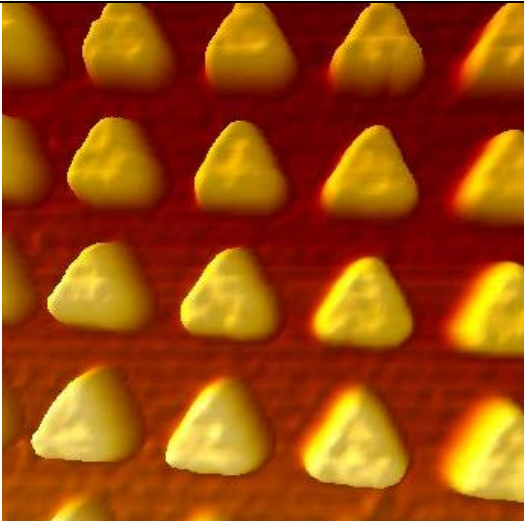
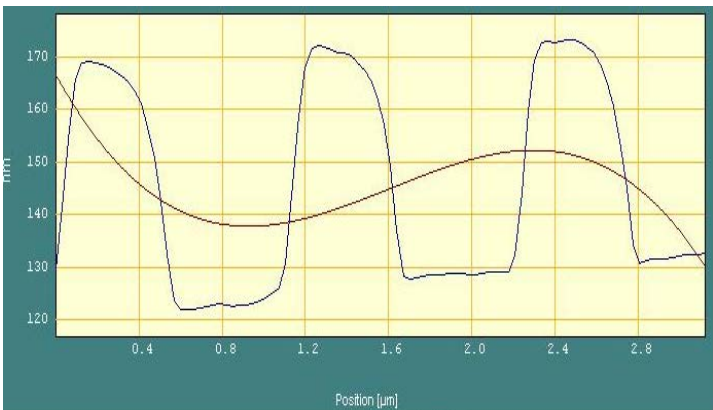
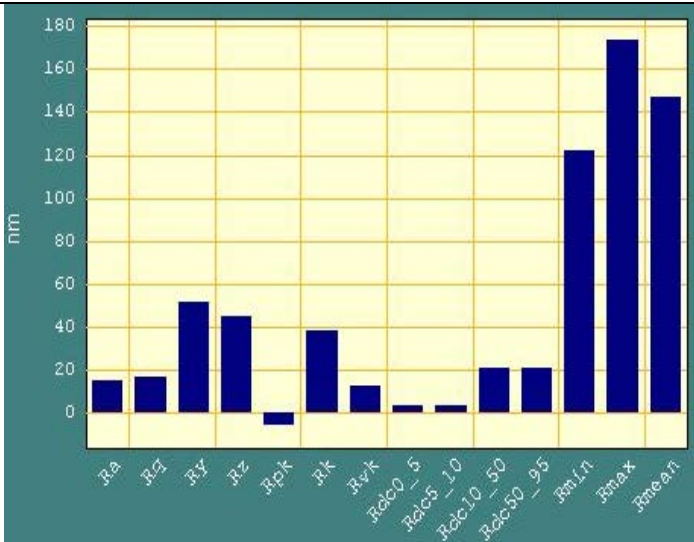
### 3.4 Atomic Force Microscopy results of fabricated plasmonic substrates

For atomic force microscopy 3 plasmonic substrates with different geometries of nanostructures have been chosen. Tapping mode is suitable for gold surfaces scanning applications. After placing the substrate on the holder plate and then loading it, finding a tip location over the sample and focusing on the surface in order to find desirable position for scanning, engage button was pressed. Probing over the surface under consideration by tapping mode was started and qualitative enough results of fabricated plasmonic substrates were obtained. Surface morphology, topography 2D, 3D images, surface roughness and heights variations are represented in table 3.4.

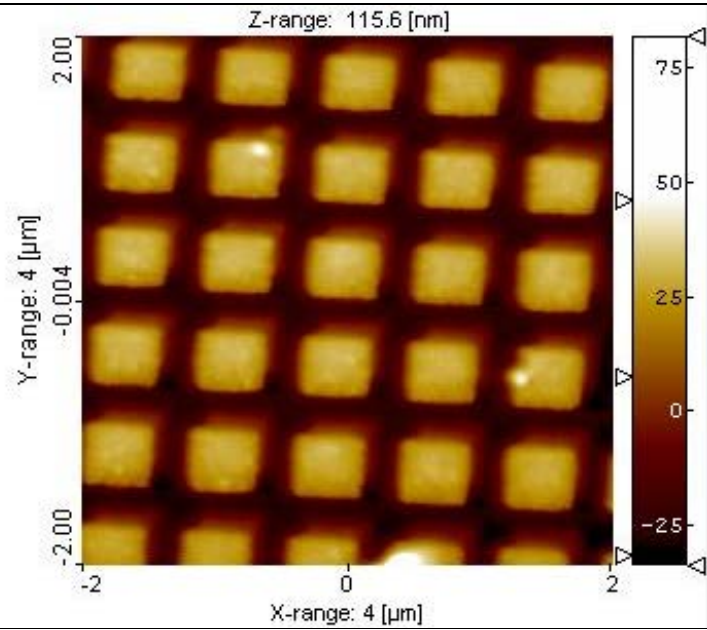
Table 3.4

AFM surface analysis of fabricated substrates

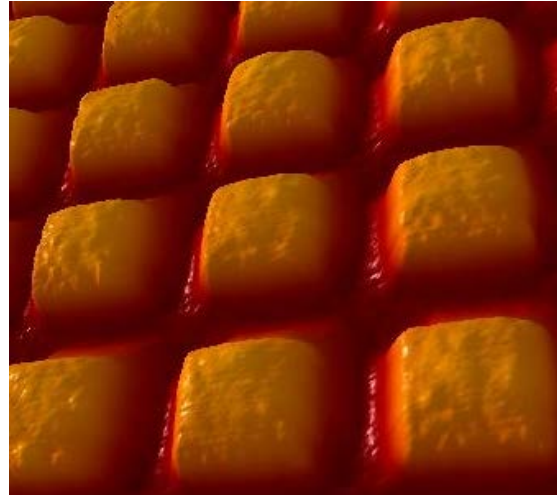
Sample	Image	Description
450 x 450 nm triangles, pitch distance 750 x 750 nm by x and y axes respectively		2D Topography image of triangles 4 x 4 μm

		<p>3D topography image of triangles 4 x 4 <math>\mu\text{m}</math></p>
		<p>Triangles heights vs. thickness: 55 nm and 450-500 nm dimension by x axis respectively</p>
		<p>Triangles roughness values, <math>R_z \approx 55 \text{ nm}</math></p>

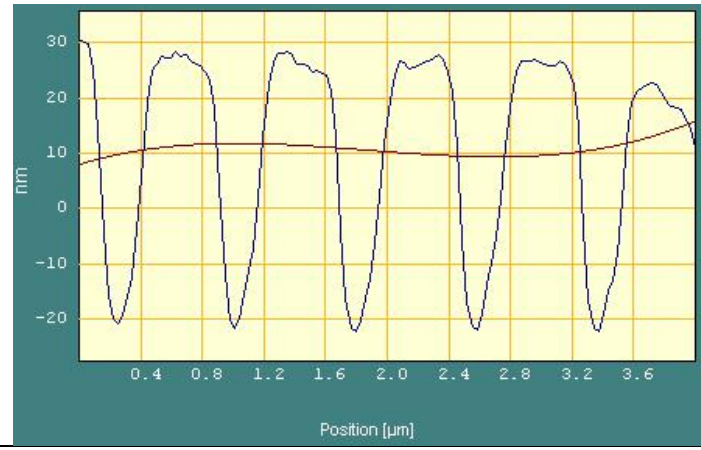
450 x 450 nm squares, pitch distance 750 x 750 nm by x and y axes respectively



2D  
Topography  
image of  
squares  
4 x 4 μm

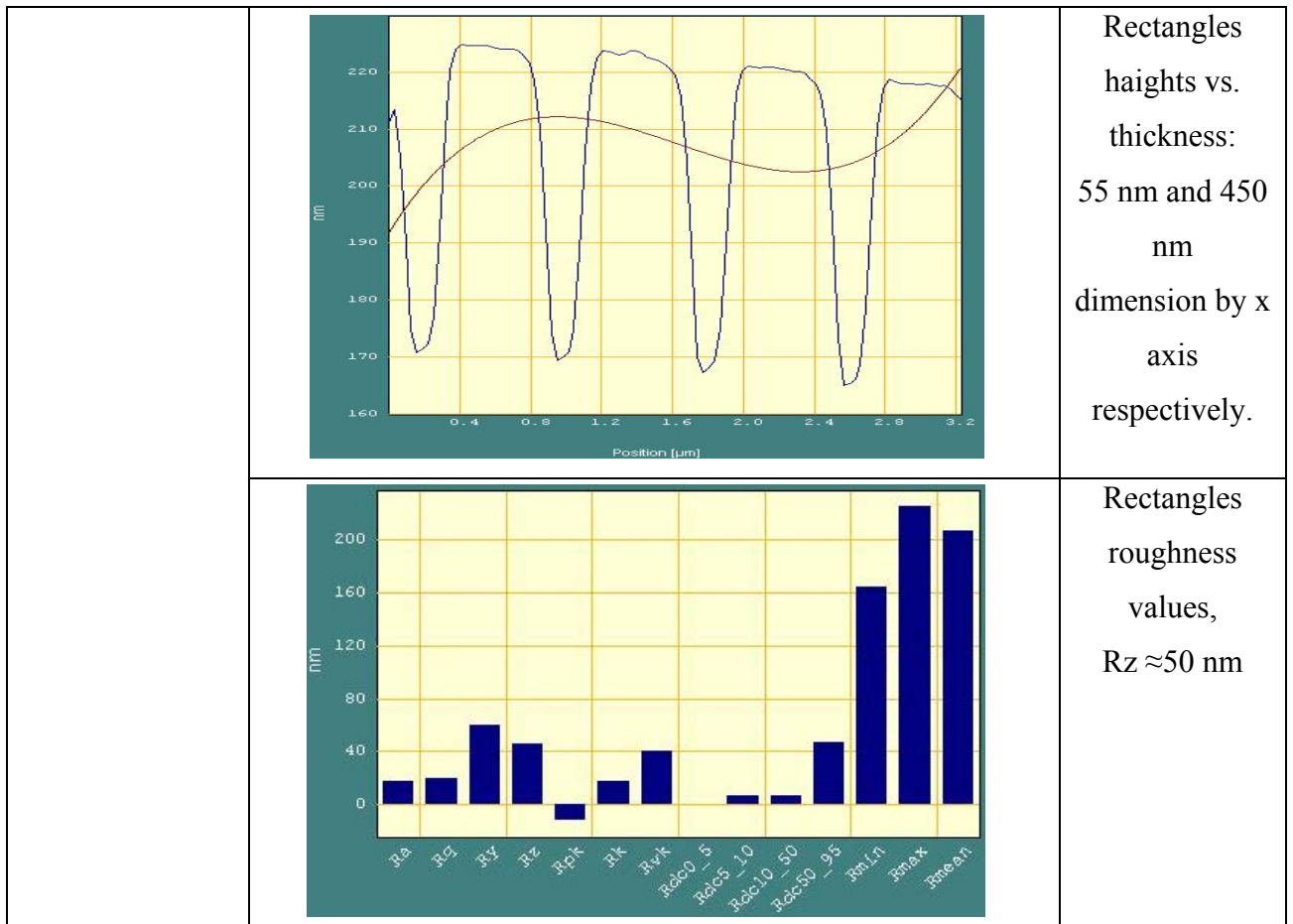


3D  
Topography  
image of  
squares  
4 x 4 μm



Squares  
heights vs.  
thickness:  
50 nm and 450  
nm dimension  
by x axis  
respectively

		<p>Squares roughness values,  <math>R_z \approx 50</math></p>
<p>450 x 900 nm rectangles, pitch distance 750 x 1030 nm by x and y axes respectively</p>		<p>2D      Topography image of rectangles      4 x 4 <math>\mu\text{m}</math></p>
		<p>3D      Topography image of rectangles      4 x 4 <math>\mu\text{m}</math></p>



Atomic Force Microscopy results show that geometries of fabricated nanostructures are not so precise. 3D Topography images represent number of surface irregularities along each nanotriangle, nanorectangle and nanosquare. However, results for  $R_z$  are 55 nm for both triangles and rectangles. Only squares show less  $R_z$  value of 50 nm. It could be deduced, that all shapes are matched the design dimensions and could be investigated optically.

### 3.5 Ellipsometry data of fabricated plasmonic substrates

Ellipsometry is highly sensitive, non destructive, advanced spectroscopic data acquisition technique (Fig. 3.2), based on relative phase change in a polarized light beam reflected on (or transmitted through) thin film surface of multiple or single wavelengths and angles of incident [34].

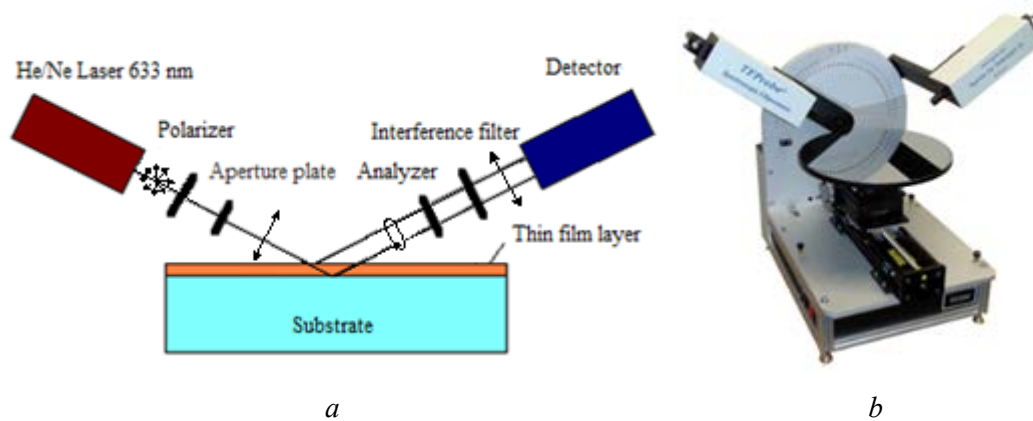


Figure 3.2 a) Light beam of 633 nm is polarized elliptically by the polarizer. After the aperture plate elliptically polarized monochromatic light hits the substrate at 70° angle, then reflects from it and enters the analyzer, which doesn't let any light pass through if the light is totally linearly polarized. Finally the reflected light is filtered to be sure that only 633 nm of wavelength is detecting [34]; b) TFprobe ellipsometer, model: SE200BM at Nanosyd was used for experiment [35]

Intensity of the light reflected from the substrate is detected by Detector and plotted as a curve (Fig. 3.3)

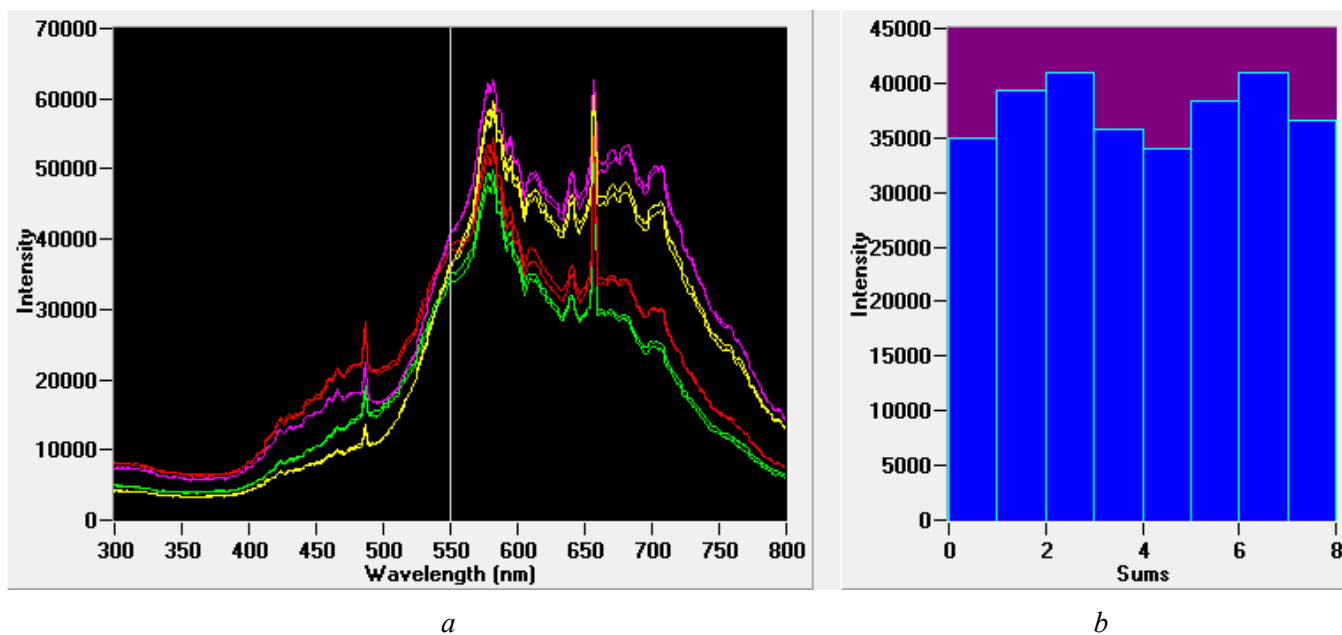


Figure 3.3 a) Intensity of incident light of polarizer on gold plasmonic substrate. b) Maximum intensity of reflected light acquisition by tilting the substrate. If the substrate tilted at the correct angle of reflection, the reflected beam enters the analyzer module along its optical axis [34].

Ellipsometer is accompanied by the operating software, which digitizes optical data coming from the substrate (Fig. 3.4) thus, enabling to estimate unknown optical parameters of interest.

Reflection spectra of 70 nm gold thin film at different incident angles of 400 nm and 790 nm S and P polarized light (Fig. 3.7).

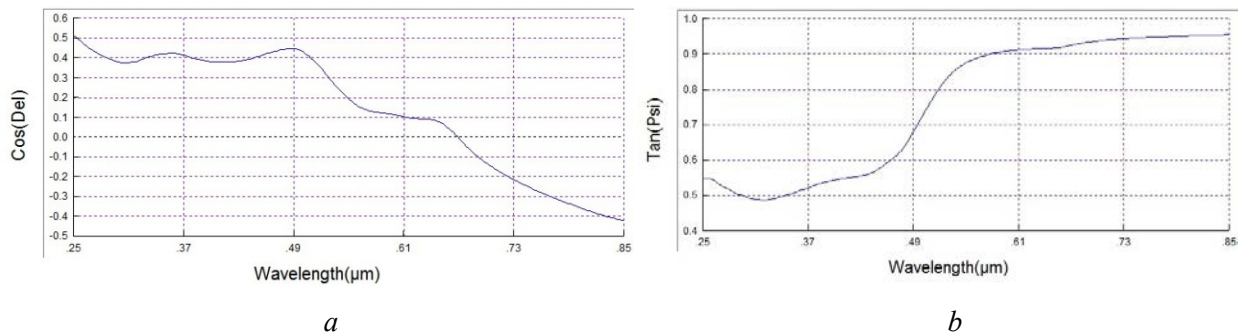


Figure 3.4 If polarized light is reflected from the surface it causes the phase shift of its perpendicular as well as parallel components; thus, ellipsometric parameters a) Delta-phase shift dependence on wavelength; b) Psi-amplitude ratio dependence on wavelength.

The real and imaginary parts of refractive index of the substrate material can be estimated from the data of ellipsometric parameters. Figure 3.5 represents n and k components of refractive index of gold.

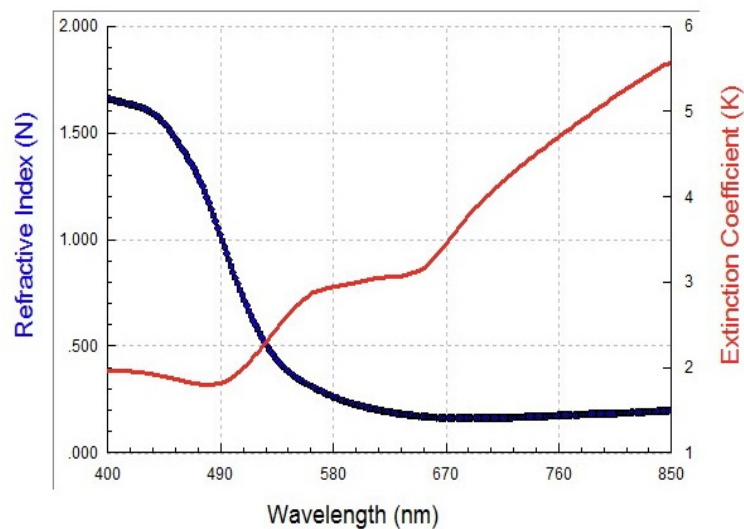


Figure 3.5 Real and imaginary parts of refractive index of gold at Visible and IR diapason;

Calculated reflectance percentage spectra of 55 nm gold thin films are represented as follows (Fig. 3.6):

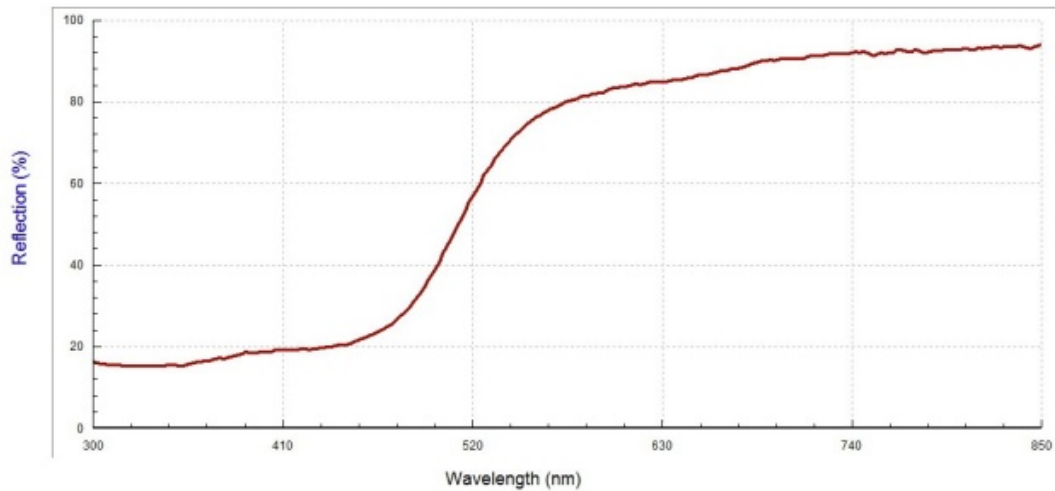


Figure 3.6 Percentage reflectance of gold thin films of 55 nm thickness.

### 3.6 Second-Harmonic spectra and imaging of plasmonic substrates

Second-Harmonic Generation (or frequency doubling) is nonlinear optical effect, which is observed on fabricated plasmonic substrates by excitation of femtosecond laser pulses (Fig. 3.8). When incident femtosecond pulsing laser beam  $\lambda = 790$  nm, duration less than 100 fs (Table 2.2), of 50 mW to several hundreds of mW hits gold substrate it enables of simultaneous two-photon absorption and second-harmonic generation phenomena (section 1.4.1)

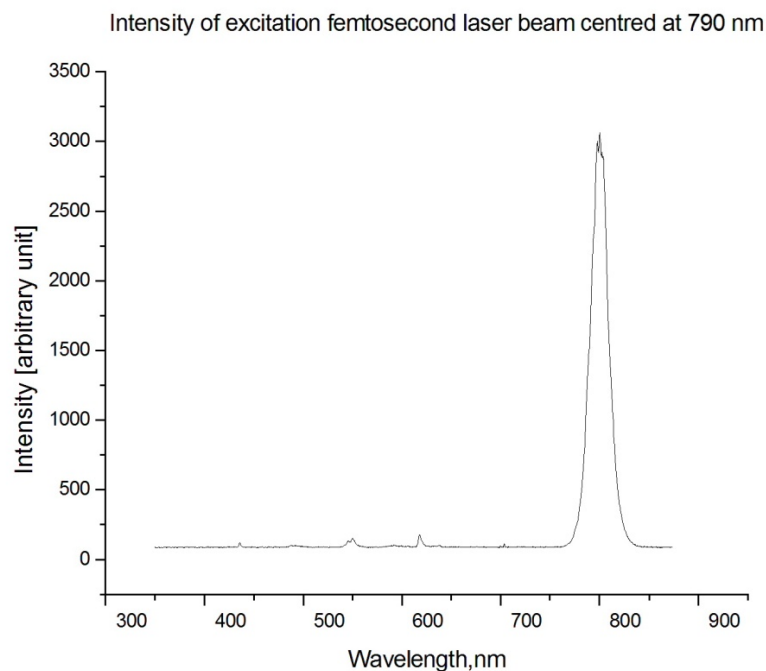
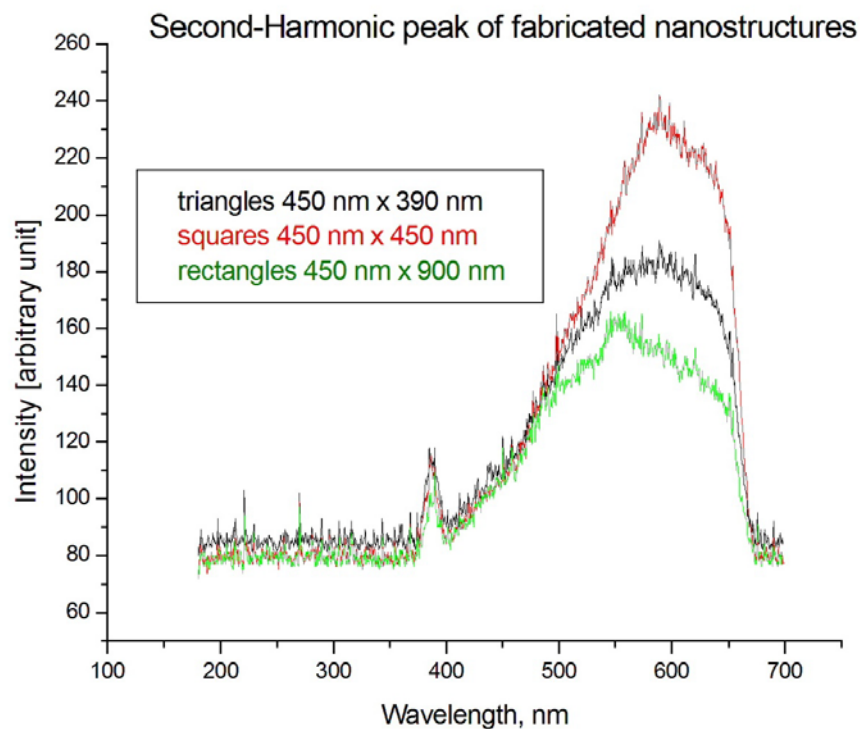


Figure 3.7 Incident Gaussian shape laser beam Intensity estimated by Avantes spectrometer after it passes the  $\lambda/2$  plate.

When two photons of Infrared diapason at 790 nm enters the material of Au plasmonic substrate, the one photon is being emitted with exactly the double frequency and half the excitation wavelength 395 nm at Visible diapason (Fig. 3.8).

The substrates emit light by itself when SHG happens (Fig. 3.9). The many molecules of the substrate can be observed at the same time, however it is high background signal, which was estimated and compensated by Avantes spectrometer in order to get accurate measurements. Two-photon excitation generates high photon densities in a certain sections of the sample stimulating transition of molecules between energy states. Because two-photon excitation depends on simultaneous absorption, the resulting fluorescence emission (Fig. 3.9) varies with the square of the excitation intensity [37]. Since the energy of a photon is inversely proportional to its wavelength, the two absorbed photons must have wavelength which is about twice less that required for one-photon excitation [37] (Fig. 3.8).



*Figure 3.8 demonstration of SHG peak at 395 nm of visible diapason of EM spectra for arrays of triangles, squares and rectangles with 750 x 750 nm (triangles, squares) and 750 x 1030 nm (rectangles) of period.*

During second-harmonic spectra measurements, normal incidence with controlled linear polarization vector was defined by  $0^\circ$  at the substrate surface. Second-harmonic signal from gold substrate without nanostructures was not caught due to its evident weakness.

Owing to the small focus volume and high peak intensity of LSM fluorescence emission images of plasmonic nanostructured substrates are observed. Excited electromagnetic radiation emitted by the sample (Fig. 2.12) is being focused by the lens to the Photomultiplier, which counts photons and emits photocurrent, which is then passed through the certain LSM setup optical components (pre-amplifier, discriminator) and finally appeared on the computer. “Globals for Imaging” arranges the collected photocurrent signal into an image of the scanned area [27] (Fig. 3.9).

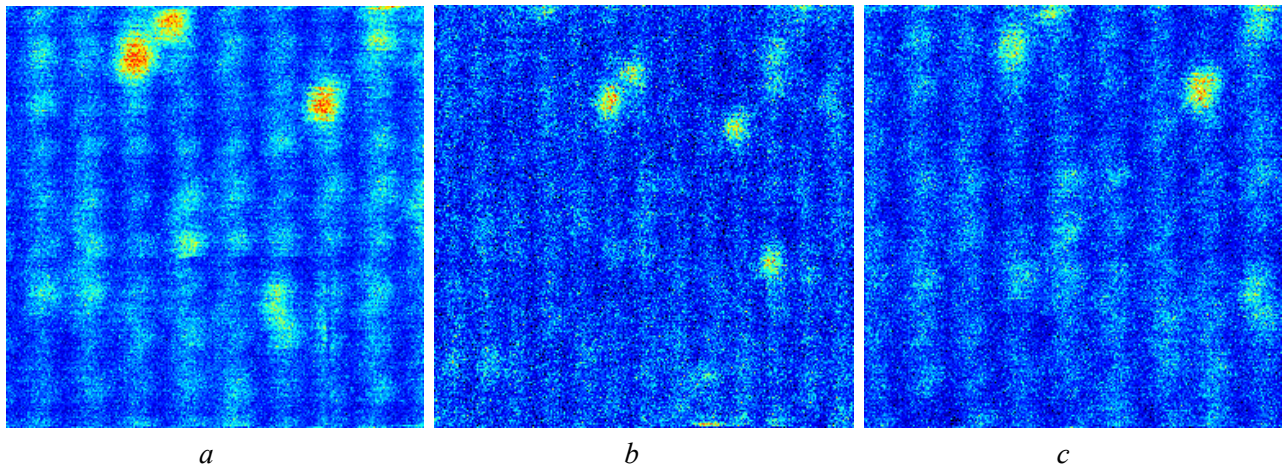


Figure 3.9 LSM imaging of fluorescence emission of plasmonic substrates: a) 200mV (8.9 x 8.9  $\mu\text{m}$  [27]) scanning area of triangles; b) 300 mV (10.25 x 10.25  $\mu\text{m}$ ) scanning area of rectangles and c) 200 mV (8.9 x 8.9  $\mu\text{m}$  [27]) scanning area of squares.

Figures 3.9 represent poor resolution due to the fact of resolution limit about  $450/2$  nm. Blue bandpass filter (450 nm) was used during LSM and SHG experiments in order to catch the only important signal of observed field enhancements of nanostructures, and cut another unimportant wavelength above 450 nm.

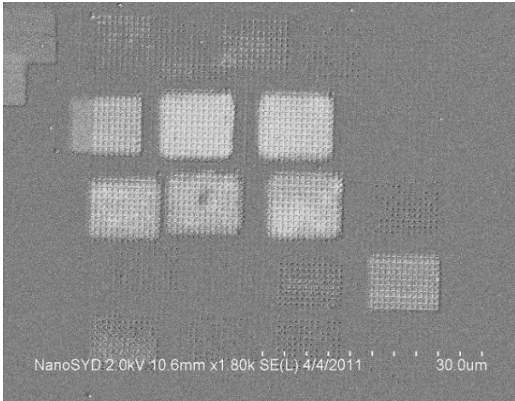
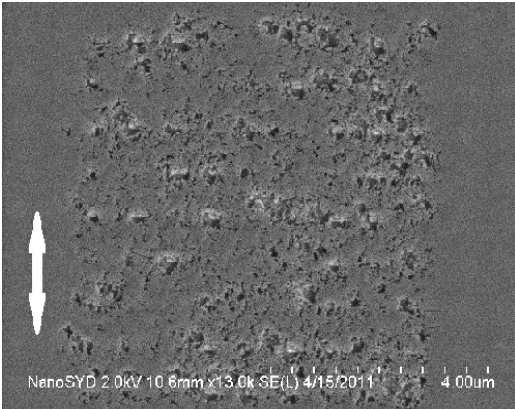
### 3.7 Scanning Electron Microscopy images of ablated substrates

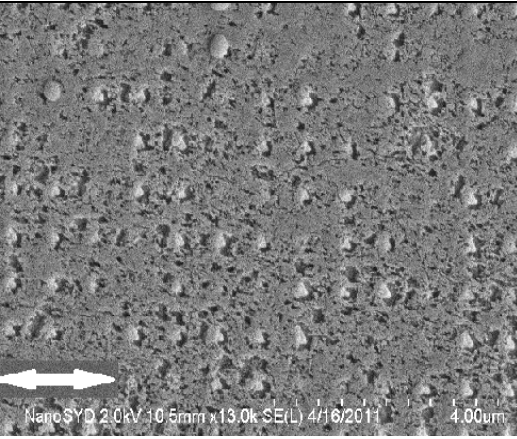
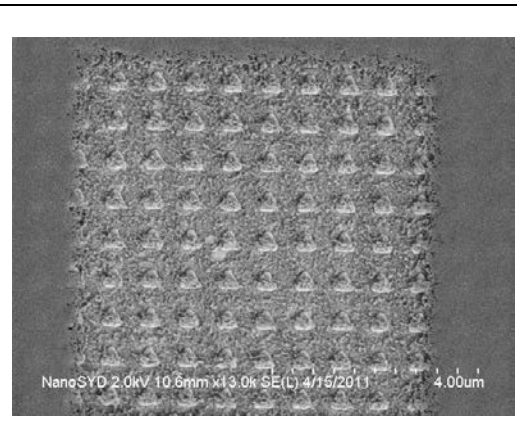
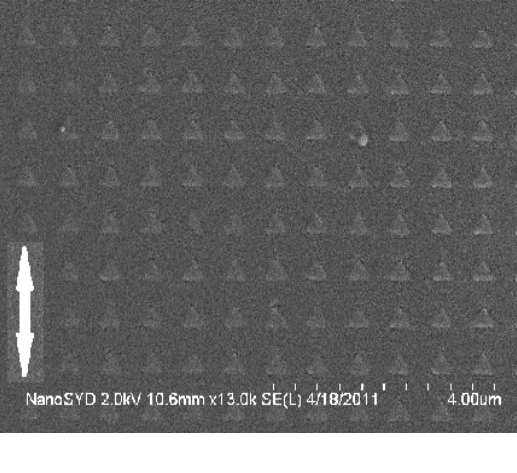
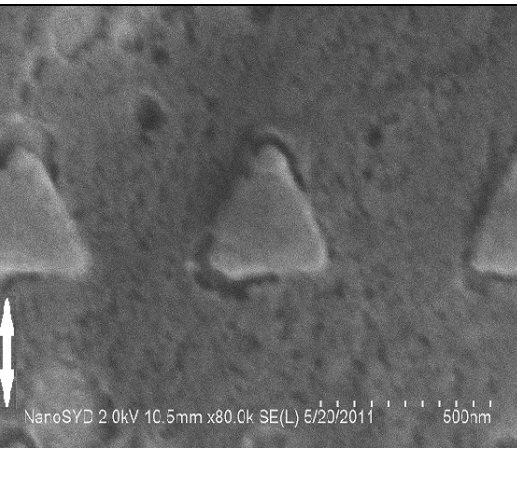
Field enhancements mapping of the gold substrates are represented in table 3.5. Ablation was performed using Ti:Sapphire laser (<100 fs pulses, repetition rate 80 MHz and max pulse energy 8nJ) beam of wavelength centered at 790 nm with different fluence variations (controlled by  $\lambda/2$  plate). One full area scan time was roughly estimated, so during one full scan each diffraction limited spot receive one laser pulse. The ablation threshold for PMMA in my case was roughly theoretically calculated (section 2.8) and equal to  $F_{\text{th}} \approx 0.24 \text{ J/cm}^2$ . It was not precisely estimated, due to many factors influence on this value, for instance, how long had the PMMA layer been in the

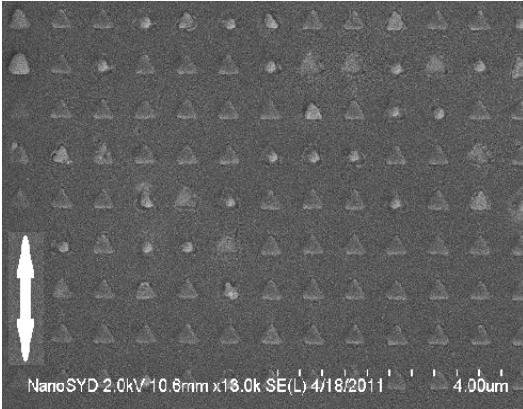
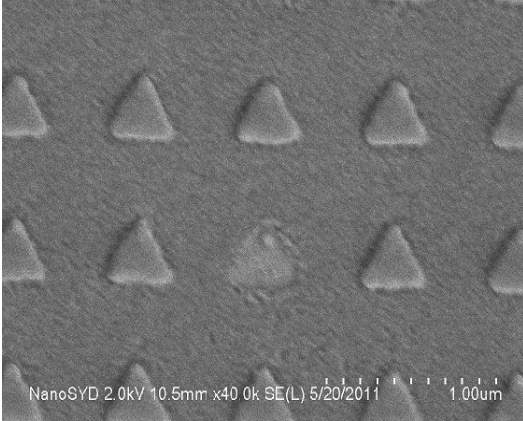
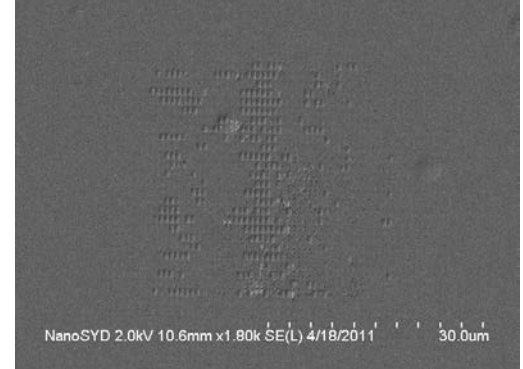
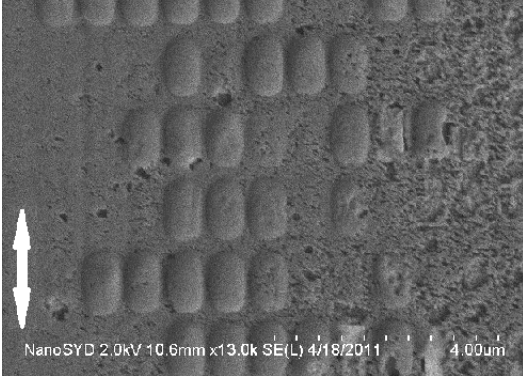
coated condition on the substrate at the moment of ablation, thickness of PMMA layer, laser pulse duration and stability, surroundings temperature, humidity and etc. All ablation experiments were performed at normal incidence with controlled linear polarization. Substrates were rotated by 0° or 90° with respect to the vector of incident light, thus, enabling different polarization vectors at the substrate surface during ablation. White arrows indicate the polarization direction [29].

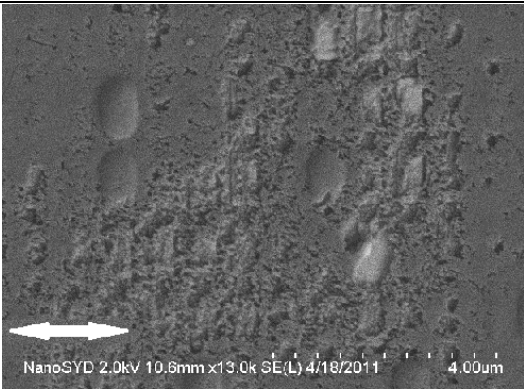
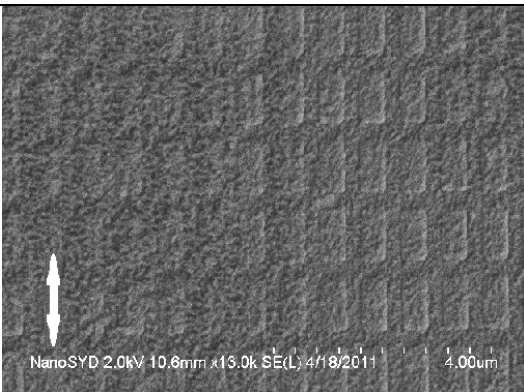
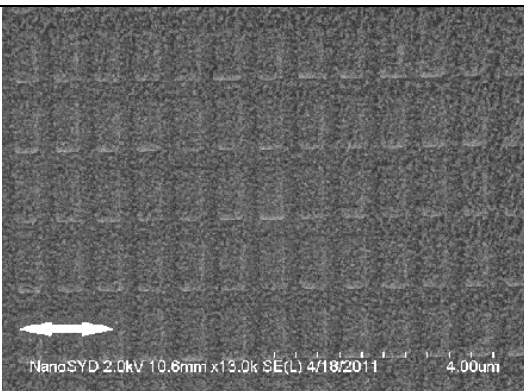
Table 3.5

Scanning Electron Microscopy images representing field enhancements of gold plasmonic substrates

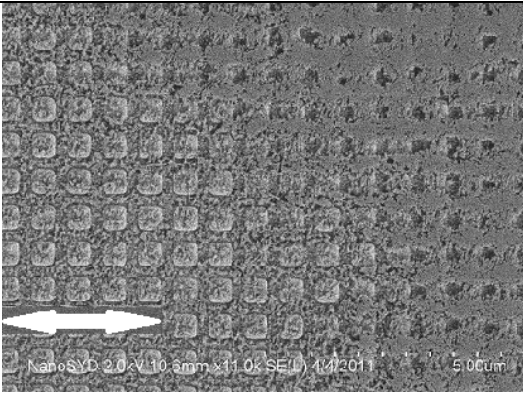
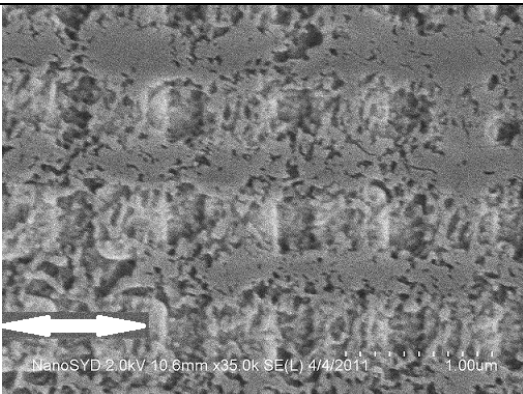
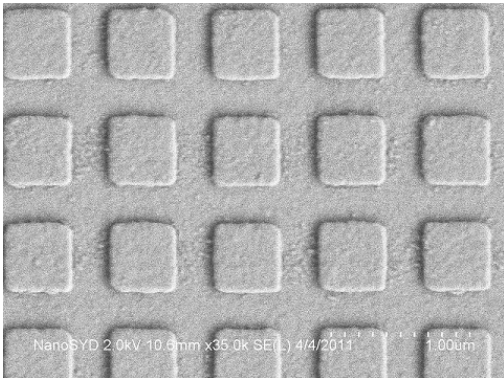
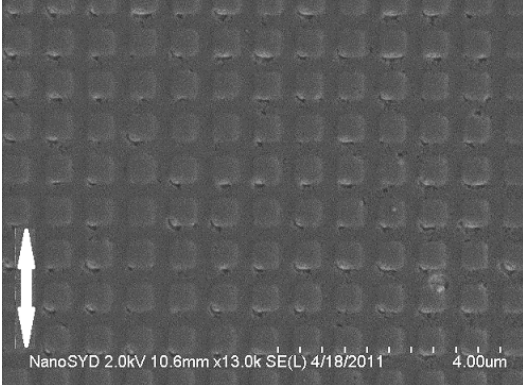
Nr.	Sample	Image	Description
1	PMMA 200 nm Image of ablated one single platform with nanostructures		Ablated PMMA layer on gold plasmonic substrate. Different grey color intensities represent variations of applied laser beam fluences, focus of ablation adjustment and ablation time. The brighter it seems, the higher values were applied. Magnification x1.80k
2	450 x 450 nm triangles, pitch distance 750 x 750 nm by x and y axes respectively; PMMA 200 nm		790 nm $F=0.22 \text{ J/cm}^2$ scanning for <b>4 seconds</b> ; <b>300 mV</b> scanning area (about 10 x 10 $\mu\text{m}$ ); sampling frequency 40000; About 2 full scan; Magnification x13.0k

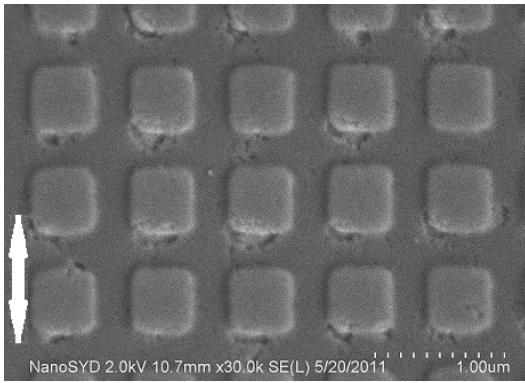
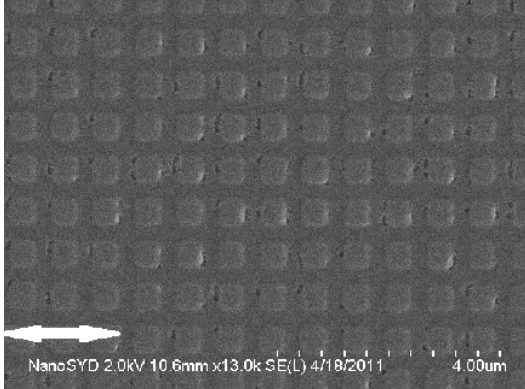
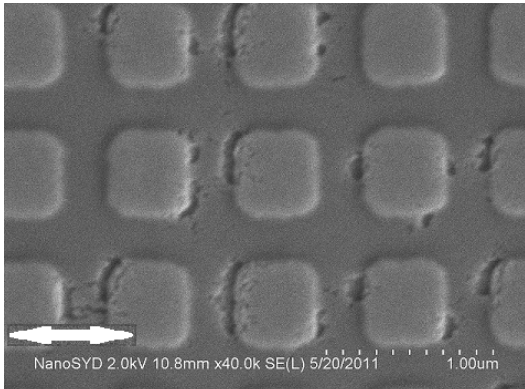
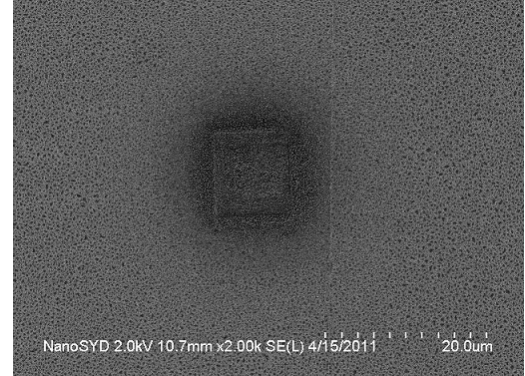
3	450 x 450 nm triangles, pitch distance 750 x 750 nm by x and y axes respectively; PMMA 200 nm		790 nm $F=0.24 \text{ J/cm}^2$ scanning for <b>4 seconds</b> ; <b>300 mV</b> scanning area (about 10 x 10 $\mu\text{m}$ ); sampling frequency 40000; About 2 full scans; Magnification x13.0k
4	450 x 450 nm triangles, pitch distance 750 x 750 nm by x and y axes respectively; PMMA 200 nm		790 nm $F=0.51 \text{ J/cm}^2$ scanning for <b>6 seconds</b> ; <b>300 mV</b> scanning area (about 10 x 10 $\mu\text{m}$ ); sampling frequency 40000; About 3 full scans; Magnification x13.0k
5	450 x 450 nm triangles, pitch distance 750 x 750 nm by x and y axes respectively; PMMA 80 nm		790 nm $F=0.24 \text{ J/cm}^2$ scanning for <b>4 seconds</b> ; <b>300 mV</b> scanning area (about 10 x 10 $\mu\text{m}$ ); sampling frequency 40000; About 2 full scans; Magnification x13.0k
6	450 x 450 nm triangles, pitch distance 750 x 750 nm by x and y axes respectively; PMMA 80 nm		790 nm $F=0.24 \text{ J/cm}^2$ scanning for <b>4 seconds</b> ; <b>300 mV</b> scanning area (about 10 x 10 $\mu\text{m}$ ); sampling frequency 40000; About 2 full scans; Magnification x80.0k of image Nr. 5

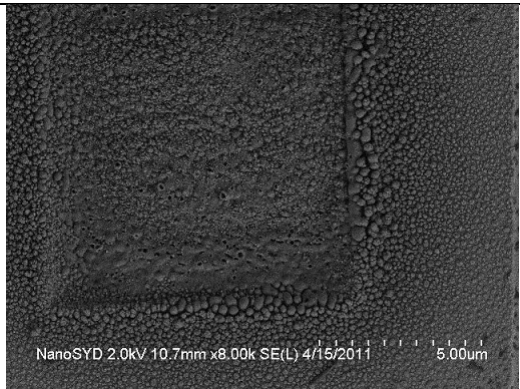
7	450 x 450 nm triangles, pitch distance 750 x 750 nm by x and y axes respectively; PMMA 80 nm		790 nm $F=0.51 \text{ J/cm}^2$ scanning for <b>6 seconds</b> ; <b>300 mV</b> scanning area (about 10 x 10 $\mu\text{m}$ ); sampling frequency 40000; About 3 full scans; fully ablated Magnification x13.0k
8	450 x 450 nm triangles, pitch distance 750 x 750 nm by x and y axes respectively; PMMA 80 nm		790 nm $F=0.51 \text{ J/cm}^2$ scanning for <b>6 seconds</b> ; <b>300 mV</b> scanning area (about 10 x 10 $\mu\text{m}$ ); sampling frequency 40000; About 3 full scans; fully ablated Magnification x40.0k
9	450 x 900 nm rectangles, pitch distance 750 x 1030 nm by x and y axes respectively; PMMA 200 nm		790 nm $F=0.22 \text{ J/cm}^2$ scanning for <b>4 seconds</b> ; <b>1000 mV</b> scanning area (about 30 x 30 $\mu\text{m}$ ); sampling frequency 40000; About 1 full scan; Magnification x1.80k
10	450 x 900 nm rectangles, pitch distance 750 x 1030 nm by x and y axes respectively; PMMA 200 nm		790 nm $F=0.22 \text{ J/cm}^2$ scanning for <b>4 seconds</b> ; <b>1000 mV</b> scanning area (about 30 x 30 $\mu\text{m}$ ); sampling frequency 40000; About 1 full scan; Magnification x13.0k

11	450 x 900 nm rectangles, pitch distance 750 x 1030 nm by x and y axes respectively; PMMA 200 nm		790 nm $F=0.23 \text{ J/cm}^2$ scanning for <b>8 seconds</b> ; <b>300 mV</b> scanning area (about 10 x 10 $\mu\text{m}$ ); sampling frequency 40000; About 4 full scans; Magnification x13.0k
12	450 x 900 nm rectangles, pitch distance 750 x 1030 nm by x and y axes respectively; PMMA 200 nm		790 nm $F=0.29 \text{ J/cm}^2$ scanning for <b>8 seconds</b> ; <b>300 mV</b> scanning area (about 10 x 10 $\mu\text{m}$ ); sampling frequency 40000; About 4 full scans; Magnification x13.0k
13	450 x 900 nm rectangles, pitch distance 750 x 1030 nm by x and y axes respectively; PMMA 200 nm		790 nm $F=0.51 \text{ J/cm}^2$ scanning for <b>8 seconds</b> ; <b>300 mV</b> scanning area (about 10 x 10 $\mu\text{m}$ ); sampling frequency 40000; About 4 full scans; Magnification x13.0k
14	450 x 900 nm rectangles, pitch distance 750 x 1030 nm by x and y axes respectively; PMMA 200 nm		790 nm $F=0.51 \text{ J/cm}^2$ scanning for <b>8 seconds</b> ; <b>300 mV</b> scanning area (about 10 x 10 $\mu\text{m}$ ); sampling frequency 40000; About 4 full scans; Magnification x13.0k



19	450 x 450 nm squares, pitch distance 750 x 750 nm by x and y axes respectively; PMMA 200 nm		790 nm $F=0.34 \text{ J/cm}^2$ scanning for <b>4 seconds</b> ; <b>500 mV</b> scanning area (19.2 x 19.2 $\mu\text{m}$ ); sampling frequency 40000; About 2 full scans; Magnification x11.0k
20	450 x 450 nm squares, pitch distance 750 x 750 nm by x and y axes respectively; PMMA 200 nm		790 nm $F=0.34 \text{ J/cm}^2$ scanning for <b>4 seconds</b> ; <b>500 mV</b> scanning area (19.2 x 19.2 $\mu\text{m}$ ); sampling frequency 40000; About 2 full scans; Magnification x35.0k
21	450 x 450 nm squares, pitch distance 750 x 750 nm by x and y axes respectively; PMMA 200 nm fully ablated		790 nm $F=0.53 \text{ J/cm}^2$ scanning for 6 seconds; <b>300 mV</b> scanning area (about 10 x 10 $\mu\text{m}$ ); sampling frequency 40000; About 3 full scans; Magnification x35.0k
22	450 x 450 nm squares, pitch distance 750 x 750 nm by x and y axes respectively; PMMA 80 nm		790 nm $F=0.24 \text{ J/cm}^2$ scanning for 6 seconds; <b>300 mV</b> scanning area (about 10 x 10 $\mu\text{m}$ ); sampling frequency 40000; About 3 full scans; Magnification x13.0k

23	450 x 450 nm squares, pitch distance 750 x 750 nm by x and y axes respectively; PMMA 80 nm		790 nm $F=0.24 \text{ J/cm}^2$ scanning for 6 seconds; <b>300 mV</b> scanning area (about 10 x 10 $\mu\text{m}$ ); sampling frequency 40000; About 3 full scans; Magnification x30.0k
24	450 x 450 nm squares, pitch distance 750 x 750 nm by x and y axes respectively; PMMA 80 nm		790 nm $F=0.24 \text{ J/cm}^2$ scanning for 6 seconds; <b>300 mV</b> scanning area (about 10 x 10 $\mu\text{m}$ ); sampling frequency 40000; About 3 full scans; Magnification x13.0k
25	450 x 450 nm squares, pitch distance 750 x 750 nm by x and y axes respectively; PMMA 80 nm		790 nm $F=0.24 \text{ J/cm}^2$ scanning for 6 seconds; <b>300 mV</b> scanning area (about 10 x 10 $\mu\text{m}$ ); sampling frequency 40000; About 3 full scans; Magnification x40.0k of image 21
26	450 x 450 nm squares, pitch distance 750 x 750 nm by x and y axes respectively;		$F=0.61 \text{ J/cm}^2$ After about 2 minutes of scanning burned off squares. Magnification x2.00k

27	450 x 450 nm squares, pitch distance 750 x 750 nm by x and y axes respectively;		<p><b>F=0.61 J/cm<sup>2</sup></b></p> <p>After about 2 minutes of scanning burned off squares.</p> <p>Magnification x8.00k</p>
----	---	--	--

It has been roughly estimated observing the scanning laser spot moving on the screen and using stopwatch that the full scan of 500, 200 and 300 mV with 40000 of sampling frequency is accomplished after 2 seconds. For 1000 mV it is about 4 seconds for 1 scan.

Summarizing all results (Table 3.6):

Table 3.6

Ablated fluence vs. topography changes

<b>Geometry</b>	<b>Fluence, J/cm<sup>2</sup></b>	<b>A2 950 PMMA, 80 nm</b>	<b>A4 950 PMMA, 200 nm</b>
Triangles 450 x 450 nm; pitch distance 750 x 750 nm respectively by x-y	0.22		Modifications become visible after about 2 scans
	0.24	Modifications become visible after about 2 scans	Significant modifications appear after about 2 scans
	0.51	After 3 scans triangle is removed or change its geometry, becoming a circle	PMMA is fully removed after about 3 scans. Geometries do not change
Rectangles 450 x 900 nm; pitch distance 750 x 1030 nm respectively by x-y	0.22		Modifications become visible after about 1 scan
	0.23		Significant modifications appear after about 4 scans
	0.29		Very significant modifications appear after about 4 scans
	0.51		Allmost all PMMA is

			removed after about 4 scans
Squares 450 x 450 nm; pitch distance 750 x 750 nm respectively by x-y	0.2		Modifications become visible after about 1 scan
	0.24	Modifications become visible after about 3 scans	Significant modifications appear after about 1 scans
	0.34		Very significant modifications appear after about 2 scans
	0.53		PMMA is fully removed after about 3 scans

Some assumptions and discourse:

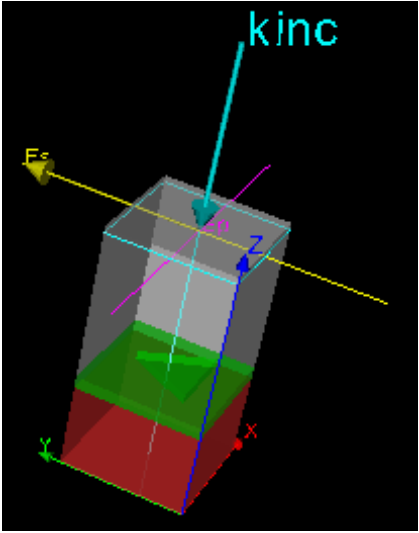
- PMMA is not 100% transparent material (Appendix 2) at 790 nm as well as visible spectra, where SH is generated, therefore it could be assumed that thicker 200 nm layer of PMMA is ablated faster, than 80 nm and it needs lower fluences of laser pulsing beam due to some small amounts of absorption happen inside;
- At larger ablation areas gradient of ablation is spreading diagonally (Table 3.5, image 19);
- Triangles generate higher amounts of Near-Field Intensities, because for full PMMA ablation it requires fluence about  $0.51 \text{ J/cm}^2$  for about 3 scans (Table 3.5, image 4), while for squares fluence is about  $0.53 \text{ J/cm}^2$  for about 3 scans (Table 3.5, image 21), and for rectangles it is about  $0.51 \text{ J/cm}^2$  for about 4 scans (Table 3.5, images 12, 13). However if polarization changes by  $90^\circ$  (y axis), where dimension of rectangles is 900 nm, longer scanning is needed in order to full remove of PMMA;
- After ablation of rectangles, some convex reliefs appear under each single rectangle (Table 3.5, images 10, 11). It seems like PMMA layer is coming off the plasmonic substrate affected by Near-Field Intensities generated at nanostructures. A possible explanation for this phenomena is that an overheated liquid is generated, which vaporizes instantaneously [40];
- After ablation at high enough fluence about  $0.51 \text{ J/cm}^2$  and long time scanning, the gold triangles become molten [41] (Table 3.5, image 7) or even fully disappear (Table 3.5, image 8);
- It has been noticed that the sharper edges are, the higher Near-Field Intensities are generated at the top of the edges (Table 3.5, image 6, 23, 25; Table 3.7).

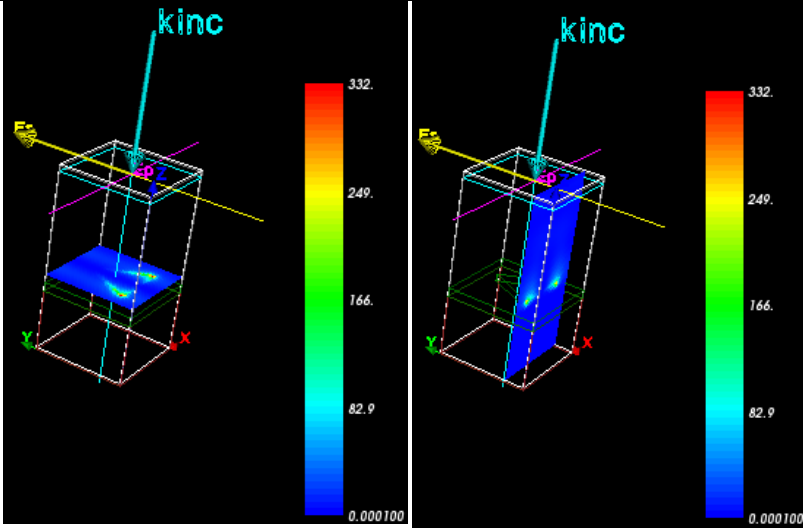
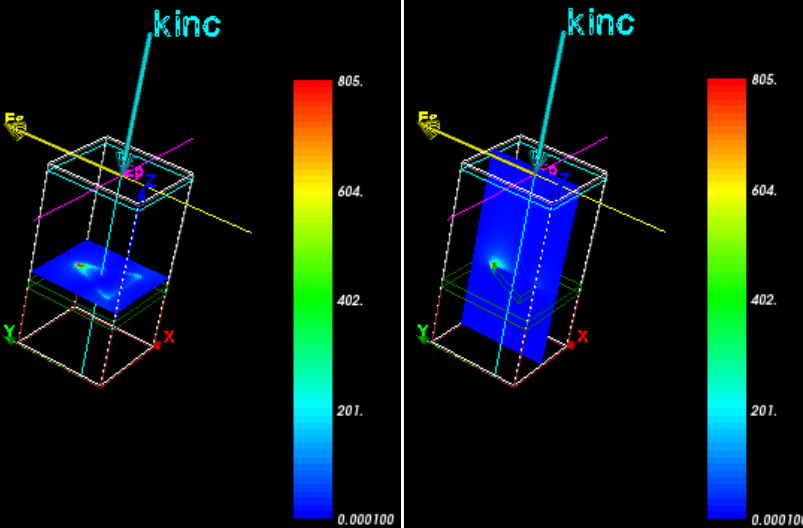
### 3.8 Software-based Near-Field Intensities simulation of plasmonic substrates.

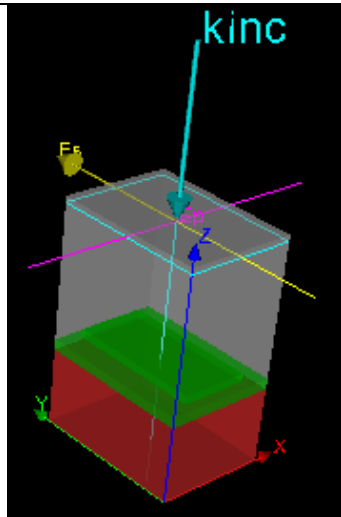
There are various types of commercial software, which can be implemented for theoretically observation of how electromagnetic radiation interacts with material. EM Explorer was used for this purpose. Solutions are based on FDTD (Finite Difference Time Domain) method of Maxwell's equation (section 1.1) approximation. Software has its benefits and drawbacks. The advantages include simple & robust numerical algorithm (Appendix 4), versatility for nearly any geometries, and good scalability of computing resources as a function of simulation volume size [36]. The disadvantages are numerical dispersion and stability constraint due to the finite difference (FD) approximation to Maxwell's equations and explicit time marching algorithm [36]. Table 3.7 represents obtained results of electromagnetic radiation propagation over plasmonic substrates with one single nanostructure of different shapes: triangles, rectangles and squares of predefined dimensions.

Table 3.7

Near-Field Intensities demonstration based on EM Explorer Simulation Results

Image	Description
 <p>450 x 450 nm triangles, pitch distance 750 x 750 nm by x and y axes respectively;</p>	<p>Starting geometry design with <math>k_{inc}</math>-incident 790 nm light; <math>E_s</math> yellow arrow – s polarization (x); <math>E_p</math> pink arrow – p polarization (y);</p> <p>Red - Si substrate with refractive indexes:  <math>n</math> 3.74951;  <math>k</math> 0.018917;</p> <p>Green – Au 70 nm thin film and 55nm triangle with refractive index values:  <math>n</math> 0.15045;  <math>k</math> 4.82455;</p> <p>Grey – Air with refractive index values:</p>

	<p>n 1.0; k 0;</p> <p>Near-Field Intensity Slices (X-polarized incident field)</p>
	<p>Near-Field Intensity Slices (Y-polarized incident field)</p>
	<p>Starting geometry design with <math>k_{inc}</math>-incident 790 nm light; <math>E_s</math> yellow arrow – s polarization (x); <math>E_p</math> pink arrow – p polarization (y);</p> <p>Red - Si substrate with refractive indexes:  n 3.74951;  k 0.018917;</p> <p>Green – Au 70 nm thin film and 55nm rectangle with</p>



450 x 900 nm rectangles, pitch distance 750 x 1030 nm by x and y axes respectively;

refractive index values:

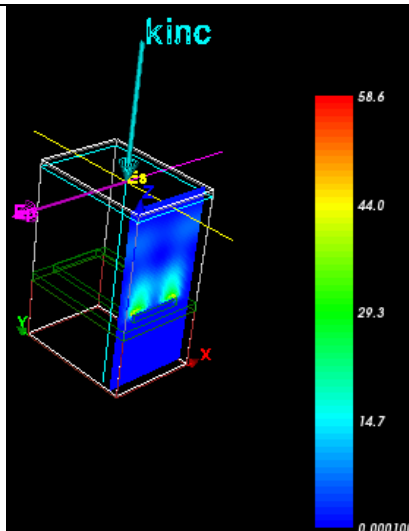
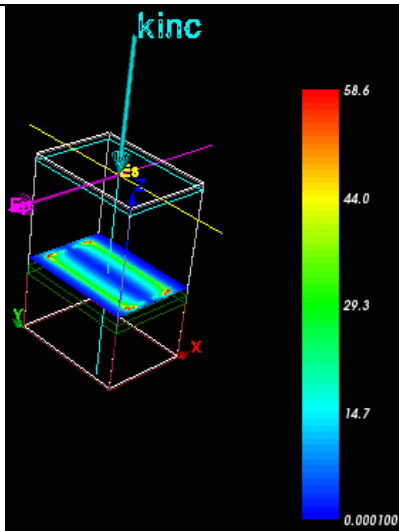
n 0.15045;

k 4.82455;

Grey – Air with refractive index values:

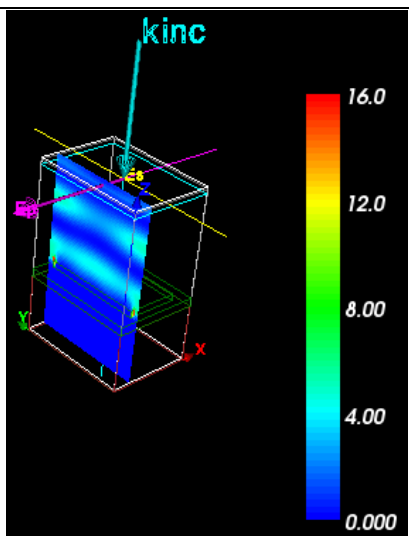
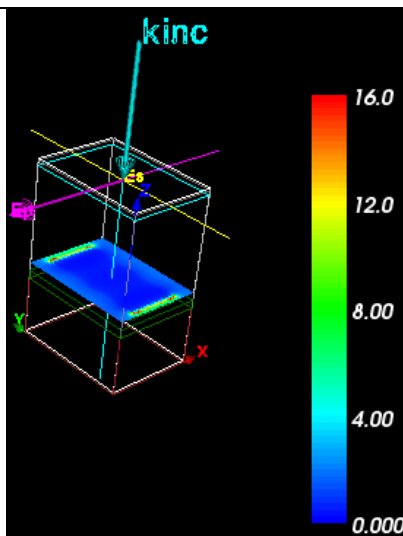
n 1.0;

k 0;



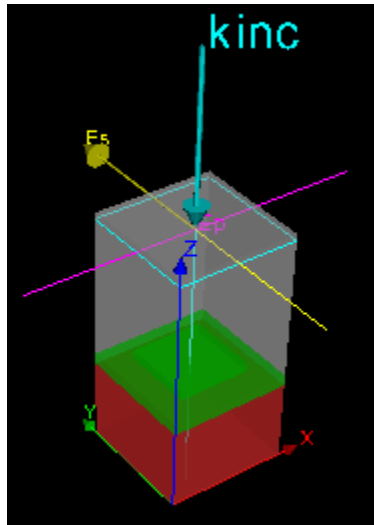
Near-Field Intensity Slices

(X-polarized incident field)



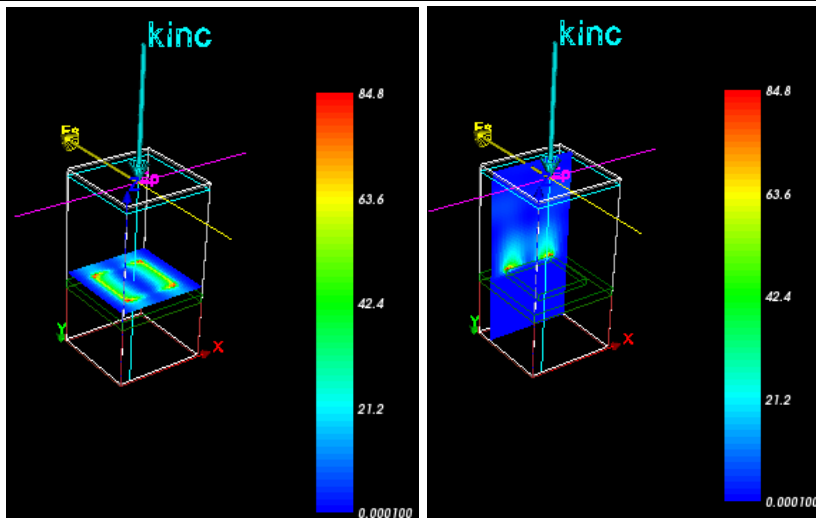
Near-Field Intensity Slices

(Y-polarized incident field)

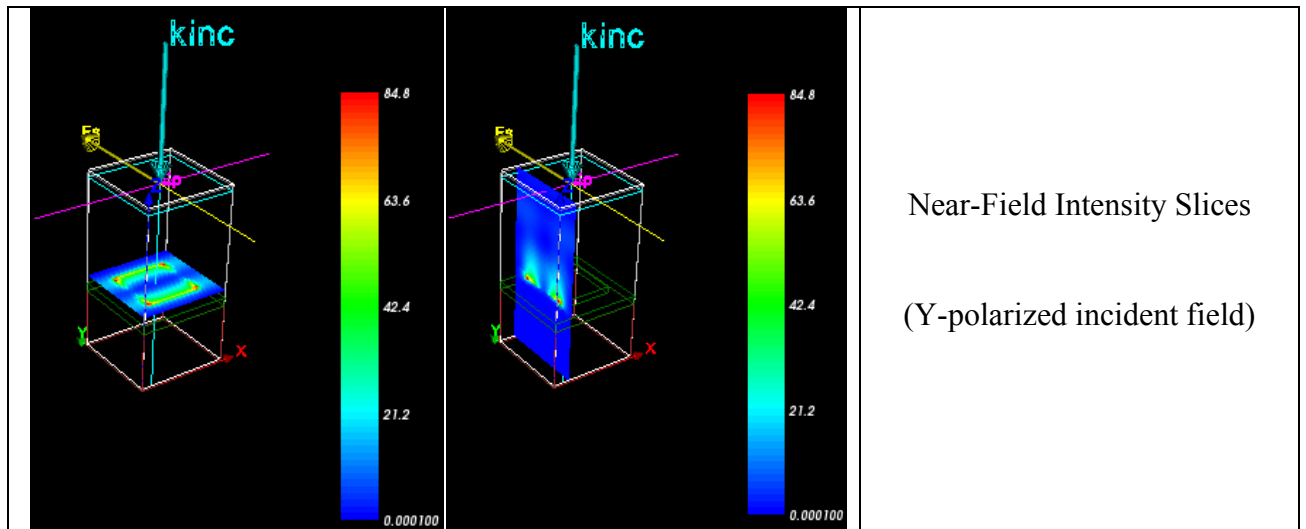


450 x 450 nm triangles, pitch distance 750 x 750 nm by x and y axes respectively;

Starting geometry design with  $k_{inc}$ -incident 790 nm light;  $E_s$  yellow arrow – s polarization (x);  $E_p$  pink arrow – p polarization (y);  
 Red - Si substrate with refractive indexes:  
 $n$  3.74951;  
 $k$  0.018917;  
 Green – Au 70 nm thin film and 55nm square with refractive index values:  
 $n$  0.15045;  
 $k$  4.82455;  
 Grey – Air with refractive index values:  
 $n$  1.0;  
 $k$  0;



Near-Field Intensity Slices  
 (X-polarized incident field)



Solutions were performed for 100 number of cycles for each s and p polarizations.

Images of simulation were saved at different number of solution cycles. Therefore, so different Near-Field Intensities for triangles, squares and rectangles are represented. However it has been mentioned, that rectangles represent less Near-Field Intensities at all solution cycles for Y-polarized incident field. It can be explained by large dimension at y-axis equal to 900 nm, which is larger than incident field wavelength equal to 790 nm.

For all geometries EM Explorer software solutions represents the same near-field enhancement locations as it was noticed during PMMA ablation (Table 3.5 N r. 6, 12, 23, 25). Consequently, in the issue of plasmon migrations intensive localized maximum on the tops or sharp edges of triangles, rectangles and squares is represented. It becomes possible to concentrate energy in nanometer scale due to localized surface plasmon resonances appearance when light interacts with particles much smaller than the incident wavelength.

These simulations represent electromagnetic energy on plasmonic substrates concentration for only one single triangle, rectangle and square, however, in the case of periodically distributed arrays of the same geometries, near field intensities of each triangle, rectangle and square would amplify the near-field intensity of the neighbor one.

#### 4. DISCUSSIONS AND FUTURE PLANS

This work helps me to become familiar with fabrication of plasmonic substrates and nondestructive investigation of nonlinear optical behaviour of them. Furthermore, understanding of quite complicated linear polarized light propagation at nanoscale within different geometries becomes stronger while analyzing results of experimental part. During this work, I became even more interested in nano-optics and I am looking forward to continue my development skills toward sensitive plasmonic substrates fabrication and analysis.

This work displays unique abilities of Au substrates to generate second harmonics and Near-Field Enhancements at the incident wavelength twice larger, than geometries of them. Surely, it is not only some interesting results, however it should be attractive for today microtechnology industry, due to the fact, that fabricated substrates generate intensive plasmon oscillation signal with ultrafast respond at femtosecond time scale.

Further investigations can be performed, if organic nanofibers would be placed between periodically distributed nanostructures. It would be another technique of plasmonic Near-Field Intensities observation. Fibers will work as waveguides for plasmon oscillations produced by nanostructures. Additionally, CNHP<sub>4</sub> gives the strongest SH signal of all organic fibers.

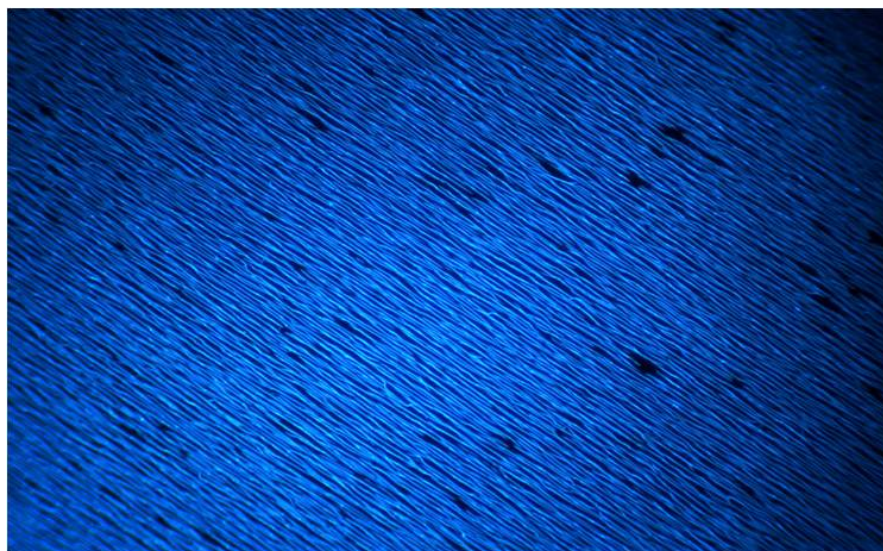


*Figure 4.1 Organic CNHP<sub>4</sub> Nanofibers fluorescence image performed using optical microscope with mercury lamp. Image area is 674x506  $\mu\text{m}$  by x20 objective (Appendix 5).*

Nonsymmetrical nanostructures of different shapes could be also fabricated in order to observe the other cases of Near-Field Enhancements.

## CONCLUSIONS

Fabrication and investigation of plasmonic substrates have been accomplished in this master thesis. Conclusions are represented by set of following remarks:

1. Using EBL arrays of triangles, rectangles and squares have been fabricated. The most suitable dose factors for each array with matrix of nanostructures have been estimated experimentally (Table 3.1).

2. Geometries of fabricated structures have been measured using SEM and AFM. Final fabricated dimensions differ from expected of about  $\leq 10$  nm (Table 3.3; 3.4).

3. The favourable film thicknesses of PMMA for further ablation have been found by varying rotation speed of spin-coating process and measuring then covered PMMA coatings implementing Profilometry technique. For A2 PMMA it is 80 nm and for A4 PMMA it is 200 nm (Table 2.1).

4. In order to investigate Near-Field Enhancements of fabricated gold plasmonic substrates, PMMA coatings have been ablated by ultrashort femtosecond laser Gaussian shape beam pulses. Ablation have been performed by controlled linearly polarized incident light changing either x or y polarization on the ablation surface. Threshold ablation fluence for PMMA has been calculated theoretically, taking into account that ablation happens from the bottom of the coated PMMA layer.  $F_{th}$  is equal to  $0.24 J/cm^2$  (section 2.8). Threshold fluence dependence on number of pulses has been plotted (Graph 2.1).

5. Second-Harmonic Generation signal has been observed by ablation of all three fabricated geometries and it is equal to the half of the incident wavelength. Incident IR light is 790 nm, Second-Harmonic Signal generated at 395 nm of visible diapason (Fig. 3.8)

6. LSM imaging of fluorescence emission of plasmonic substrates has been performed (Fig. 3.9).

7. Near-Field Enhancement Intensities of triangles, squares and rectangles have been demonstrated using commercial EM Explorer software based on Finite Difference Time Domain of Maxwell's Equations approximation method. Simulation images of Near-Field Intensities have been represented (Table 3.7). The experimentally observed near-field intensities locations (Table 3.5) coincide with the simulation results of near-field intensity locations (Table 3.7).

## REFERENCES

- [1] S.A. Maier, *Plasmonics: Fundamentals and Applications*, Springer, New York (2007).
- [2] K. A. Willets, R. P. Van Duyne, *Localized Surface Plasmon Resonance Spectroscopy and Sensing*, Ann. Rev. Phys. Chem. 58 267-97 (2007).
- [3] H. Raether, *Excitation of Plasmons and Interband Transitions by Electrons*, Springer Tracts in Modern Physics, v. 88, New York (1980).
- [4] Discover Nano, *Size Matters*, Northwestern University, (2005). //http//  
[www.discovernano.northwestern.edu/whatis/index\\_html/sizematters\\_html](http://www.discovernano.northwestern.edu/whatis/index_html/sizematters_html).
- [5] A. Goodacre, D. Donley, J. Jai, *Combining Second-Harmonic Generation with Multiphoton Imaging*, BioPhotonics October Features, Olympus America Inc. (2010). //http//  
[www.photonics.com/Article.aspx?AID=44684](http://www.photonics.com/Article.aspx?AID=44684).
- [6] C. Ropers, T. Elsaesser, G. Cerullo, M. Zavelani-Rossi, *Ultrafast optical excitations of metallic nanostructures: from light confinement to a novel electron source*, New J. Phys. 9, 397 (2007).
- [7] R. W. Boyd, *Nonlinear Optics*, 3<sup>rd</sup> edition, Academic Press, New York (2007).
- [8] Polyteknik Cryofox machines, *Explorer series*, House of coating technology. //http//  
[www.polyteknik.dk/Explorer\\_series.asp](http://www.polyteknik.dk/Explorer_series.asp).
- [9] Midwest tungsten service, Inc., tip, *Electron Beam Evaporation*. //http//  
[www.tungsten.com/tipsbeam.pdf](http://www.tungsten.com/tipsbeam.pdf).
- [10] M. Ohring, *The Material Science of Thin Film*, Academic Press (1992).
- [11] Paul Scherrer Institut, Materials Group, *Spin Coating*, Villigen. //http//  
[http://materials.web.psi.ch/Research/Thin\\_Films/Methods/Spin.htm](http://materials.web.psi.ch/Research/Thin_Films/Methods/Spin.htm).
- [12] Brewer Science, Inc., *Spin Coater Theory*. //http//

[www.brewerscience.com/research/processing-theory/spin-coater-theory](http://www.brewerscience.com/research/processing-theory/spin-coater-theory).

[13] SiliconFarEast online reference on semiconductor manufacturing, *Electron Beam Lithography*. (2004). //http// [www.siliconfareast.com/lith\\_electron.htm](http://www.siliconfareast.com/lith_electron.htm).

[14] H. J. Levinson, *Principles of Lithography*, 2<sup>nd</sup> edition, Spie, Washington (2005).

[15] Casino monte carlo simulation of electron trajectory in solids. //http//  
[www.gel.usherbrooke.ca/casino/index.html](http://www.gel.usherbrooke.ca/casino/index.html).

[16] Raith innovative solutions for nanofabrication and semiconductor navigation, *ELPHY Quantum*. //http//  
[www.raith.com/?xml=solutions|SEM+%26+FIB+lithography+kits|ELPHY+Quantum](http://www.raith.com/?xml=solutions|SEM+%26+FIB+lithography+kits|ELPHY+Quantum).

[17] W. R. Fahrner, *Nanotechnology and Nanoelectronics*, Springer-Verlag, Berlin (2005)

[18] NanoSYD Cleanroom, *Electron Beam Lithography (EBL) (Raith ELPHY Quantum module)*. //http// [www.nanosyd.dk/cleanroom/en/page/electron-beam-lithography](http://www.nanosyd.dk/cleanroom/en/page/electron-beam-lithography).

[19] NanoSYD Cleanroom, *Profilometer*. //http//  
[www.nanosyd.dk/cleanroom/en/sections/view/profilometer](http://www.nanosyd.dk/cleanroom/en/sections/view/profilometer).

[20] Bruker AXS, *Dektak 150 Stylus Profiler*. //http//  
[http://www.bruker-axs.com/dektak-150\\_stylus\\_profilometer.html](http://www.bruker-axs.com/dektak-150_stylus_profilometer.html).

[21] NanoSYD Cleanroom, *AFM-Atomic Force Microscope*. //http//  
[www.nanosyd.dk/cleanroom/en/sections/view/afm-atomic-force-microscope](http://www.nanosyd.dk/cleanroom/en/sections/view/afm-atomic-force-microscope).

[22] Veeco Instruments Inc., *Veeco Dimension 3100 Atomic Force Microscope User Manuals*, Santa Barbara (2005)

[23] University of Wisconsin System. Materials research science and engineering centre, The Board of Regents of the University of Wisconsin Systems, (2008). //http//  
[www.mrsec.wisc.edu/Edetc/nanoquest/afm/](http://www.mrsec.wisc.edu/Edetc/nanoquest/afm/).

- [24] Veeco Dimension 3100 Atomic Force Microscope (AFM), *Procedure (Last Update 11/20/06)*.  
//http// <http://164.67.193.121/machinefiles/pdf/AFM.pdf>.
- [25] A. Winkelmann, V. Sametoglu, A. Kubo, J. Zhao, H. Petek, *One-Photon and two-photon photoemission from Ag(111) surfaces*, Pittsburgh, PA 15260, USA
- [26] X. C. Wang, G. C. Lim, W. Liu, S. J. Chua, H. Y. Zheng, F. L. Ng, *Femtosecond Pulse Laser Ablation of Sapphire in Ambient Air*, *Applied Surface Science*, vol. 228, issue 1-4, pp. 221 -226, (2004).
- [27] C. Maibohm, *Generation and characterization of functionalized organic nanoaggregates*, Ph.D Thesis, University of Southern Denmark (2010)
- [28] Semrock, Inc., *Laser Damage Threshold*, Technical Notes, (2001-2011)
- [29] J. Fiutowski, C. Maibohm, J. Kjelstrup-Hansen, H.-G. Rubahn, *Laser ablation of polymer coatings allows for electromagnetic field enhancement mapping around nanostructures*, *Appl. Phys. Lett.* 98, 193117 (2011).
- [30] S. Baudach, J. Bonse, J. Krüger, W. Kautek, *Ultrashort pulse laser ablation of polycarbonate and polymethylmethacrylate*, *Appl. Surf. Science*, 154-155 (2000) 555-560.
- [31] User`s Manual, *Tsunami Mode-locked Ti:sapphire Laser*, Part Number 0000-232A, Rev. D, (2002).
- [32] Y. Dong, H. Sakata, P. Molian, *Femtosecond pulsed laser ablation of diamond-like carbon films on silicon*, *Appl. Surf. Science*, 252 (2005) 352-357.
- [33] R&D Mag web scientific publication journal, *Optical Microscope Specifications Guide: NikonMetrology, Inc.`s Universal Design Microscope*.
- [34] University of Johannesburg, *Ellipsometry*, Chapter 5

- [35] Angstrom Sun Technologies Inc., *Spectroscopic Ellipsometer SE200BM Film Thickness Measurement System*. //http//  
[www.angstec.com/Product/SE200BM.html](http://www.angstec.com/Product/SE200BM.html) .
- [36] EM Explorer, *Welcome to EM Explorer*, (2010) //http// [www.emexplorer.net/index.php](http://www.emexplorer.net/index.php).
- [37] D. W. Piston, T. J. Fellers, M. W. Davidson, *Fundamentals and Applications in Multiphoton Excitation Microscopy*, MicroscopyU webpage (2000-2010).
- [38] LG MMA, Inc., *Overviews on PMMA*, tech info (2005).
- [39] Microchem Corp., *Nano<sup>TM</sup> PMMA and Copolymer*, PMMA data sheet (2001).
- [40] H.-G. Rubahn, *Laser Applications in surface science and technology*, Wiley (1999).
- [41] A. Habenicht, M. Olapinski, F. Burmeister, P. Leiderer, J. Boneberg, *Jumping Nanodroplets*, Science 309, 2043 (2005).

Relative reflectance spectra of gold plasmonic substrates with nanocircle geometries

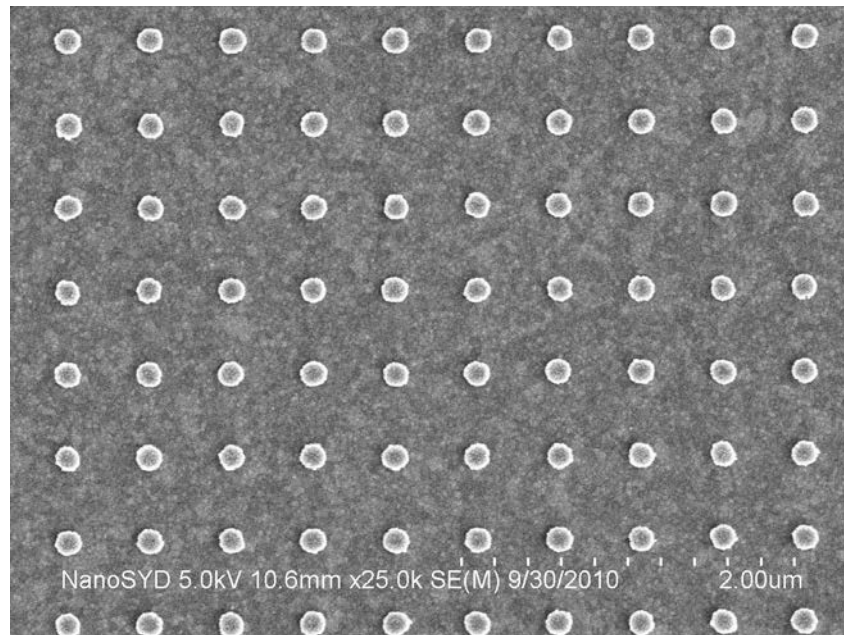


Image 1 SEM image of Au nanocircles array

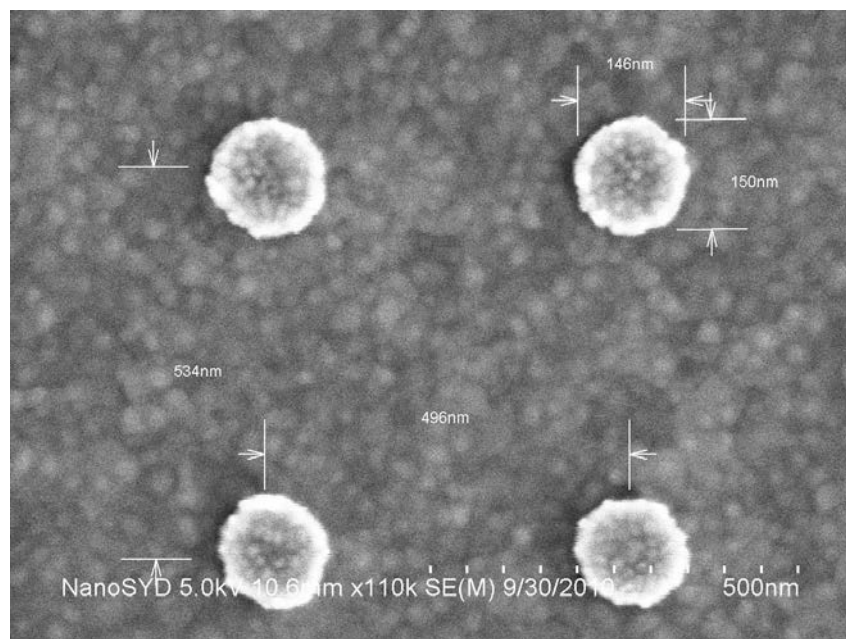


Image 2. Illustration of four Au nanocircles in array. The exposure area dose for this array is  $370 \mu\text{As}/\text{cm}^2$ . The distance between two Au nanocircles is approximately 500 nm, while the diameter of one nanocircle is about 150 nm.

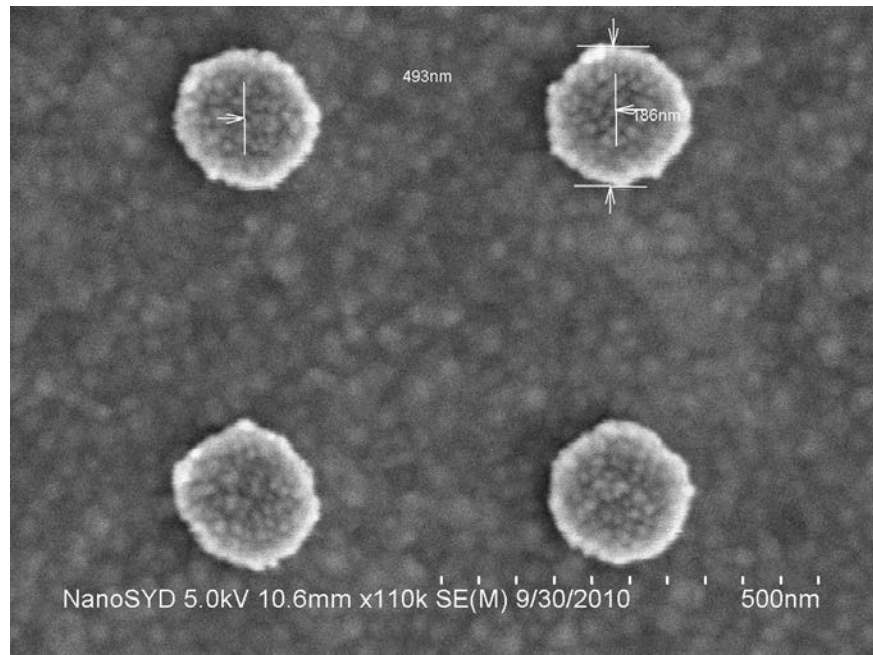


Image 3. Illustration of four Au nanocircles in array. The exposure area dose for this array is  $506 \mu\text{As}/\text{cm}^2$ . The distance between two Au nanocircles is approximately 500 nm, while the diameter of one Au particle is about 185 nm.

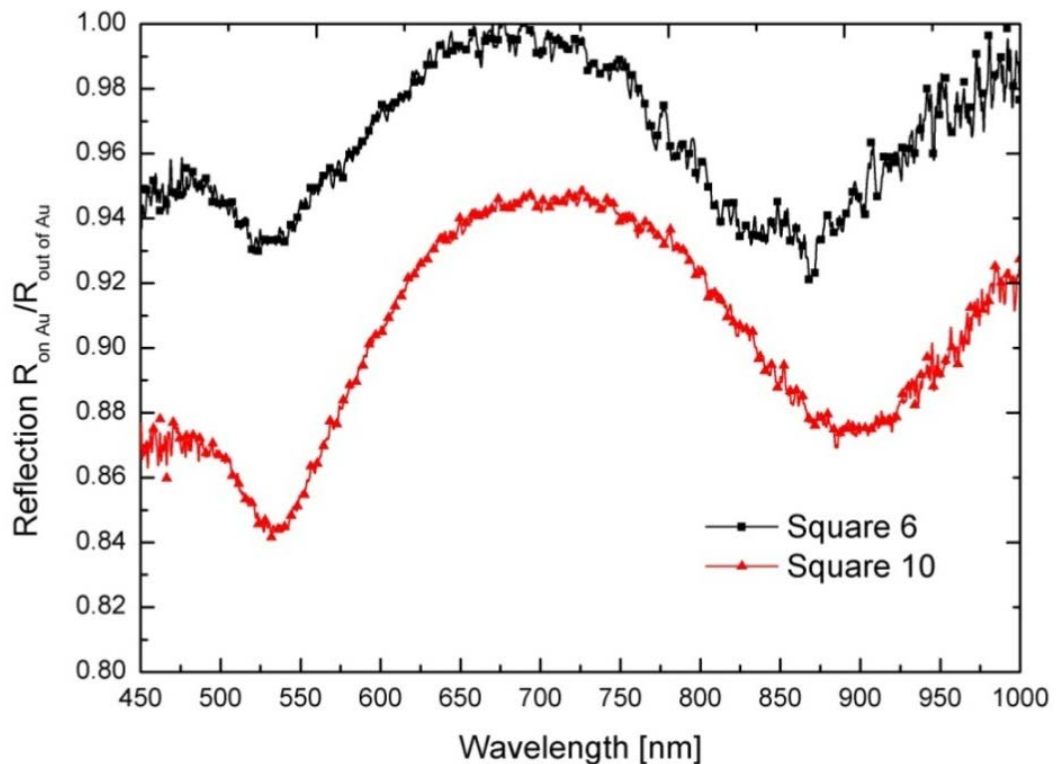


Image 4. Relative reflection spectra for nanocircles array of different diameters. Black – 150 nm; Red – 185 nm;

Light Transmission of PMMA and various materials

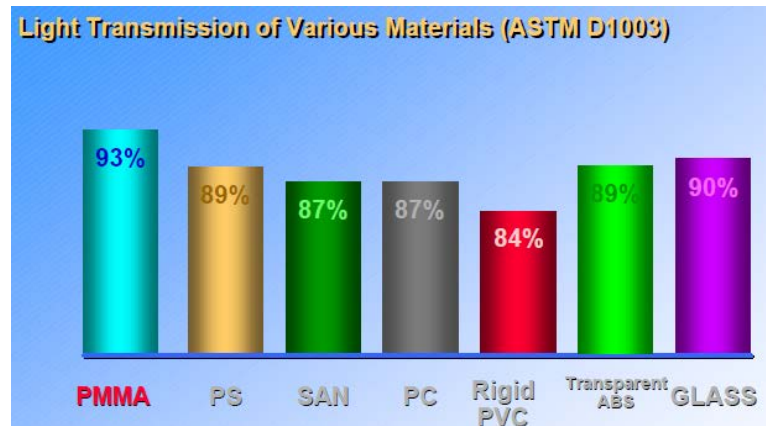


Image 5. Percentage transmittance of PMMA at 380-780 nm Visible Diapason [38]

Image 6 represents ellipsometry calculated reflectance spectra of gold at variable of incident angles and two different wavelengths of s- and p-polarized excitation light.

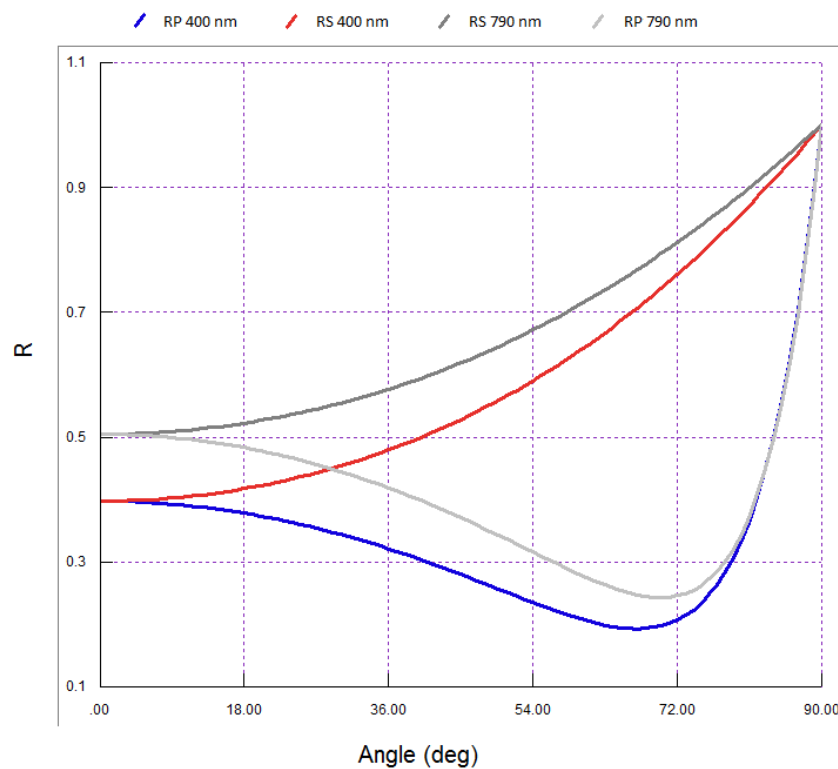


Image 6 Reflectance spectra of 70 nm Au thin film at different incident angles of light: blue and red curves represent reflection of P and S polarized 400 nm wavelength light respectively; light and dark grey curves represent reflection of P and S polarized 790 nm wavelength light respectively.

## EM Explorer Solution numerical algorithm for triangles

```
# Define wavelength
set wavelength 790.0
# Define simulation domain and grid properties
set lx 750.0
set ly 750.0
set lz 1500.0
set GRIDSIZE 20.0
set nx [expr int($lx/$GRIDSIZE+0.5)]
set ny [expr int($ly/$GRIDSIZE+0.5)]
set nz [expr int($lz/$GRIDSIZE+0.5)]
# Define triangle properties
set triangle_width 450.0
set triangle_height 450.0
set triangle_thickness 55.0
set triangle_n 0.15045
set triangle_k 4.82455
# Define properties of the film below the triangle
set film_thickness 70.0
set film_n 0.15045
set film_k 4.82455
# Define substrate properties
set substrate_thickness 500.0
set substrate_n 3.74951
set substrate_k 0.018917
# Define air n&k
set nair 1.0
set kair 0.0
# Loop over polarization
foreach pol {ypol xpol} {
set ID ${pol}
# Setup FDTD Grid
```

```

emxp::grid lx=$lx ly=$ly lz=$lz nx=$nx ny=$ny nz=$nz n0=$nair k0=$kair
# Substrate
set xc [expr $lx/2.0]
set yc [expr $ly/2.0]
set xw $lx
set yw $ly
set zc [expr 0.5*$substrate_thickness]
set zw [expr 1.0*$substrate_thickness]
emxp::solid shape=box xc=$xc yc=$yc zc=$zc xw=$xw yw=$yw zw=$zw n=$substrate_n
k=$substrate_k
# Film
set zc [expr $substrate_thickness+0.5*$film_thickness]
set zw $film_thickness
emxp::solid shape=box xc=$xc yc=$yc zc=$zc xw=$xw yw=$yw zw=$zw n=$film_n
k=$film_k
# Triangle
set zc [expr $substrate_thickness+$film_thickness+0.5*$triangle_thickness]
set zw $triangle_thickness
set xc1 $xc
set xc2 $xc
set yc1 [expr $yc-0.5*$triangle_height]
set yc2 [expr $yc1+$triangle_height]
set zc1 $zc
set zc2 $zc
set aw1 $zw
set bw1 $triangle_width
set aw2 $zw
set bw2 0.0
emxp::solid shape=frustum_y type=pyramid xc1=$xc1 yc1=$yc1 zc1=$zc1 aw1=$aw1
bw1=$bw1 xc2=$xc2 yc2=$yc2 zc2=$zc2 aw2=$aw2 bw2=$bw2 n=$triangle_n k=$triangle_k
# Setup FDTD incident field
if {$spol == "xpol"} {
set ep 1.0
set es 0.0

```

```

} else {
set ep 0.0
set es 1.0
}
emxp::planewave2 wavelength=$wavelength z_source=[expr $lz-2.0*$GRIDSIZE]
theta=180 phi=0 es_amp=$es ep_amp=$ep
# Setup FDTD PML
emxp::pml2
# Setup FDTD convergence monitor
emxp::convergence i=0 j=0 k=$nz sample_size=10 samples_per_cycle=1 tolerance=0.001
# Setup FDTD real-time snapshot (optional)
emxp::snapshot property=intensity file=snapshot_${pol} imin=[expr $nx/2] imax=[expr
$nx/2] jmin=0 jmax=$ny kmin=0 kmax=$nz
emxp::output property=geom file=triangle.vtk
# Run FDTD solver
emxp::run n_cycles=100
# Output intensity
emxp::output property=intensity imin=0 imax=$nx jmin=0 jmax=$ny kmin=0 kmax=$nz
file=intensity_${ID}.vtk
emxp::reset
}; #end of pol loop
exit

```

## Appendix 5

### Optical microscope with mercury lamp camera calibration

5x magnification	2698x2024 $\mu\text{m}$
10x magnification	1348x1011 $\mu\text{m}$
<b>20x magnification</b>	<b>674x506<math>\mu\text{m}</math></b>
50x magnification	270x202 $\mu\text{m}$
100x magnification	135x101 $\mu\text{m}$

*Publications*

1. O. Kostiučenko, A. Guobienė. Optical properties evaluation of silver nanocompound. *Mechatronic Systems and Materials : scientific papers / Kaunas University of Technology, Lithuanian Academy of Sciences, IFToMN National Committee of Lithuania, Vilnius Gediminas Technical University. Kaunas : Technologija. 2008 1822-8283, p. 75-79*
  
2. O. Kostiučenko (University of Southern Denmark), A. Guobienė (Kaunas University of Technology), S. Ponelytė (Kaunas University of Technology), I. Prosyčėvas (Kaunas University of Technology), J. Puišo (Kaunas University of Technology). Formation and investigation of photoplasmonic structures. [Radiation Interaction with Material and Its Use in Technologies 2010 : 3rd international conference, Kaunas, Lithuania, 20-23 September, 2010 : program and materials / Kaunas University of Technology, Vytautas Magnus University, Lithuanian Energy Institute, Riga Technical University. Kaunas : Technologija. ISSN 1822-508X. 2010.](#)

*Activities*

- “Mechatronics for Hi-Tech Devices“. **The Conference for Students and Young Researchers**, Kaunas University of Technology, Department of Mechanics and Mechatronics, Kęstučio g. 27, 44312 Kaunas, Lithuania, October, 30, 2008
  
- Series of lectures attended: PhD Antanas Daugėla, Seagate Technology LLC, Mineapolis, JAV. **Modern tools equipment and methods in nanometrology**: theory and application in investigation of nanostructures. Kaunas University of Technology, Department of Mechanics and Mechatronics, Kęstučio g. 27, 44312 Kaunas, Lithuania, February 15-29, 2008;
  
- Series of lectures attended: **arrangement and realization of national program for improvement of mechatronical researches competences**. Kaunas University of Technology, Department of Mechanics and Mechatronics, Kęstučio g. 27, 44312 Kaunas, Lithuania, 2007;
  
- Participant of Erasmus exchange programme for autumn semester 2009/2010. University of Southern Denmark

## *Certifications*

- BPD and EU certifications:
  - Engineering analysis;
  - Computer imitation systems of technological processes;
  - Computer imitation systems of manufacture processes preparations and mechanical treatment of manufacture;
  - Use of systems of integrated hardness analysis in mechanical engineering;
  - Systems of modelling and documentation preparations of mechanical systems and its elements;
  - Application of integrated dynamic-kinematic analysis systems in mechanical engineering
  - Modern computer project systems in mechanical engineering: from project to manufacture preparation and control;
  
- BPD and EU certification: “Imitation of business processes”
  
- Modern tools equipment and methods in Nano Metrology: theory and application in investigation of nanostructures.